A low cost, accurate instrument to measure the moisture content of building envelopes *in situ*

Thesis

A Low Cost, Accurate Instrument to Measure the Moisture Content of Building Envelopes *in situ*

Zhihui Ye

A thesis submitted for the degree of

Doctor of Philosophy at

The Open University

Milton Keynes

United Kingdom

November 2005

Abstract

Buildings must be designed and built to achieve a healthy environment, low energy consumption and a predictable service life. In order to achieve these goals the effects of combined heat, air and moisture (HAM) transfer must be understood. A suitable moisture measurement technique is thus required. There is a pressing need for a suitable instrument capable of *in situ* moisture measurements in building envelopes. Techniques do exist for such moisture measurement but all exhibit deficiencies in at least one critical area. A thermal dual-probe is investigated as a candidate for an appropriate instrument as such an approach offers significant potential benefits over existing methods.

It is demonstrated, via extensive finite-element (FE) modelling, that the thermal dual-probe technique is indeed applicable to *in situ* moisture measurements in typical building fabrics.

The thesis then moves on to deal with the *optimisation* of the design of such a probe. The results of relevant simulations using the proven two and three-dimensional FE models are detailed.

Finally, the extensive experimental work undertaken to support the modelling work is described. The measured data obtained from the thermal dual-probes is compared with the results of series of gravimetric analyses. Close agreement between the two methods is obtained.

The work, has successfully demonstrated that, depending upon the building fabric material, optimal probe lengths and spacing range from approximately 45-60mm and 12-20mm

respectively. The experimental work clearly indicates that the thermal dual-probe is capable of accurate, *in situ* moisture measurements in building envelopes.

Acknowledgements

I would particularly like to thank my supervisor Dr. Mike Davies for supporting me in this project, reading thesis drafts and providing help throughout the years.

I would like to thank my supervisor Professor Chris Earl for supervising my study at the Open University.

I would like to thank my external supervisors Professor Savvas A Tassou and Dr. Maria Kolokotroni for assisting my study at Brunel University.

Also I would like to thank Dr. Marko Tirovic for his most valuable supervision of the FE modelling work.

I am especially grateful to the Open University for providing me with scholarship support, as well as other financial support for the project.

Additional thanks go to the Brunel University Mechanical Engineering Department technician Mr. Clive Barrett for installing the dual-probe moisture sensor's electrical equipment. Thanks to Mr. Bryan Dear for helping me with mechanical work.

Thanks to Mr. Keith Withers for his invaluable help which made the laboratory work enjoyable.

Finally, I would also like to acknowledge the help provided to me by other Departmental staff and fellow students, especially Abas Fadel Hadawey, and others too numerous to mention by name.

Table of Contents

List of Tables

List of Figures

Page

Chapter 1

Introduction

Many building materials are porous bodies. In these porous bodies the moisture content may vary from a dry state to a fully saturated state, when the open pores are completely filled with water (Kumaran, 1996). Between the dry and saturated states, the moisture content varies with the water vapour pressure of the surroundings.

Heat transfer and moisture transfer are inextricably interconnected. Whenever a temperature difference exists, conditions conducive to moisture transfer also exist. Moisture enters building materials in several ways, such as:

- flooding
- driving rain
- run off from the roof and facade
- capillary rise of ground water
- occupants: washing, cooking, respiration etc.
- fire related water.

Let us consider why a knowledge of the moisture content of building fabrics is important. For example, in the UK, climate change is forecast to increase the likelihood of flooding. To reduce the impact of flooding on buildings, it is important to start the drying process as soon as possible after a building has been flooded. In order to allow the building to return to normal use, it is necessary to understand if it has been properly dried out as soon as possible.

A building material's durability, degradation and thermal performance can be affected by moisture transport (Goual *et al.*, 2000). Wet materials may also act as a substrate for the growth of bacteria, fungi and algae with possible physical and chemical damages, all potential risk factors to the inhabitants' health. A better understanding of moisture transfer can therefore reduce damage in building materials as well as preventing certain health risks.

Sanders (1996) notes that the combined heat, air and moisture (HAM) analysis of structures also relates to the development and testing of theoretical models. Many simulation models predict heat and moisture flows through building components and are used to design and assess buildings. However, there is inevitably uncertainty as to how much reliance can be placed on their predictions, due to the difficulty in determining the actual conditions within materials *in situ*.

For the reasons outlined above, there is therefore a need for monitoring. In order to provide monitoring, a suitable *in situ* measuring instrument must be available. There does not exist at present a technique for the measurement of moisture content within building fabrics which fulfils all of the following criteria. Ideally, such an instrument should be:

- capable of providing in situ measurements
- capable of producing transient measurements
- capable of producing moisture profiles through the fabric of a building envelope
- capable of providing measurements without the need for field calibration (or if calibration is required then it should be non-complex and reliable)
- insensitive to the movement of salts through the building fabrics
- accurate
- robust

- portable
- inexpensive
- non-complex.

Certainly, techniques do exist for moisture measurement (e.g. NMR (Pel *et al.*, 1992), gamma attenuation (Kumaran, 1993), thermogravimetric analysis (TGA), electrical resistance etc.) but all exhibit a failure in at least one of the above criteria.

Within the field of soil science, a technique has recently emerged which, for measurements in soils, appears to satisfy the above criteria. This is known as the 'dual-probe' technique (Tamara and Ham, 1997). Essentially, a short pulse of electrical energy (typically of the order of 10 seconds in duration) is applied to a wire within the 'heating' needle. The 'temperature sensor' needle, which incorporates a thermocouple (for example), records the resulting maximum temperature rise in the soil at a certain distance from the heating needle. A schematic dual-probe design is shown in Figure 1.1. This temperature rise, combined with knowledge of the volumetric heat capacity of the dry soil, allows the moisture content to be determined (see Chapter 3 for more details). Note that several thermocouples could be incorporated in the same sensor needle to allow a moisture profile to be recorded. The technique is essentially non-complex and the equipment required is standard and relatively inexpensive. It comprises the probes, a stable power supply and a data logging system.

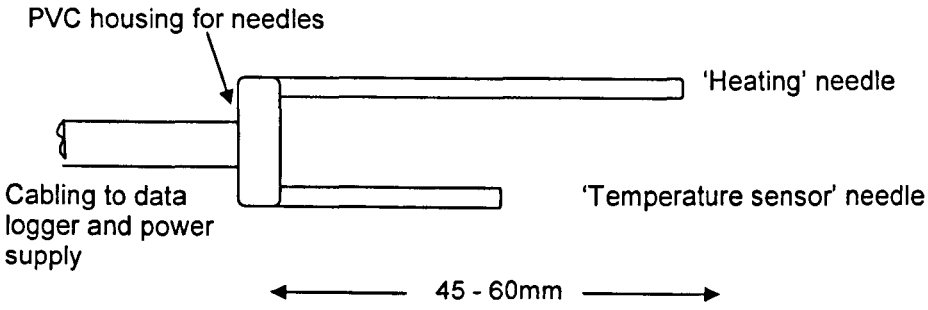

Figure 1.1 A conceptual dual-probe (not to scale)

Previous workers have investigated the use of a *single*-probe heat pulse instrument for conductivity measurements in building fabrics (Batty *et al.*, 1984 and Haupl *et al.*, 1992). It appears that, certainly for masonry materials, the technique can provide reliable conductivity measurements (Batty *et al.*, 1984). The possibility of using such conductivity measurements to deduce moisture content has been suggested (Haupl *et al.*, 1992). However, this would necessitate the conductivity/moisture relationship to be established for each material of interest. To some extent this data exists (Kumaran, 1996) but the relationship would be sensitive to any departure from the original test samples. Certainly, with regard to the *dual*-probe, the volumetric heat capacity is easier to measure with standard laboratory techniques. Additionally, with a single-probe, there does not exist the possibility of accessing accurate *changes* in the moisture content if absolute measurements are not possible due to unknown material properties. As the theory section in Chapter 3 will show, this *is* possible with the dual-probe, i.e., no field calibration is necessary if only measurements of changes in moisture content with time are required (indeed in many cases, the *changes* in moisture content may be more important than the absolute values).

The dual-probe would thus appear to be a suitable candidate for the measurement of moisture content within building fabrics. The aim of this study is to apply the theory of the dual-probe technique, and to construct a new dual-probe to be used in the context of the built environment. To achieve this aim, five separate tasks were completed:

1. The application of numerical finite element (FE) modelling to simulate the dual-probe related heat transfer in an aerated concrete wall. 2D and 3D FE models were set up to optimize the design of the dual-probe.
2. The determination of the robustness of the FE models.
3. The preparation of the aerated concrete samples for the dual-probe test.
4. The construction of the new dual-probes.
5. The testing of samples conditioned at different air Relative Humidity (RH) levels (89.0% and 96.4%).

A brief outline of the thesis follows:

In Chapter 2 the history of the dual-probe's development is described. The theory of the dual-probe was originally developed by Carslaw and Jaeger (1959). Campbell *et al.* (1991) proposed a dual-probe heat-pulse technique for determination of the volumetric heat capacity of soil. Further developmental work has been undertaken by Bristow *et al.* (1993, 1994). The dual-probe has since been applied to simultaneously determine volumetric heat capacity, thermal diffusivity, thermal conductivity and water content.

In Chapter 3 the dual-probe theory and sources of error related to the dual-probe are discussed. The methodology of the dual-probe is based on the application of a heat pulse to a line source, and analysis of the temperature response at the line source or at some distance from the line source (Carslaw and Jaeger, 1959). The measured temperature response was used to determine the volumetric heat capacity and hence the water content of the porous medium.

In Chapter 4 an extensive programme of numerical finite element (FE) modelling is described which was undertaken to simulate the dual-probe heat transfer process. A design

with a probe spacing of 6mm was developed successfully for which the FE model results were in good agreement with the analytical solution. A reliable FE modelling procedure was established and this could then be used for the optimisation of the probe design. The parameters used for constructing the 2D and 3D FE models that may affect the accuracy of the model simulation results are also discussed. This includes FE time step, transient simulation algorithms and surface convective heat transfer coefficients.

In Chapter 5 the use of FE models to optimise the design of the dual-probe is described. 2D models were used to determine the most suitable probe spacings and 3D models to determine the most suitable probe lengths.

In Chapter 6 the preparation of aerated concrete samples for the dual-probe test is described. The samples were cut to a suitable size, and holes were drilled to enable the dual-probe to be inserted. Four samples were conditioned with air of RH 96.4%. Five samples were conditioned with air of RH 89.0%. The curve of the sorption isotherm of the aerated concrete indicated that the equilibrium moisture content would be appropriate at these RH values (http://www.wufi.de).

In Chapter 7 the construction of the four dual-probes with probe spacing of 12mm and probe length of 50mm is described. A calibrated type T thermocouple was used to measure the temperature rise of the temperature sensor needle when an energy pulse was applied to the heating needle. The dual-probe heater was made by winding the resistance wire onto a core to 50mm long. A computer controlled data acquisition system was used to record the data automatically.

In Chapter 8 the tests of the samples at different moisture contents are discussed. The water-agar medium was first tested by the dual-probe. After checking the dual-probe in

this way, it was then tested with nine dry aerated concrete samples. The dual-probe was then tested with the nine conditioned 'wet' samples.

Chapter 9 summarises the work and provides conclusions and suggestions for further research.

Chapter 2

Literature Survey – Dual-probe

Alternative, existing methods of moisture content measurement have been noted in Chapter 1. This chapter now concentrates on the dual-probe method. The theory of the dual-probe technique (also referred to as the 'heat-pulse' technique) was originally developed by Carslaw and Jaeger (1959) who established the theory relating to the temperature change in an infinite medium, due to an instantaneously heated infinite line source, at a known distance from the source, due to a known quantity of heat.

Based on this work, a dual-probe heat-pulse method for measuring the volumetric heat capacity (ρc_p) of soil was proposed by Campbell *et al.* (1991). The dual-probe consisted of two parallel hypodermic needles, which were 0.813mm in diameter, 28mm long and spaced 6mm apart. One needle contained a heater with the resistance of 38Ω; the other contained a type T thermocouple at its centre. A measured current was applied to the heater for 8s to introduce a 700J/m heat pulse, so that the temperature rise could be detected by the thermocouple.

Campbell *et al.* (1991) calibrated the dual-probe spacing via a water-agar medium (2g/l). The effect of the agar on the thermal properties of the water was negligible, but was intended to prevent convection (Campbell *et al.*, 1991). The calibrated probe was successfully applied to measure the specific heat of six different types of soil samples. The coefficients of variation of specific heat for the six soil samples, as measured with the dual-probe, were within 2.1%.

Another application of the dual-probe was for measuring the moisture content of samples (changes in water content are primarily responsible for changes in specific heat – see Chapter 3 for full details of the relevant theory).

Bristow *et al.* (1993) applied the heat-pulse technique to determine the moisture content (θ) by using a relationship commonly attributed to De Vries (1963). It was shown that if only *changes* in moisture content ($\Delta\theta$) were being monitored, it was not necessary to know the ρc_p of the soil. A heat-pulse device was developed to determine the volumetric heat capacity and hence the water content of the porous medium. To remove changes in background temperature from the signal received at the temperature sensor probe, a third probe (a reference temperature probe) was introduced to the device. To check the probe spacing once the device had been installed, moisture content measurements were made both by the heat-pulse device and by gamma-ray attenuation. The corrected spacing of the probe was obtained by establishing a relationship between the predicted $\Delta\theta$ and the measured $\Delta\theta$. The predicted $\Delta\theta$ was obtained using the heat-pulse device measurement together with Equation (3.8), a correction for the probe spacing not yet being applied. The measured $\Delta\theta$ was obtained using gamma-ray attenuation. After applying the corrected probe spacing, the heat-pulse device provided an improved measurement of changes in soil moisture content (Bristow *et al.*, 1993).

Bristow *et al.* (1994) also developed the 'short-duration' heat-pulse theory, as applied to the dual-probe method, which simultaneously determines heat capacity and diffusivity. Thermal conductivity is simply the product of heat capacity and diffusivity. Bristow *et al.* (1994) showed that the instantaneous heat-pulse theory developed by Campbell *et al.* (1991) can be used to approximate short-duration heat pulses when determining volumetric heat capacity, but that instantaneous approximations are inadequate for determining thermal conductivity and diffusivity. Initial experiments were conducted on air-dry sand

and clay materials to measure soil thermal properties. The soil thermal properties measured by the dual-probe compared well with these measured by independent methods. This then suggested that the dual-probe heat-pulse method had potential for the routine measurements of soil thermal properties.

Further work undertaken by Bristow *et al.* (1995) established possible approaches used to analyse the temperature-time data obtained using the dual-probe heat-pulse sensor. The first approach was the 'single-point' method. This relied on accurate identification of the peak in the temperature-time measurements. The second approach, referred to as the 'Marquardt' method, involved a nonlinear temperature model to fit the data of temperature-time measurements. It appeared to be better to use the 'Marquardt' method for broad, flat peaks and sparse, 'noisy' data.

Bristow (1998) demonstrated the ability of the dual-probe heat-pulse sensor to provide reliable measurements of soil thermal properties and volumetric water content made on unsaturated sandy soil which was subject to a drying and wetting cycle. The measured thermal properties were then compared with independent measurements made with standard procedures based on the soil bulk density, specific heat and volume fraction of the soil constituents (De Vries, 1963; Campbell, 1985). The measurements indicated that the dual-probe had an important role to play in monitoring soil water content as well as providing soil thermal property data.

A total of twenty-four dual-probes were constructed by Tarara and Ham (1997) in 1994 and tested both in the laboratory and in the field. The dual-probe was designed to be similar to that of Campbell *et al.* (1991). However, to improve its rigidity, the dual-probe was made with larger diameter hypodermic tubing to maintain a fixed probe spacing when it was inserted into the soil in the field. The dual-probe spacing was calibrated using the

same method as was used by Campbell *et al.* (1991). The calibration results indicated that calibration to a known heat capacity eliminated the need for precise, accurate, physical measurements of the probe spacing, and it corrected the probe's estimate of ρc_p for non-ideal heat flow.

Tarara and Ham (1997) introduced a new method of testing dual-probes in the laboratory. In addition to the testing in a water-agar medium, the probes were tested in both dry glass beads and water-saturated glass beads, in order to represent the extremes of possible soil water content. Each medium was tested for 48 hours at 30 minutes intervals. Prior to the heat pulse being applied to the dual-probe heater, the initial temperature was recorded. The temperature rise was then measured by the thermocouple and recorded every 0.5 seconds for 60 seconds. The results of using the probes to estimate the ρc_p of dry glass beads and water-saturated glass beads were within 2.2 and 0.2% of their calculated values, respectively. These results were coupled with successful field tests, demonstrating the validity of choosing glass beads to represent soil. Further testing in two types of soil was compared to the gravimetric method. The two methods agreed to within $0.03 m^3 m^{-3}$ and $0.04 m^3 m^{-3}$, over a range of θ from $0.45 m^3 m^{-3}$ to $0.10 m^3 m^{-3}$; estimates of change in θ ($\Delta\theta$) between desorption steps agreed to within $0.01 m^3 m^{-3}$ respectively. In the field, the measurements of θ among three dual-probes installed at same depth, beneath bare soil, agreed to within $0.02 m^3 m^{-3}$ on average. The agreement between dual-probe and gamma attenuation measurements was within $0.05 m^3 m^{-3}$. In 1995, further field tests were conducted after installing sixteen dual-probes with improved design 10cm beneath a drip-irrigated row crop. A consistent difference of approximately $0.10 m^3 m^{-3}$ between much-covered and bare soil beds was detected.

Over the past ten years, dual-probe heat-pulse sensors have been developed that allow the simultaneous determination of volumetric heat capacity, thermal diffusivity, thermal conductivity and moisture content simultaneously (Campbell *et al.*, 1991; Bristow *et al.*, 1993 and 1994; Tarara and Ham, 1997). As above, estimation of thermal properties is accomplished by using a model for the conduction of heat away from an instantaneously heated infinite line source (ILS). Kluitenberg *et al.* (1993, 1995) examined the possible sources of error in the application of the infinite line source theory by comparing the ILS model (Campbell *et al.*, 1991; Bristow *et al.*, 1993 and 1994) with six other models. The application of the ILS model (Campbell *et al.*, 1991; Bristow *et al.*, 1993) was used to determine volumetric heat capacity, and hence water content. The application of the ILS model (Bristow *et al.*, 1994) was used to determine volumetric heat capacity, thermal conductivity, thermal diffusivity and moisture content simultaneously. Kluitenberg *et al.* (1993) examined the possible sources of error associated with the ILS model (Campbell *et al.*, 1991; Bristow *et al.*, 1993) by comparing it with three other models: finite probe length, cylindrical heater shape and short-duration heating. Kluitenberg *et al.* (1995) also examined the possible sources of error associated with the ILS model (Bristow *et al.*, 1994) by comparing it with three other models: finite probe length, cylindrical heater shape and finite cylindrical probe. The ILS model's assumption of an infinite line source heater produced errors in determining soil thermal properties, however, because in practice, the heater has finite length and a cylindrical shape (Campbell *et al.*, 1991; Bristow *et al.*, 1993 and 1994; Tarara and Ham, 1997). The errors of estimation of the volumetric heat capacity that resulted from ILS model (Campbell *et al.*, 1991; Bristow *et al.*, 1993) were within 1% (Kluitenberg *et al.*, 1993). Error analysis by Kluitenberg *et al.* (1995) indicated that for the typical probe design, the error was less than 2% of the estimated thermal properties by assuming an infinite length for a heat source of finite length. The error was less than 0.6% of the estimated thermal properties by assuming the cylindrically shaped heater to be a line heater source. Theoretical analyses (Kluitenberg *et al.*, 1993 and 1995) and experimental

results (Bristow *et al.*, 1994) indicate the importance of accurate probe spacing (r) and time-to-maximum-temperature-rise (t_{max}) measurements for the accuracy of thermal and water content estimations.

Applying the dual-probe heat-pulse sensor enables a soil's thermal properties and moisture content to be measured simultaneously. At present, though, as indicated above, the dual-probe heat-pulse sensor is used for moisture measurements in *soils*. Applying the heat-pulse technique, it was thought possible to develop such a dual-probe for *in situ* moisture content measurement in *buildings*. Beal (1999) and Linscott (2000) undertook projects in constructing the dual-probe heat-pulse sensor used for moisture content measurement in building materials. Experiments were conducted to find the possible probe geometry, heating time, method of drilling holes into the building envelope, materials for construction of the dual-probe and the dual-probe construction method. Several dual-probes with different geometric design were developed and tested using different materials. However, the differences between the experimental results and the theoretical solution were over 50% (Beal, 1999; Linscott, 2000). This was mainly due to inadequate probe design - the probes were not designed via numerical modelling. The objective of this project is to develop such a dual-probe for *accurately* measuring the moisture content of building fabrics. To achieve this, the probe length, probe spacing, heating time, energy input to the heater, the maximum temperature rise at the temperature sensor needle are optimised via numerical (FE) computer modelling. Additionally the technique of drilling two holes in parallel in the building envelope for installation of the dual-probe are developed along with the methods of construction of the dual-probe and conditioning the test samples.

Chapter 3

Dual-probe Theory and Sources of Error in the Experiments

3.1 Introduction

In this chapter the dual-probe theory and sources of error relating to the dual-probe experiments are described.

3.2 Dual-probe Theory

Equation (3.1) defined by Carslaw and Jaeger (1959) describes the temperature change in an infinite medium, in which a finite quantity of heat is released *instantaneously* by a line source of infinite length.

$$\Delta T = \frac{Q}{4\pi kt}\exp\left(\frac{-r^2}{4kt}\right) \qquad (3.1)$$

where Q = finite quantity of heat ($m^2{}^oC$)

ΔT = temperature rise (°C)

r = distance from the source (between the temperature sensor and the heater element) (m)

t = time after the instantaneous heat pulse (s)

k = thermal diffusivity of the medium (m^2/s)

Campbell *et al.* (1991) further developed the work of Carslaw and Jaeger (1959). A thermal probe was constructed using a heat-pulse method to determine specific heat and water content of the soil. Campbell *et al.* (1991) defined a relationship between the volumetric heat capacity and the maximum temperature rise at a known distance from the line heat source, and hence the water content of the porous medium.

To find the maximum temperature rise in Equation (3.1), the time when the maximum temperature rise occurred is first required. Differentiating Equation (3.1) with respect to time and equating its derivative to zero, the time of the maximum temperature rise can be found.

$$t_m = \frac{r^2}{4k} \tag{3.2}$$

where t_m = the time of maximum temperature rise at radius r (s)

Substituting Equation (3.2) into Equation (3.1), the maximum temperature rise ΔT_m(°C) can be obtained.

$$\Delta T_m = \frac{Q}{e\pi r^2} \tag{3.3}$$

Another parameter (the heat input to the line source, q (J/m)) was introduced by Carslaw and Jaeger (1959).

$$q = \rho c_p Q \tag{3.4}$$

where ρ = density of a medium (kg/m^3)

c_p = specific heat of a medium (J/kgK)

Substituting Equation (3.4) into Equation (3.3) yields:

$$\rho c_p = \frac{q}{e\pi r^2 \Delta T_m} \tag{3.5}$$

De Vries (1963) defined an equation to calculate the volumetric heat capacity.

$$\rho c_p = \rho_b c_{pb} + \rho_w c_{pw} \theta \tag{3.6}$$

where ρ_b = bulk density of a medium (kg/m^3)

c_{pb} = specific heat of a medium (J/kgK)

ρ_w = bulk density of water (kg/m^3)

c_{pw} = specific heat of water (J/kgK)

θ = water content (m^3/m^3)

Further development of the work of De Vries (1963) and Campbell *et al.* (1991) was carried out by Bristow *et al.* (1993). Combining Equations (3.5) and (3.6) yields an expression for water content.

$$\theta = \frac{\frac{q}{e\pi r^2 \Delta T_m} - \rho_b c_{pb}}{\rho_w c_{pw}} \tag{3.7}$$

From Equation (3.7), it can be seen that the accuracy of θ is dependent on an accurate measurement of the parameters r, q, ΔT_m and $\rho_b c_{pb}$. The accuracy of θ is extremely sensitive to the errors in r due to θ being a function of r^{-2}. An example which examines the sensitivity of θ to r is given in Appendix A.

In order to measure θ, it is necessary to know the material property of $\rho_b c_{pb}$. However, in practice, it is sometimes difficult to know the value of $\rho_b c_{pb}$ exactly. Bristow *et al.* (1993) produced a solution for monitoring *changes* in water content ($\Delta\theta$, Equation (3.8)). $\Delta\theta$ is still a function of r^{-2} and remains sensitive to the measurement accuracy of r, but the sensitivity is not the one in θ. An example is given in Appendix A which examines the measurement accuracy of the effect of r on the accuracy of $\Delta\theta$.

$$\Delta\theta = \theta_0 - \theta_i = \frac{1}{e\pi r^2 \rho_w c_{pw}} \left(\frac{q_0}{\Delta T_{m0}} - \frac{q_i}{\Delta T_{mi}} \right) \tag{3.8}$$

where θ_0 = initial reading of moisture content (m^3/m^3)

θ_i = ith reading of moisture content (m^3/m^3)

q_0 = initial quantity of heat per unit length (J/m)

q_i = ith quantity of heat supplied (J/m)

ΔT_{m0} = initial maximum temperature rise (°C)

ΔT_{mi} = ith maximum temperature rise (°C)

Substituting the ρc_p value of 'standard' water into the above equation, Equation (3.8) can be simplified as:

$$\Delta\theta = \frac{1}{4187e\pi r^2}\left(\frac{q_0}{\Delta T_{m0}} - \frac{q_i}{\Delta T_{mi}}\right) \tag{3.9}$$

Thus an accurate, absolute, determination of $\Delta\theta$ is possible. Calibration of the probe for specific materials is then no longer necessary.

In order to compare the dual-probe moisture content to gravimetric test results, the *changes* of moisture content of the dual-probe measurement in this study is calculated mass by mass ($\Delta\theta_m$, kg/kg). Changing the unit of $\Delta\theta$, Equation (3.8) becomes:

$$\Delta\theta_m = \frac{1}{e\pi r^2 \rho_0 c_{pw}}\left(\frac{q_0}{\Delta T_{m0}} - \frac{q_i}{\Delta T_{mi}}\right) \tag{3.10}$$

where ρ_0 = density of the dry medium (kg/m^3)

3.2.1 Theoretical Approximation

The theory of the heat-pulse method (Campbell *et al.*, 1991) is based on an idealised situation: an instantaneous heat pulse from an infinite line source, in an infinite, homogeneous, isotropic medium, with a uniform initial temperature (Bristow *et al.*, 1993). These ideal conditions are clearly an approximation of reality. In particular, the theory of an instantaneous line source of infinite length assumes that: the finite heater used approximates an infinite line source; the cylindrical heater approximates a line heat source; and the short duration of heating approximates an instantaneous release of heat (Kluitenberg *et al.*, 1993).

Kluitenberg *et al.* (1993) discussed in great detail the experimental errors associated with the heat-pulse method (Campbell *et al.*, 1991). As described in Chapter 2, based on the heat-pulse method, Campbell *et al.* (1991) proposed the ILS model to estimate the volumetric heat capacity, and hence the water content (Bristow *et al.*, 1993). To examine the errors associated with the ILS model (Campbell *et al.*, 1991), Kluitenberg *et al.* (1993) proposed three models: finite probe length, cylindrical heater shape, short duration non-instantaneous heating, based on the assumption made for an instantaneous line source of infinite length. Comparing the three models of Kluitenberg *et al.* (1993) with the ILS model (Campbell *et al.*, 1991), Kluitenberg *et al.* (1993) showed that the errors associated with these approximations were very small. In fact, the results indicated an error of approximately 1% in ρc_p in the measurement from the ILS model (Campbell *et al.*, 1991). Kluitenberg *et al.* (1993) concluded that the validity of the ILS model (Campbell *et al.*, 1991) holds, because the maximum temperature rise in the ILS model (Campbell *et al.*, 1991) was satisfactorily represented by the maximum temperature rise of these three models of Kluitenberg *et al.* (1993).

3.2.2 Summary

The dual-probe heat-capacity sensor has been previously developed to provide small scale *in situ* measurements of soil thermal properties. The error analysis (for this application) of the dual-probe theory concluded that for a typical dual-probe design a 1% error existed for estimating ρc_p due to the assumption made in the model's theory, while moisture content measurement is the product of the measurement of ρc_p. The aim of this study is to develop such a dual-probe for *in situ* moisture content measurement in building fabrics.

3.3 Sources of Error in the Dual-probe Experiments

In order to be able to apply the dual-probe to building fabrics, any sources of error must not result in significant departures such that Equation (3.5) does not hold. Potential sources of error must therefore be examined carefully.

Significant issues regarding sources of error are as follows (Davies *et al.*, 2004):

1. moisture movement within the sample as a result of the heat input
2. probe spacing
3. probe dimensions
4. heating times
5. probe material
6. contact resistance between probe and material
7. errors in the measurement of q
8. errors in the measurement of ΔT_m
9. errors due to inappropriate assumptions of material homogeneity.

Modelling and experimental work can provide an insight into these sources of error. Issues 1-5 will be investigated in Chapters 4 and 5. Issues 6-9 will be discussed in Chapter 8.

From a nunerical FE modelling point of view, significant sources of error will arise from the probe spacing, probe dimensions and materials of the probe and the test medium. Inappropriate design of the probe spacing and lengths may result in the predicted FE maximum temperature rise being very different from the theoretical solution. The probe spacing and probe dimensions are designed for the specific materials of the probe and test medium. Any significant changes in the material properties of the probe and test media

may result in a different design of the probe spacing and dimensions. Different building materials have different properties. Thus, the dual-probe designed with different probe spacing and length may be needed for measuring the moisture content of different building material. This work concentrated on the probe design, probe construction and experimentally measuring the moisture content of aerated concrete type B (CELCON, 2003) (Chapters 4 to 8).

From an experimental point of view, the main sources of error come from the measurement errors of ΔT_m, q, r and ρc_p (if the unit of kg/kg is used for $\Delta\theta$ measurement) of the test medium.

Before constructing the dual-probe physically, FE modelling work was undertaken to design the probe spacing, probe dimensions and energy input. The details of this design work are given in Chapters 4 and 5.

Chapter 4

Numerical Modelling

4.1 Introduction

In this chapter, an extensive program of numerical modelling is described which was undertaken to simulate the dual-probe heat transfer process. The aim of the modelling was to design the dual-probe, investigating such issues as the energy input and the physical dimensions of the dual-probe. Firstly, a summary of the governing equations is given. Secondly, the use of a one-dimensional heat and moisture transfer model to investigate the impact of the instrument on any moisture movement within a sample is described - this work was intended to give an indication of the amount of energy that could be put into the system without significantly disturbing the moisture field. Thirdly, the parameters used to construct the models are investigated to ensure that a 'robust' model will be obtained. Finally, the development and testing of two and three-dimensional (purely conductive) FE models is discussed in detail. A paper relating to the work described in Chapter 4 has been published (Davies *et al.*, 2004), which was awarded the Carter Bronze Medal (CIBSE, 2006).

4.2 Numerical Analysis of Heat and Moisture Transfer

4.2.1 Heat Transfer

4.2.1.1 Heat Transfer Equations

Heat Conduction Rate Equations

Conductive heat transfer is described by Fourier's law and is given by (Krishnamoorthy, 1996):

$$Q_h = -\lambda A_h \frac{\partial T}{\partial x} \tag{4.1}$$

where Q_h = heat flow rate (W)

λ = thermal conductivity of the material (W/mK)

A_h = area normal to the direction of heat flow (m^2)

x = length in the direction of heat flow (m)

When heat flux (heat flow rate per unit area) q_h (W/m^2) is used to express the heat flow rate (Krishnamoorthy, 1996):

$$q_h = -\lambda \frac{\partial T}{\partial x} \tag{4.2}$$

Energy Balance Equation

The energy conservation equation is one of the key equations for heat transfer analysis. A general form of the energy conservation is expressed as (Krishnamoorthy, 1996):

$$E_{in} + E_g = E_{out} + E_{\text{int}} \tag{4.3}$$

where E_{in} = energy flow into the system (W)

E_g = energy generated into the system (W)

E_{out} = energy flow out the system (W)

E_{int} = change in internal energy of the system (W)

Governing Differential Equation

The governing differential equation is derived by using the heat flow equation and the energy conservation equation with regards to an elemental volume of a solid body as shown in Figure 4.1.

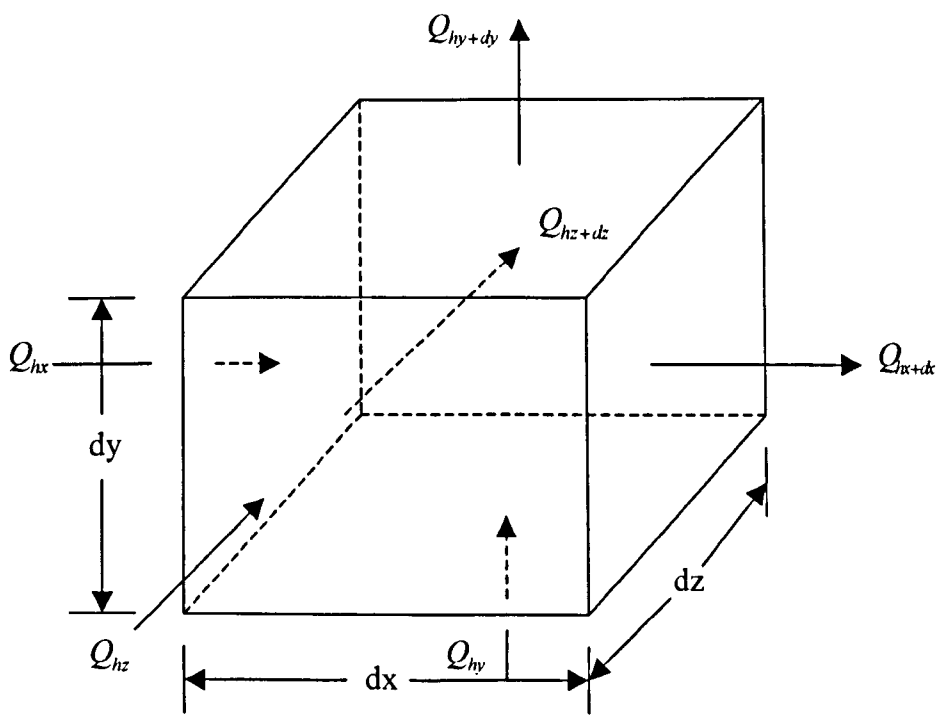

Figure 4.1 Elemental volume

For a three-dimensional stationary system in Cartesian coordinates, the energy balance for the elemental volume is (Krishnamoorthy, 1996):

$$\left(Q_{hx} + Q_{hy} + Q_{hz}\right) dt + G\ dxdydz\ dt = \left(Q_{hx+dx} + Q_{hy+dy} + Q_{hz+dz}\right) dt + \rho c\ dxdydz\ dT \tag{4.4}$$

where G = rate of heat generated per unit volume (W/m^3)

dT = temperature changes during dt (°C)

$$Q_{hx} = -\lambda_x\ A_x\ \frac{\partial T}{\partial x} = -\lambda_x\ dydz\ \frac{\partial T}{\partial x}$$

where Q_{hx} = heat flow into the face $dydz$ located at x (W)

Similarly, at location $x + dx$ (Krishnamoorthy, 1996),

$$\begin{aligned} Q_{hx+dx} &= \text{heat flow from the face } dydz \text{ located at } x + dx \\ &= Q_{hx} + \frac{\partial Q_{hx}}{\partial x} dx \\ &= -\lambda_x\ dydz\ \frac{\partial T}{\partial x} - \frac{\partial}{\partial x}\left(\lambda_x\ A_x\ \frac{\partial T}{\partial x}\right) dx \\ &= -\lambda_x\ dydz\ \frac{\partial T}{\partial x} - \frac{\partial}{\partial x}\left(\lambda_x\ \frac{\partial T}{\partial x}\right) dxdydz \end{aligned} \tag{4.5}$$

where λ_x = thermal conductivity of the material in the x direction (W/mK)

Similarly at location $y + dy$ and $z + dz$,

$$Q_{hy+dy} = -\lambda_y\ dxdz\ \frac{\partial T}{\partial y} - \frac{\partial}{\partial y}\left(\lambda_y\ \frac{\partial T}{\partial y}\right) dxdydz \tag{4.6}$$

$$Q_{hz+dz} = -\lambda_z\ dxdy\ \frac{\partial T}{\partial z} - \frac{\partial}{\partial z}\left(\lambda_z\ \frac{\partial T}{\partial z}\right) dxdydz \tag{4.7}$$

where λ_y = thermal conductivity of the material in the y direction (W/mK)

λ_z = thermal conductivity of the material in the z direction (W/mK)

Dividing *dx dy dz dt* from Equation (4.4) yields:

$$\frac{Q_{hx}+Q_{hy}+Q_{hz}}{dxdydz}+G=\frac{Q_{hx+dx}+Q_{hy+dy}+Q_{hz+dz}}{dxdydz}+\rho c\frac{dT}{dt} \qquad (4.8)$$

Substituting the expression of heat flow in the x, y and z directions (Equations 4.5 to 4.7) into Equation (4.8) yields the differential equation governing heat conduction in a solid body in which λ_x, λ_y, and λ_z are different (Krishnamoorthy, 1996).

$$\frac{\partial}{\partial x}\left(\lambda_x\frac{\partial T}{\partial x}\right)+\frac{\partial}{\partial y}\left(\lambda_y\frac{\partial T}{\partial y}\right)+\frac{\partial}{\partial z}\left(\lambda_z\frac{\partial T}{\partial z}\right)+G=\rho c\frac{\partial T}{\partial t} \qquad (4.9)$$

If in an isotropic material, the thermal conductivity in the x, y and z directions are the same ($\lambda_x = \lambda_y = \lambda_z$ = constant), and no heat generated then Equation (4.9) reduces to (Krishnamoorthy, 1996),

$$\frac{\partial^2 T}{\partial x^2}+\frac{\partial^2 T}{\partial y^2}+\frac{\partial^2 T}{\partial z^2}=\frac{1}{k}\frac{\partial T}{\partial t} \qquad (4.10)$$

and k is given as:

$$k=\frac{\rho c}{\lambda} \qquad (4.11)$$

For the application of dual-probe heat transfer, the cylindrical coordinate system (r_c, α, z) is used instead of the Cartesian coordinates, Equation (4.10) becomes (Krishnamoorthy, 1996):

$$\frac{1}{r_c}\frac{\partial}{\partial r_c}\left(r_c\frac{\partial T}{\partial r_c}\right)+\frac{1}{r_c^{\,2}}\frac{\partial^2 T}{\partial \alpha^2}+\frac{\partial^2 T}{\partial z^2}=\frac{1}{k}\frac{\partial T}{\partial t} \qquad (4.12)$$

The above equations are first order in time and second order in spatial coordinates. Therefore one initial condition and two boundary conditions for each spatial coordinate are required. There are two kinds of boundary conditions: boundary temperature distribution, boundary heat flux due to conduction, convection and radiation.

In order to deal with the governing equations, a large number of commercial FE packages are available. The CAE package 'I-DEAS' (supplied by UGS (http://www.ugsplm.co.uk)) is adopted in this work.

4.2.2 Heat and Moisture (HAM) Transfer Model

The relevant model used in this study (by others) was developed by Galbreith *et al.* (2001a) from which the following description of the governing equations is drawn.

Conservation Equations

The equations governing coupled heat and moisture transfer within building materials were analysed in detail by Galbreith (1992). The mass and energy conservation equations are as follows:

Mass conservation

$$\frac{\partial(\rho u)}{\partial t} = -\nabla \cdot j \tag{4.13}$$

where ρ_0 = density of the material (kg/m^3)

u = moisture content (kg/kg)

The moisture transport flux j can be expressed as:

$$\begin{aligned} j = j_v + j_l &= -\left(D_v + \frac{D_l R_v T \rho_l}{p_v} \right) \nabla p_v - \left[D_l R_v \rho_l \left(\ln \phi - \frac{L}{R_v T} \right) \right] \nabla T \\ &= -\mu \nabla p_v - \left[D_l R_v \rho_l \left(\ln \phi - \frac{L}{R_v T} \right) \right] \nabla T \end{aligned} \tag{4.14}$$

where j_v = moisture transport flux for vapour (kg/m^{2}s)

j_l = moisture transport flux for liquid (kg/m^{2}s)

D_v = diffusion coefficients for vapour (s)

D_l = diffusion coefficients for liquid (s)

ρ_l = density of liquid water (kg/m^3)

p_v = water vapour pressure (N/m^2)

L = latent heat of water vaporisation (J/kg)

R_v = gas constant for vapour (J/kgK)

ϕ = relative humidity (-)

The differential permeability μ (s) of a material may be expressed using following relationship to separate the vapour and liquid phases:

$$\mu = D_v + \frac{D_l R_v T \rho_l}{p_v} = A + B\phi^C \tag{4.15}$$

The values of A, B and C are constants determined experimentally using non-linear regression (Galbraith *et al.*, 1993). Combining Equations (4.14) and (4.15), the moisture transfer flux can be rewritten as:

$$\begin{aligned} j &= -\left(A + B\phi^C\right)\nabla p_v - \left[D_l R_v \rho_l \left(\ln\phi - \frac{L}{R_v T}\right)\right]\nabla T \\ &= -[A\nabla p_v] - \left[B\phi^C \nabla p_v + \left\{\frac{B\phi^C p_v}{T}(\ln\phi - \frac{L}{R_v T})\right\}\nabla T\right] \end{aligned} \tag{4.16}$$

The first term on the right hand side of this equation describes the vapour transfer, in which vapour pressure gradient is the driving force, while the second term accounts for the liquid transfer and incorporates the influence of both the vapour pressure gradient and temperature gradient, i.e.

$$j_v = -[A\nabla p_v] \tag{4.17}$$

$$j_l = -\left[B\phi^C \nabla p_v + \left\{\frac{B\phi^C \nabla p_v}{T}\left(\ln\phi - \frac{L}{R_v T}\right)\right\}\nabla T\right] \tag{4.18}$$

Energy conservation

$$c\rho\frac{\partial T}{\partial t} = -\nabla \cdot q_k + j_i c_i \nabla T - L\nabla \cdot j_v \tag{4.19}$$

where j_i = moisture transfer flux for liquid and vapour (kg/m^{2}s)

c_i = specific heat capacity for vapour and liquid (J/kgK)

In the present model, air infiltration has been neglected, as in the models of (Chapman, 1987; McLean *et al.*, 1990). The relevant parameters were simplified and formulated as:

$$c = c_i u_i = c_0 u_0 + c_v u_v + c_l u_l + c_a u_a \approx c_0 u_0 + c_l u_l \qquad (4.20)$$

$$(u_0 = \text{unity},\ u_a \approx 0,\ u_l \gg u_v)$$

where c_0 = specific heat capacity of the dry material (J/kgK)

c_i = specific heat capacity of the material which contain moisture in liquid, vapour and air (J/kgK)

c_v = specific heat capacity for vapour (J/kgK)

c_a = specific heat capacity for air (J/kgK)

u_v = moisture content in vapour phase (kg/kg)

u_l = moisture content in liquid phase (kg/kg)

u_i = moisture content (liquid, vapour and air) of the material (kg/kg)

u_a = moisture content for air (kg/kg)

$$j_i c_i = j_0 c_0 + j_v c_v + j_l c_l + j_a c_a \approx j_v c_v + j_l c_l \qquad (j_0 = 0, j_a \approx 0) \qquad (4.21)$$

where j_i = moisture transport flux for vapour and liquid and air (kg/m^{2}s)

j_0 = moisture transport flux for the material (kg/m^{2}s)

j_a = moisture transport flux for air (kg/m^{2}s)

4.3 Preparatory HAM Modelling

In order to address the first of the issues regarding the sources of error that were noted in Chapter 3, collaboration was undertaken with Glasgow Caledonian University. Dr. Paul Baker undertook heat and moisture modelling to investigate the moisture migration within

a sample when an energy pulse is applied. Such migration is undesirable and, if significant, will place an upper limit on the energy input at the heating needle.

A one-dimensional transient heat and moisture transfer model was used for this purpose. The model, the basic theory of which has been introduced in Section 4.2, was developed at Glasgow Caledonian University and incorporates the following features:

- Humidity (ϕ) dependent vapour permeability (μ) is dealt with using the relationship in Equation (4.15) (Galbraith *el al.*, 1998).

- The thermal conductivity varies with moisture content and temperature. Similarly, the changes in thermal capacity and density with moisture content are also considered.

- Moisture capacity is treated using the relationship for the sorption isotherms derived by Hansen (1989).

- Liquid moisture transport is dealt with following Pederson (1990). Explicit liquid transport can be switched off in the model, although in the hygroscopic region liquid transport is dealt with implicitly by the permeability relationship.

- Dynamic boundary conditions may be applied to either side of the construction.

The model uses a control volume technique, with a two-way expansion space-discretisation scheme to optimise computation time without compromising accuracy (Galbraith *et al.*, 2001a and b).

The model performs well in comparison with (a) analytic steady-state moisture transfer calculations in the hygroscopic range and (b) a benchmark heat and moisture transfer computer program MATCH (Galbraith *et al.*, 2001a). The model has also been validated against experimental data obtained from gravimetric measurements of moisture flux through a number of materials with controlled boundary conditions.

The layer of material was divided into a grid with nodes at 0.2mm intervals. The simulated temperatures and relative humidities at the "sensor" location were recorded.

In general, the RH does not change significantly for the materials tested under typical conditions and pulse energy inputs. For brick, for example (see Figure 4.2), the maximum change is from 60% to 60.3% at a spacing of 6mm from the heating needle.

As Figure 4.2 indicates, any moisture migration within the building fabric, under typical conditions, was found to be insignificant for the materials investigated in this study.

So, in conclusion, it is clear that for the purposes of this study, the use of a purely conductive numerical model will suffice.

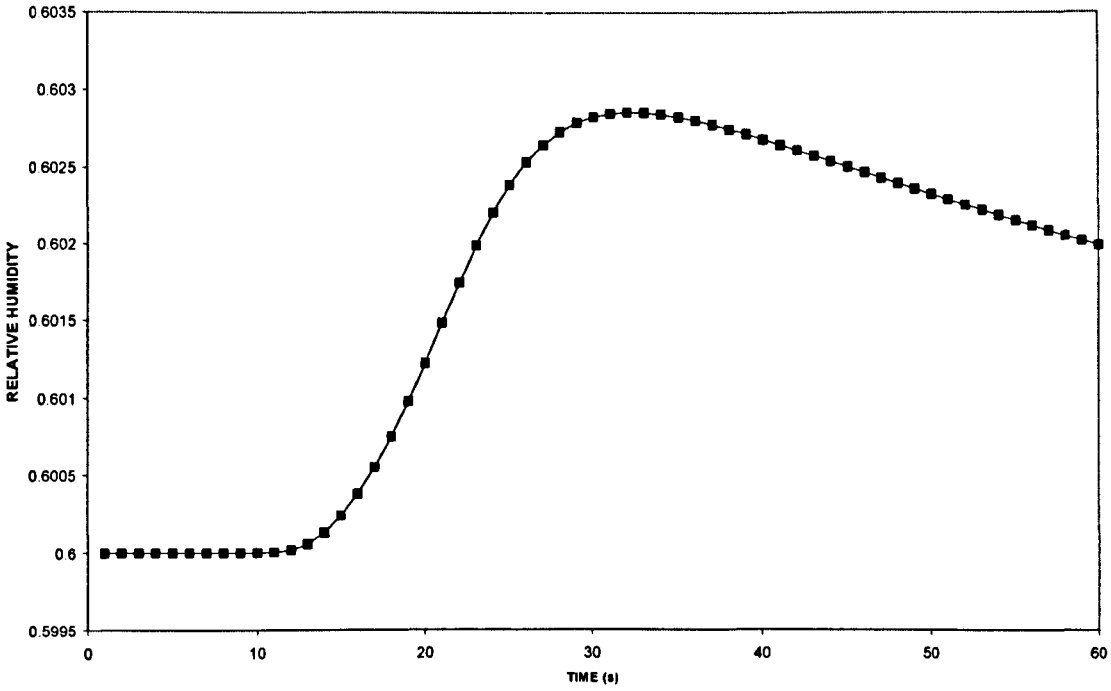

Figure 4.2 Predicted changes in relative humidity in brick at the sensor location as a result of the relevant energy input

4.4 Numerical Modelling (Purely Conductive) - Introduction

An extensive programme of numerical (Finite Element - FE) modelling has been undertaken. It is of course possible to undertake an analytical analysis of the problem, as Chapter 3 notes. However, numerical modelling enables a more general study, including the accurate modelling of actual heat impulse duration, the heating and temperature sensor needles, wall thickness, real wall boundary conditions etc.. As noted previously, the work described in section 4.3 showed that under the conditions that would hold in the experimental work, it would be reasonable to use a purely conductive model.

The overall aim of the numerical modelling was to show that the predicted temperature rises are in agreement with the analytical solution and hence that the relevant theory can be used with confidence to deduce the moisture content from the temperature rises that the probe will measure. In order to be able to use the FE model for this purpose it was necessary to 'validate' it. This was done by comparing a two-dimensional (2D) FE model (with no probe metal present) to the analytical solution. The analytical solution will hold for this situation and thus, if agreement is achieved, the model can be assumed to be 'validated'.

Numerous FE models and analysis approaches were examined in order to achieve high accuracy, acceptable model complexity and reasonable CPU times. 2D and 3D FE models, with and without steel needles were created, analysed and the results, as well as modelling and CPU times, compared. This was in order to gain confidence that it would be possible to produce a probe design in which the effect of the stainless steel is insignificant. It is clear that if the probes are too close together then one is not sampling the building fabric but merely the probe material (i.e., stainless steel). In the other extreme, probes at too great a spacing will result in low temperature increase (unless excessive heat is applied) compromising accuracy.

4.5 Development and Testing of the FE Model

To provide evidence that the model used to simulate the dual-probe heat transfer process in the building fabric was 'robust', the testing of the parameters used for constructing the 2D and 3D FE models will be discussed.

The effects of the time step, transient simulation algorithm and surface convective heat transfer coefficient on the maximum temperature rise were tested.

4.5.1 Fourier Number

The 'Fourier number' was used as guidance to determine the element length and the time step. The Fourier number can be calculated as:

$$\tau = \frac{k\Delta t}{\Delta x^2} \tag{4.22}$$

where Δt = time step (s)

Δx = element length (m)

Numerous models were created and analyses performed which enabled optimisation of FE mesh densities and time increments to ensure that very accurate results were obtained with acceptable effort (user input times and CPU times).

To exemplify such work, some typical results are presented here. To examine the time step effect on the simulation results, two 2D models (Models A and B) with a probe spacing of 6mm were tested with different time steps from 0.01s to 0.10s. Cast concrete and stainless steel were tested in these two models. The thermal properties of these materials (Incropera *et al.*, 1985; CIBSE GUIDE, 1986) are listed in Table 4.1. The needle was simulated with inner and outer diameters of 0.5mm and 1.5mm respectively. The detailed specifications of these two 2D models were:

Table 4.1 Material properties for a probe spacing of 6mm model

Material	Density (kg/m^3)	Thermal conductivity (W/mK)	Specific heat capacity (J/kgK)
Cast concrete (dense)	2100	1.40	840
Brickwork (out leaf)	1700	0.84	800
Aerated concrete type A	500	0.16	840
Stainless steel AISI 304	7900	14.90	477

2D Model A

- The element length of the stainless steel was 0.25mm.
- The element length of the cast concrete was 0.5mm.
- The model was extruded to 2mm in the z-direction.
- The total energy input was kept at 700J/m.

2D Model B

- The element length of the stainless steel was 0.25mm.
- The element length of the cast concrete was 0.125mm.
- The model was extruded to 0.25mm in the z-direction.
- The total energy input was kept at 700J/m.

In this section and Sections 4.5.2 to 4.5.3, the 3D models (Section 4.6.2) with a spacing of 6mm to simulate the dual-probe heat transfer in cast concrete were also used to examine the effects of time step, transient simulation algorithms and surface convective heat transfer coefficients on the FE model results. Time steps of 0.10s, 0.01s and 0.0015s were tested in the 3D model A. Time steps of 0.10s and 0.01s were tested in the 3D Model B. Cast concrete was tested in 3D Model A (without metal tubing). Cast concrete and stainless steel were tested in 3D Model B (with metal tubing). The detailed specifications of these two 3D models were:

3D Model A

- The element length of the cast concrete was 0.25mm.
- The model was extruded to 20mm in the z-direction.
- The model was extruded to 20mm in the -z-direction.
- The total energy input was kept at 700J/m.

3D Model B

- The element lengths of the cast concrete and stainless steel were 0.25mm.
- The needle was simulated with inner and outer diameters of 0.5mm and 1.5mm respectively.
- The lengths of heating and temperature sensor needles were simulated as 20mm and 10mm respectively. This was done by extruding the model to 20mm in the z-direction.
- The model was extruded to 20mm in the -z-direction for the distance of boundary at the back of the heating and temperature sensor needles.
- The total energy input was kept at 700J/m.

The simulation results of the time step effect on the maximum temperature rise are shown in Table 4.2. It can be seen that the time step did have an impact on the maximum temperature rise. The maximum temperature rise predicted by 3D Model A did not change with time steps of 0.01s and 0.0015s. Thus, 0.01s was chosen as a suitable time step to be applied to both 2D and 3D models which developed in Chapter 5. At the start stage for the modelling work, the 2D models developed in Section 4.6.1 and 3D models (Section 4.6.2) were tested with time step of 0.0015s.

Table 4.2 The effect of the time step on the maximum temperature rise

Material	Energy input (J/m)	Parameters		Numerical results		Analytical results
		Model	Time step (s)	t_m (s)	ΔT_m (K)	ΔT_m (K)
Cast concrete (dense) and stainless steel	700	2D A	0.10	21	1.03	1.29
			0.08	19 to 22	1.03	
			0.06	19 to 22	1.03	
			0.04	20 to 22	1.03	
			0.03	20	1.04	
			0.02	20	1.04	
			0.01	20 to 21	1.04	
Cast concrete (dense) and stainless steel	700	2D B	0.10	21	1.09	
			0.08	19 to 21	1.09	
			0.04	19 to 21	1.09	
			0.03	19 to 20	1.10	
			0.02	20	1.10	
			0.01	19 to 20	1.10	
Cast concrete (dense)	700	3D A	0.10	16 to 18	1.21	
			0.01	17 to 18	1.23	
			0.0015	17 to 18	1.23	
Cast concrete (dense) and stainless steel	700	3D B	0.10	18 to 21	0.92	
			0.01	18 to 21	0.93	

Note:
1. t_m is the time when the maximum temperature rise occurred at the temperature sensor needle.
2. The pulse time applied to all the models was 10s.

4.5.2 Transient Simulation Algorithm

The transient simulation algorithms available in the 'I-DEAS' package allow 'backward', 'backward-forward', 'forward' and 'exponential forward' methods to be used to run the model. Different transient simulation algorithms were thus used to test the 3D Models A and B (see detail of model in Section 4.6.2).

The simulation results obtained with the backward and backward-forward algorithms were the same and are shown in Table 4.3. The simulation results obtained with the exponential-forward algorithm were much lower than the analytical solution and are shown in Table 4.3. The results conducted by the forward algorithm were not obtained because the resulting solution time was impractically large. A decision was then taken to apply the

backward calculation algorithm to all the 2D and 3D models because the backward algorithm was unconditionally stable, computationally reliable and efficient, and more accurate than the backward-forward algorithm under conditions of rapid temperature change.

Table 4.3 The effect of the transient simulation algorithm on the maximum temperature rise

Material	Energy input (J/m)	Parameters			Numerical results		Analytical results
		Model	Transient solution algorithm	Time step (s)	t_m (s)	ΔT_m (K)	ΔT_m (K)
Cast concrete (dense)	700	3D A	backward	0.01	17 to 18	1.23	1.29
			backward-forward		17 to 18	1.23	
			exponential-forward		30	0.64	
Cast concrete (dense) and stainless steel	700	3D B	backward		18 to 21	0.93	
			backward-forward		18 to 21	0.93	

Note:
1. t_m is the time when the maximum temperature rise occurred at the temperature sensor needle.
2. The pulse time applied to all the models was 10s.

4.5.3 Surface Convective Heat Transfer Coefficients

In order to evaluate the impact of the convective heat transfer occurring between the surface of the building fabric and the surrounding air, the 3D Model A constructed in Section 4.6.2 was tested with different convective heat transfer coefficients. 4W/m^{2}K is the free convective heat transfer coefficient in the typical room conditions (CIBSE GUIDE, 1986) which were applied in this study. The air temperature was set at 20.0°C and 20.5°C.

Depending on the wind speed from 1 to 10m/s, 12.5 to 50.0W/m^{2}K (BS EN ISO 6946:1997: (*'Building components and building elements – Thermal resistance and thermal transmittance – calculation method'*)) might be a reasonable range of convective heat transfer coefficients to expect when the dual-probe is used in the field.

The simulation results of testing the convective heat transfer effect are shown in Table 4.4. Free convective heat transfer did not significantly affect the maximum temperature rise when the convection heat transfer coefficient changed from 0 to 4W/m^{2}K. The maximum temperature rise decreased from 1.21°C to 1.18°C to 1.16°C when the convective heat transfer coefficient increased from 4W/m^{2}K to 50W/m^{2}K to 100W/m^{2}K.

Table 4.4 The effect of convection heat transfer on the maximum temperature rise

Energy input (J/m)	Parameters			Numerical results
	Model	Convection coefficient (W/m^{2}K)	Air temperature (°C)	ΔT_m (K)
700	3D A	0	20.0	1.21
		4	20.0	1.21
		4	20.5	1.21
		50	20.0	1.18
		100	20.5	1.16

Analysis of the above FE results indicated that free convective heat transfer did not significantly affect the maximum temperature rise when the dual-probe was used in typical room conditions.

4.5.4 Summary of Parameter Sensitivity Testing

Confidence in the FE models was improved by testing the 2D and 3D models with different parameters. The results of parameter sensitivity testing are summarized:

- The time step did have an impact on the maximum temperature rise. 0.01s was chosen as a suitable time step used to test the 2D and 3D models.
- The transient simulation algorithms of the backward and backward-forward methods appear to be suitable for these 2D and 3D models. All the 2D and 3D models were tested using the backward algorithm.

- Surface free convective heat transfer coefficient did not affect the maximum temperature rise under typical internal room conditions.

4.6 Finite Element Modelling with a Probe Spacing of 6mm

Previous studies demonstrated that the soil thermal properties of thermal conductivity, thermal diffusivity and volumetric heat capacity as well as the moisture content were measured successfully by the dual-probe with a spacing of 6mm (Campbell *et al.*, 1991; Bristow *et al.*, 1993 and 1994; Tarara and Ham, 1997). As the start point of this work, 2D and 3D models with a spacing of 6mm were thus initially tested. The 2D and 3D models, excluding the probe material, showed good agreement with the theoretical solution. The FE procedures to design the dual-probe were therefore established and could be used for optimisation of the probe design. This is the aim of testing of the FE model with a probe spacing of 6mm.

4.6.1 Two Dimensional Models

The two dimensional models consider heat transfer only in the wall plane, assuming infinite thickness, i.e., there are no temperature differences into the wall thickness. This corresponds to the analytical model mentioned earlier (Chapter 3). A part of the 2D FE model, showing the mesh area around the needles, is presented in Figure 4.3. Very fine meshing can be seen, with the whole model being sufficiently large to ensure that no significant temperature rise is predicted at its periphery during the simulated period. In this case, the boundary was 20mm away from the centres of the heating needle and

temperature sensor needle. The element length used in this 2D model was 0.06mm with a time step of 0.0015s. The model consists of 14814 four-node quadrilateral elements and 26 three-node triangular elements, having a total of 15600 nodes. Due to the symmetry involved, it was sufficient to model only the upper half of the domain.

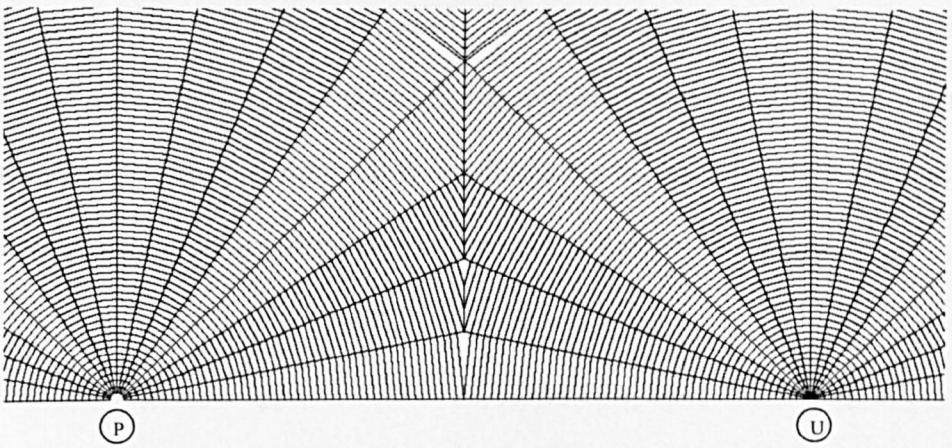

Figure 4.3 A detail part of the 2D FE model with a probe spacing of 6mm

In Figure 4.3, position P indicates the location of the heating needle, and position U indicates the location of the temperature sensor needle. In this case the two needles are 6mm apart (distance between the centres). In the first instance, the metal of the needles was not modelled (i.e., the 'needles' were assumed to have the same properties as the wall material). As noted in Section 4.4, this enabled direct comparison of temperature rises with the analytical solution. The energy input was modelled as a surface thermal flux applied at the semi-cylindrical surface at the position of the heating needle. This energy input was chosen for each material such that a similar temperature rise of approximately 1°C occurred in each case. The range of the maximum temperature rise was addressed by Bristow *et al.* (1995). The heat and moisture transfer model (Section 4.3) also verified that moisture migration within each test material under such an energy input with approximately 1°C maximum temperature rise was insignificant. By choosing the energy input with the temperature rise of approximately 1°C, from the model simulation results, a

relatively sharp peak temperature could be detected at the temperature sensor needle. Brick, aerated concrete type A and cast concrete were tested (Table 4.1 provides details of the relevant thermal properties of these materials, including the stainless steel of the needles themselves (Incropera *et al.*, 1985; CIBSE GUIDE, 1986)).

As the start point of this work, cast concrete was used as the material tested initially in the 2D and 3D models. Then, the work concentrated on aerated concrete (which, as the work progressed, seemed a more likely candidate for the measurement element of this project). More models used in testing aerated concrete are given in Chapter 5.

Some examples of typical results are shown in the plots in Figures 4.4 and 4.5 (cast concrete - 6mm needle spacing). Figure 4.4 shows the temperature rise of the heating needle, for the 2D FE model with 10 seconds heating time ('impulse duration'). The heating period can be clearly seen.

The typical temperature change at the position of the temperature sensor needle is shown in Figure 4.5.

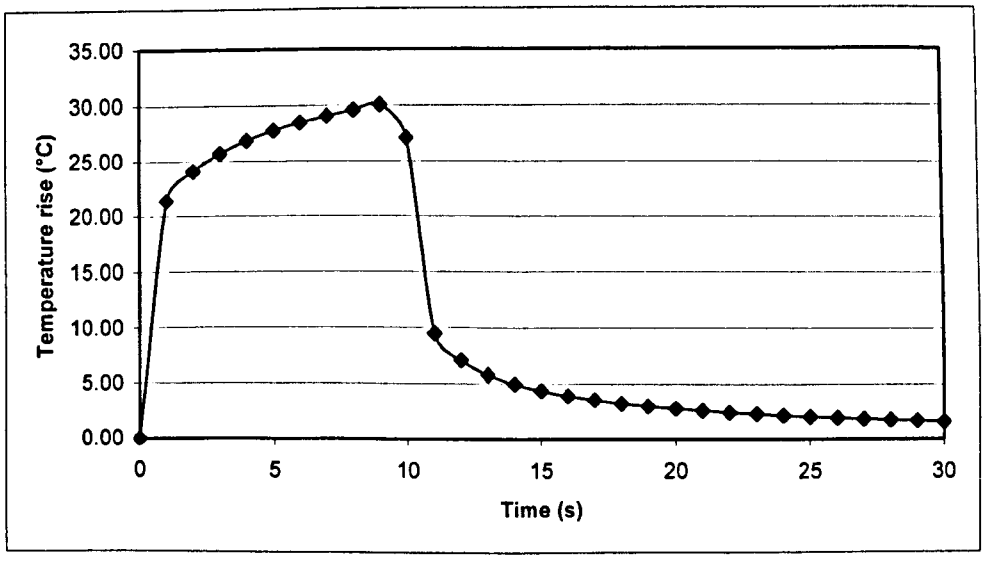

Figure 4.4 Temperature history plot at the position of the heating needle

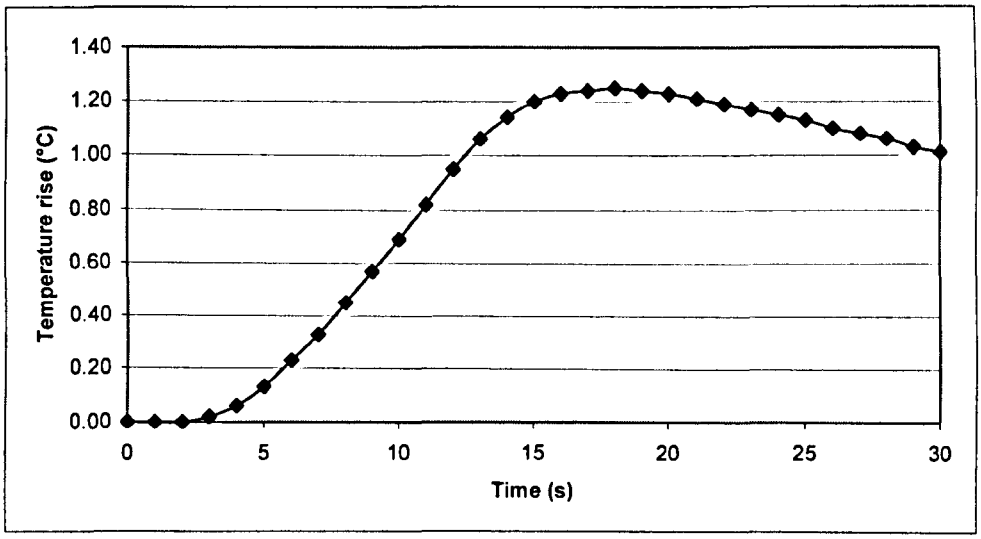

Figure 4.5 Temperature history plot at the position of the temperature sensor needle

Some initial modelling with cast concrete was then also undertaken to investigate the effect of the metal needles on the FE predicted maximum temperature rise. The outer and inner diameters of the needle were simulated as 1.56mm and 0.52mm, respectively. The element length and the time step used for this model were determined by the Fourier number and were the same for both the cast concrete and the stainless steel.

Based on the calculation of the Fourier number, i.e., the Fourier number and time step for both elements of cast concrete and the stainless steel were the same, the element lengths of the cast concrete and the stainless steel were 0.06mm and 0.13mm, respectively. The time step was determined to be 0.0015s.

4.6.2 Three Dimensional Models

A series of 3D FE models were constructed and analysed. Obviously, these models are much more complex to design, requiring more time and computer resources. Again, the actual needles were not initially modelled first. This enabled direct comparison of

temperature rises with the 2D model and an analytical solution. The 3D FE model (3D Model A) is shown in Figure 4.6 with an example of a simulation result (temperature contour plot at 10 seconds). Note the high temperature along the heating needle (corresponding to the position P in Figure 4.3). The dark semi-circle at the 'entrance' position (front wall surface) of the temperature needle (corresponding to the position U in Figure 4.3) is a consequence of high mesh density, not temperature rise.

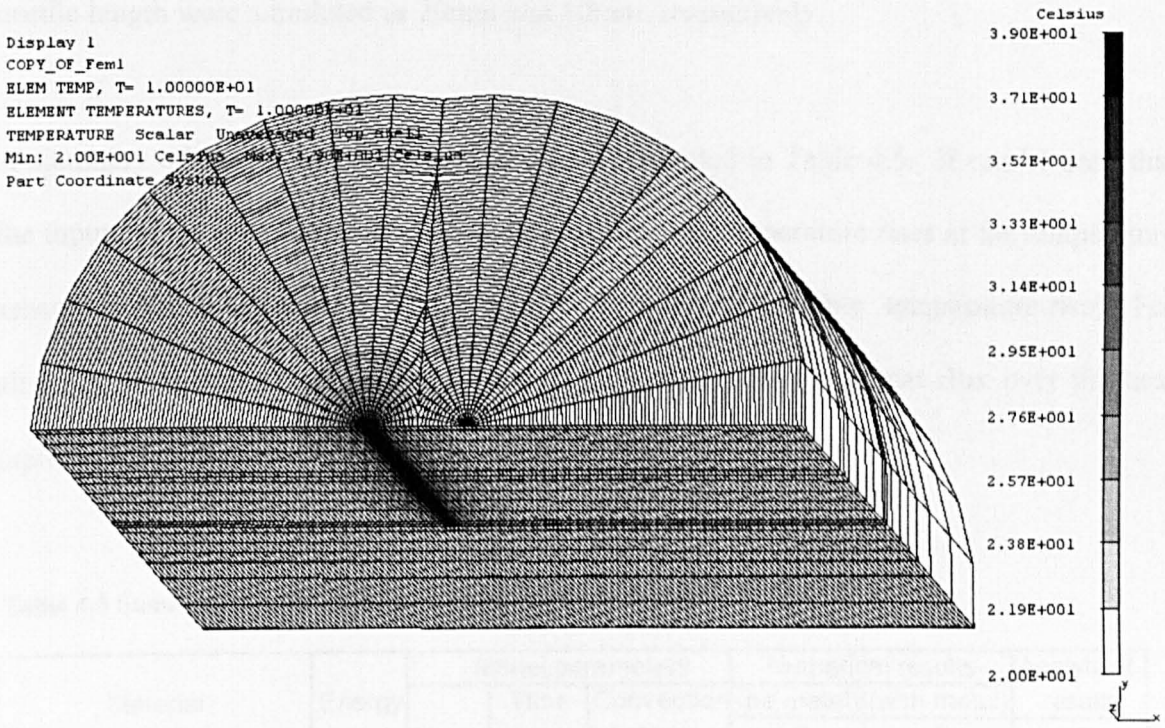

Figure 4.6 Temperature contour plot for the 3D FE model at 10s

It can be seen (Figure 4.6) that the mesh density changes in the direction of wall thickness (z-direction) in order to incorporate accurately the influence of the front wall surface boundary condition (convective heat losses) and the influence of the ends of temperature and heating needles. As with the 2D model, it was sufficient to model only the upper half of the actual 'wall', due to the symmetry. The same basic model geometry and boundary conditions were maintained as for the 2D FE models. The sensitivity of the simulations to the convective heat transfer coefficient at the front wall surface was investigated. Considering the 3D model in full detail would require more substantial computer resources

than were available for this project. The element length used in this model was 0.25mm. The model, however, was relatively complex, consisting of 51585 elements and 39090 nodes.

Some initial modelling with cast concrete (3D Model B) was then also undertaken to investigate the effects of the metal of the needles. The outer and inner diameters of the needle were simulated as 1.5mm and 0.5mm. The heating needle and temperature sensor needle length were simulated as 20mm and 10mm, respectively.

A summary of the FE and analytical results is presented in Table 4.5. It can be seen that the input energy was varied in order to achieve similar temperature rises at the temperature sensor needle, of the order of 1°C. (i.e., a realistically 'measurable' temperature rise). For all FE models the input energy was used to calculate a uniform heat flux over the heat input area (heating needle), over the period of 10s.

Table 4.5 Summary results of the probe spacing 6mm model

Material	Energy input (J/m)	Model parameters			Numerical results		Analytical results
		Model	Time step (s)	Convection coefficient (W/m^2K)	(no metal) ΔT_m (K)	(with metal) ΔT_m (K)	ΔT_m (K)
Cast concrete (dense)	700	2D	0.0015	-	1.25	1.18*	1.29
		3D	0.01	0	1.23	0.93*	
		3D	0.01	4	1.23	0.93*	
Aerated concrete type A	160	2D	0.0015	-	1.23	-	1.24
		3D	0.01	0	1.21	-	
		3D	0.01	4	1.21	-	
Brickwork (out leaf)	520	2D	0.0015	-	1.22	-	1.24
		3D	0.01	0	1.20	-	
		3D	0.01	4	1.20	-	

Note:
1. * The metal effect on the probe spacing was investigated initially only via the cast concrete FE models.

The time steps used were optimised for the appropriate FE mesh (see Section 4.5.1 for detail). The convective heat transfer coefficient was applied to the front wall of the 3D

model (see Figure 4.6). The maximum temperature increase (ΔT_m) for the FE results applies to the position of the temperature sensor needle, for the 2D model. For the 3D model, the temperature sensor needle measured the temperature 10mm into the wall thickness (from the front wall face) – see Figures 1.1 and 4.6.

The simulation results of the 2D and 3D FE models show that the 2D model, excluding the probe material, achieves good agreement with the analytical solution. Thus, reliable FE modelling procedures have been established. The 3D models, excluding the probe material, also show good agreement with the analytical solution. The effects of 3D heat flows and the sensitivity to boundary conditions are thus not significant for these cases.

The preliminary 2D modelling of the stainless steel of the probes indicates that the material of the needles does, as expected, impact upon the accuracy of the results. However, even for the spacing of 6mm which was considered (which would need to be optimised), the additional error is only in the order of 5%. The additional error is 2.3% for the 3D model. The optimisation of the spacing is discussed in Chapter 5.

As a result of the work that has been undertaken, confidence has been gained that the dual-probe approach is indeed applicable to typical building fabrics. The results show that a proven FE modelling procedure is now available. This FE modelling procedure can now be used to *optimise* the design of the dual-probe.

Chapter 5

Optimization of the Dual-probe Design

5.1 Introduction

The 2D model with a probe spacing of 6mm (but without the simulation of the specific probe material) successfully demonstrated that the FE modelling could be used to simulate the dual-probe heat transfer within the building fabric (see Chapter 4). This chapter deals with the *optimization* of the dual-probe design. Firstly, the probe spacing was tested by the 2D models (in which the metal needles *were* now included in the simulations). Secondly, based on the 2D models with a successful probe *spacing* design, a series of 3D models, with probe length varying from 40mm to 60mm, were tested to optimize the *lengths* of the heating needle and temperature sensor needle. A paper relating to the work in Chapter 5 described has been published (Ye *et al.*, 2004).

It has previously been shown that the metal tubing has a significant effect on the probe spacing design (Section 4.6). To reduce the effect of the metal, a larger probe spacing must be applied to the model. A model with a probe spacing of 20mm was the first successfully tested model in which the metal tubing was included. Thus, the optimization of the dual-probe design began with a probe spacing of 20mm. To avoid repetition, the models with a probe spacing of 20mm are initially described in detail. The method of construction of other models with different probe spacings was identical. Aerated concrete types A (CIBSE GIUDE, 1986) and B (CELCON, 2003) were used as the test material because of the ease with which they could be cut and drilled.

5.2 Criteria for Optimization of the Dual-probe Design

The aim of the optimization of the dual-probe design is to obtain the optimal combination of probe spacing and probe length. Two aspects for probe length design were considered to determine the critical 3D FE predicted maximum temperature rise: (a) the 3D model with the longest probe predicted the maximum temperature rise closest to the analytical solution; (b) however, a shorter probe was preferred as it increased ease of insertion into the building fabric. The analytical solution of the maximum temperature rise for each model detailed in Sections 5.5 and 5.6 (Section 5.3) is 1.22°C. The criteria for a successful design of the dual-probe were that the difference between the 3D model predicted maximum temperature rise and the analytical solution should be less than 10%.

5.3 Procedures for the Optimization of the Dual-probe Design

The optimization of the dual-probe design began by considering the probe spacing. Narrower probe spacing was preferred (if possible) as less energy input was required, thus minimising the disturbance to the moisture field. The sequence for the optimization of the probe spacing was as follows. Firstly, the 2D model with metal needles of a probe spacing of 6mm was tested and the result was unsuccessful because the metal had too great an effect on the results (Section 4.6.1). Secondly, to reduce the effect of the metal, the 2D model with a larger probe spacing of 20mm was tested and was successful. Thirdly, 2D models with probe spacing of 18mm, 16mm, 14mm, 12mm and 9mm were tested in an attempt to minimize the probe spacing. The 2D model with a probe spacing of 9mm was tested unsuccessfully because the maximum temperature rise was less than 1.10°C.

A shorter probe length was preferable to a longer probe length due to increased ease of insertion into the building fabric. The probe length was tested in the range from 40mm to 60mm. The procedures for the optimization of the probe length were as follows. Firstly, based on each 2D model with successfully designed probe spacing, the probe length of 60mm was tested successfully. Secondly, the 3D model with a probe length of 50mm was tested successfully. Thirdly, the 3D model with a probe length of 45mm or 40mm was tested until it was unsuccessful because the maximum temperature rise was less than 1.10°C.

5.4 General Aspects of the Models for Probe Design Optimization

To construct either 2D models or 3D models, the model had to be meshed first. The mesh procedures for the construction of 2D or 3D models were:

1. The construction of a 2D shell mesh in the OSS'O' plane is shown in Figure 5.1. In Figure 5.1, Q is the centre of the OS line. P is the point at which the central axis of the heating needle (P'' to P''') meets the line OS. The length of OP was chosen so that the temperature at point O did not increase during the period when the maximum temperature rise was recorded along UU' when a heat pulse was applied to the heating needle. PQ is the symmetric line of the 2D shell mesh. Thus, PQ is half of the dual-probe spacing. Firstly, a cylindrical coordinate with origin at point P was set up so that a 2D shell mesh was constructed using this cylindrical coordinate within the area SPP'S'. Detailed element lengths in each model are given in Sections 4.6.1, 5.5.1, 5.6.1, 5.6.2, 5.6.3, 5.6.4 and 5.6.5. Secondly, another part of the 2D shell mesh was constructed within the area OPP'O'. This was done

by reflecting the 2D shell mesh within the area SPP'S' along the symmetry axis PP'. Thirdly, one element was separated into two elements along the QQ' line. All the element points on the right side of the QQ' line were deleted. Finally, the full shell mesh elements were obtained by reflecting the 2D shell mesh elements in the QQ'O'O area along the axis QQ'. U is the projection of the temperature sensor needle and U is the symmetry of P along Q.

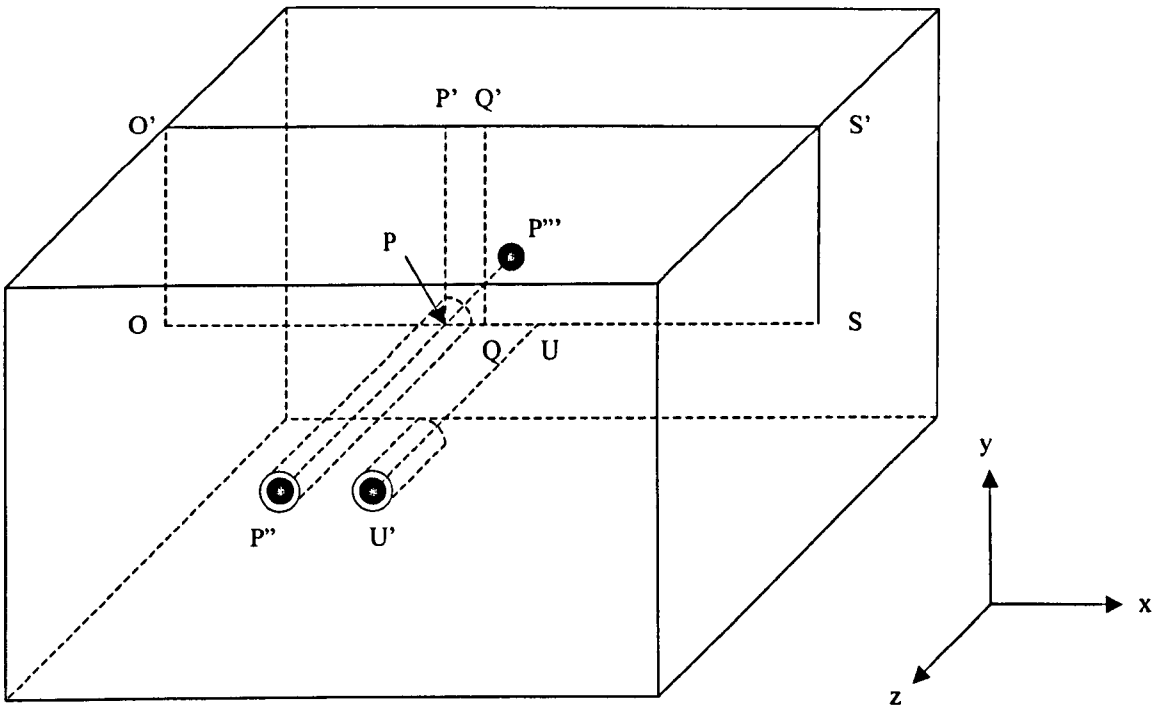

Figure 5.1 Schematic diagram of mesh construction procedure. The element lengths and the corresponding locations are shown in Figures 5.2, 5.6-5.10, 5.13, 5.16-5.19, 5.22 and 5.25.

2. Construction of the 2D or 3D models' mesh.

(1). A 2D model mesh was constructed by extruding the shell mesh into solid elements along the z-direction. Extrusion length was 0.25mm, which was the same as the element length used in the temperature measurement points at x-direction.

(2). A 3D model mesh was constructed by extruding the shell mesh into solid elements along the z-direction as shown in Figure 5.1. Extrusion length PP" is the

heating needle length. Then, the shell mesh was extruded into solid elements along the -z-direction as shown in Figure 5.1. Extrusion length PP''' was determined by the FE model so that the predicted temperature did not change at point P''' when the energy pulse was applied. Due to the 3D model needing more computer resources, varied element lengths were used. A shorter element length was used in the temperature measurement points. Otherwise, a longer element length was applied. Detailed element lengths along the z-direction are given in Sections 5.5.2, 5.6.1, 5.6.2, 5.6.3 and 5.6.4.

After the model was meshed, boundary conditions, which were heat flux, initial temperature of the model and convective heat transfer coefficient for 3D model, were applied to the model. The temperature distribution of the test sample was obtained by running the FE model.

Although the probe spacing was varied, the boundary conditions for the 2D models with varied probe spacings from 9mm to 20mm were the same as for the 2D model with a probe spacing of 6mm. The boundary conditions for the 3D models with varied probe spacings from 12mm to 20mm were the same as for the 3D model with a probe spacing of 6mm.

As mentioned in Section 4.6.1, a certain amount of energy input was chosen so that in both the 2D and 3D models, the predicted maximum temperature rises was approximately 1°C. In the first instance, an energy pulse of 1750J/m was input to the 2D model with a probe spacing of 20mm. The analytical solution of the maximum temperature rise was 1.22°C with this amount of energy input. For consistency, the same maximum temperature rise was used for all the probe designs. The energy input was chosen for each 2D model and the corresponding 3D model so that a theoretically calculated maximum temperature rise of approximately 1.22°C occurred in each model simulation. The inner and outer

diameters of the heating and temperature sensor needles were simulated as 0.5mm and 1.5mm, respectively. For the 3D model with a probe spacing of 12mm, the length of the temperature sensor needle was simulated as half of the heating needle length and one third of the heating needle length. For other 3D models, the length of the temperature sensor needle was simulated as half of the heating needle length. The aerated concrete type A and stainless steel were tested in the 2D and 3D models with probe spacings of 20mm, 18mm, 16mm and 14mm. The aerated concrete type B was selected as the experimental material because of its thermal and mechanical properties. The aerated concrete type B and stainless steel were tested in the 2D and 3D models with probe spacings of 16mm, 14mm, 12mm and 9mm. The thermal properties of these materials (Incropera *et al.*, 1985; CIBSE GUIDE, 1986; CELCON, 2003) are shown in Table 5.1. Due to the symmetry involved, it was sufficient to model only the upper half of the domain for both the 2D and 3D models. The time step used for all the 2D and 3D models was 0.01s. Free convective heat transfer in the front surface of the dual-probe was simulated as $4 W/m^2K$.

Table 5.1 Material properties for optimization of the dual-probe design

Material	Density (kg/m^3)	Thermal conductivity (W/mK)	Specific heat capacity (J/kgK)
Aerated concrete type A	500	0.16	840
Aerated concrete type B	620	0.15	1050
Stainless steel AISI 304	7900	14.90	477

The 2D models were used to optimise the probe spacings from 20mm, 18mm, 16mm, 14mm, 12mm, to 9mm. The 3D models were used to optimise the probe lengths from 60mm, 50mm, 45mm, to 40mm. Details of the optimisation of the probe spacing and length are described in Sections 5.5 to 5.7.

5.5 Finite Element Modelling with a Probe Spacing of 20mm

This section relates to the 2D and 3D modelling of aerated concrete type A using a probe spacing of 20mm.

5.5.1 Two Dimensional Model

In Section 4.6.1, the 2D model with a probe spacing of 6mm was tested. The FE predicted maximum temperature rise agreed well with the analytical solution. However, when the stainless steel needles were included in the model, the FE predicted maximum temperature rise was significantly lower than the analytical one. Thus, the probe spacing of the 2D models was varied in an attempt to produce a probe spacing design in which the effect of the stainless steel is negligible.

Initially, a 2D model with element length of 0.25mm was tested. The FE model predicted a maximum temperature rise which agreed well with the analytical solution. This indicated that the probe spacing of 20mm was designed successfully. However, when a 3D model with a heating needle length of 60mm was constructed based on this 2D model, the 3D model could not be run as the computer resources were insufficient. For consistency, the 3D model element lengths in x and y-directions were the same as the 2D model. To reduce the number of elements, a 2D model with varied element lengths was tested. The element lengths and the corresponding locations are shown in Figure 5.2. The maximum temperature rise predicted by these two 2D models was 1.16°C which was 0.06°C lower than that of the analytical solution. A part of the 2D FE model with varied element length, the mesh area around the needles, is presented in Figure 5.3. In Figure 5.3, position P

indicates the location of the heating needle, and position U indicates the position of the temperature sensor needle. Very fine meshing can be observed around the area of the needles, with the whole model being sufficiently large to ensure that no significant temperature rise is predicted at its periphery during the simulation period. In this case, the boundary was at 65mm away from the centres of the heating needle and temperature sensor needle. The mesh density was lower in the area far away from the needles. The model consisted of 3726 four-node quadrilateral elements and 30 three-node triangular elements, with a total of 3958 nodes. Figures 5.4 and 5.5 show the temperature changes at the heating needle and the temperature sensor needle.

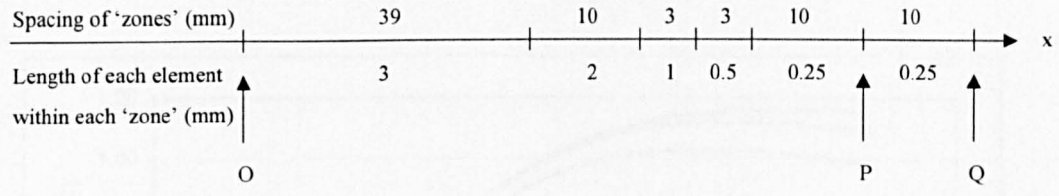

Figure 5.2 The element length and the corresponding location of the probe spacing of a 20mm model in x-direction

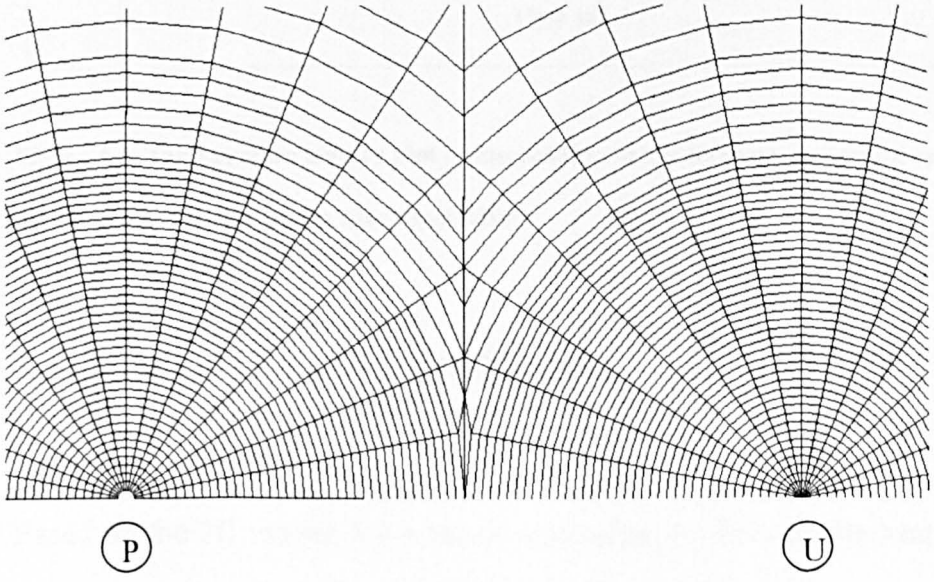

Figure 5.3 A detail part of 2D FE model of a probe spacing of a 20mm

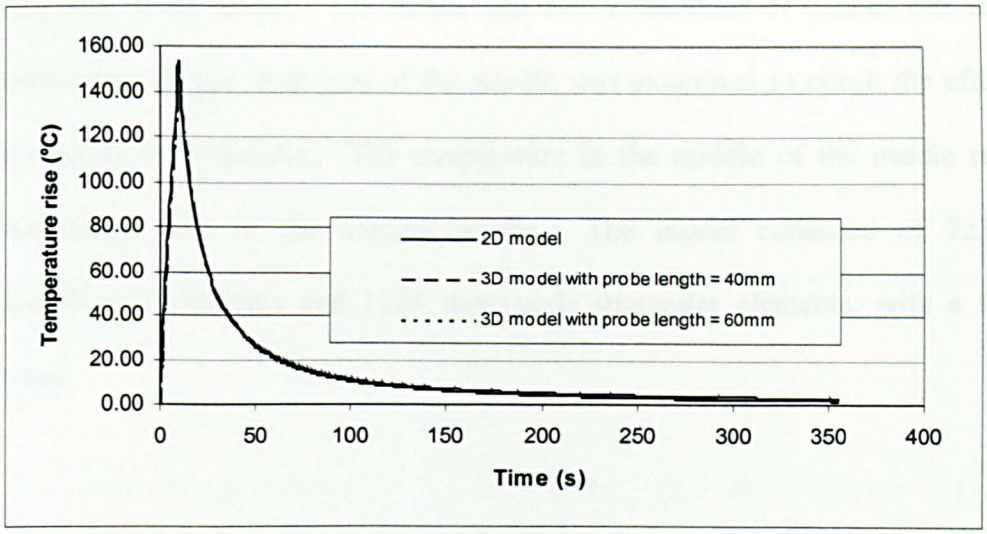

Figure 5.4 Temperature history plot at the position of the heating needle for the models with a probe spacing of 20mm (note: these three curves overlap)

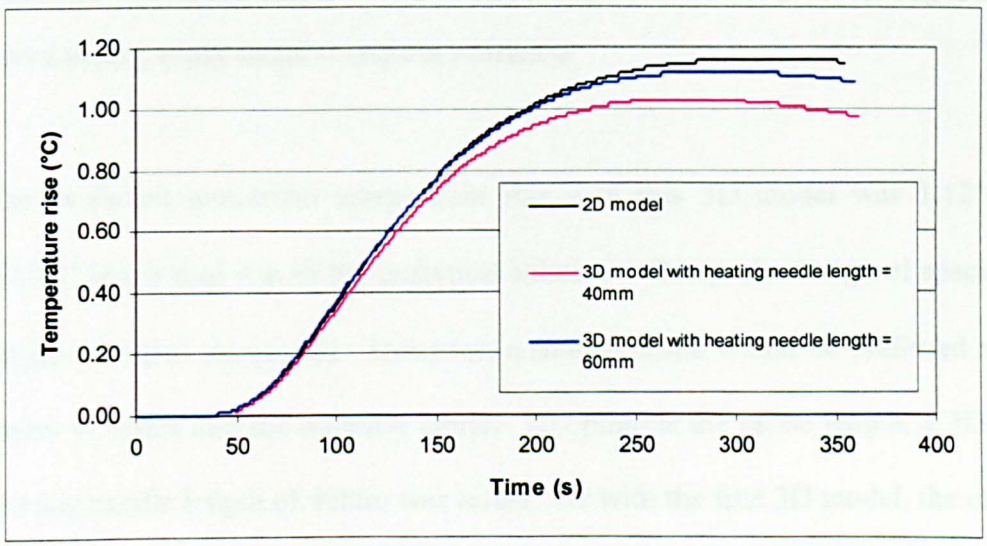

Figure 5.5 Temperature history plot at the position of the temperature sensor needle for the models with a probe spacing of 20mm

5.5.2 Three Dimensional Models

Based on the 2D model, a 3D model was tested to simulate the heating needle length of 60mm. The element lengths in the z-direction were varied. The element lengths and their locations are shown in Figure 5.6. Fine meshing was used at the end, the middle and the

front part of the needle. The needle end with a thickness of 0.5mm was simulated. The temperature of the front part of the needle was examined to check the effect of the free convective heat transfer. The temperature in the middle of the needle represented the temperature rise of the heating needle. The model consisted of 72314 four-node quadrilateral elements and 1224 three-node triangular elements, with a total of 75212 nodes.

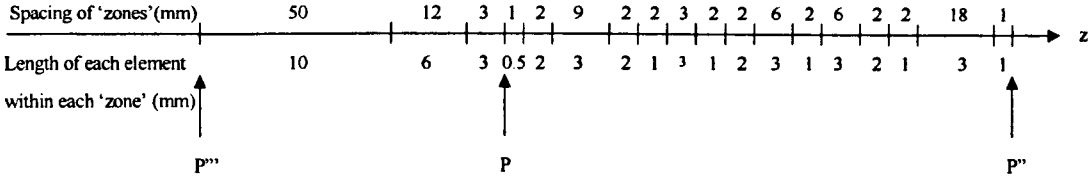

Figure 5.6 The element length and the corresponding location of the probe spacing of a 20mm model with a heating needle length of 60mm in z-direction

The predicted maximum temperature rise with this 3D model was 1.12°C which was 0.10°C lower than that of the analytical solution. This probe design of spacing and needle length was thus successful. However, a shorter probe would be preferred as it would be easier to insert into the building fabric. To optimize the probe length, a 3D model with a heating needle length of 40mm was tested. As with the first 3D model, the element lengths in the z-direction were varied. The element lengths and corresponding locations are shown in Figure 5.7. The model consisted of 57436 four-node quadrilateral elements and 1014 three-node triangular elements, with a total of 59380 nodes. The predicted maximum temperature rise with this 3D model was 1.03°C which was 0.17°C lower than that of the analytical solution. This probe design was thus 'not successful'. Thus, the successful dual-probe design with a probe spacing of 20mm was that with a heating needle length of 60mm. The temperature changes of these two 3D models at the heating needle and the temperature sensor needle are shown in Figures 5.4 and 5.5.

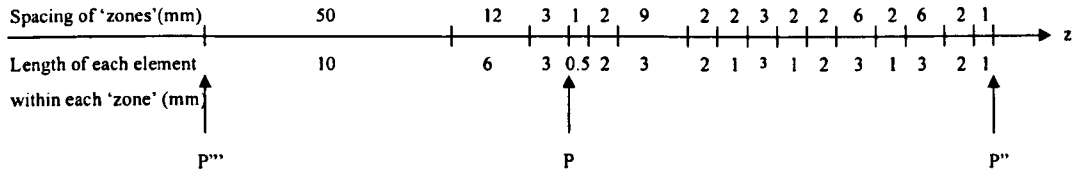

Figure 5.7 The element length and the corresponding location of the probe spacing of a 20mm model with a heating needle length of 40mm in z-direction

5.6 Finite Element Modelling with Probe Spacings of 18mm, 16mm, 14mm, 12mm and 9mm

As the previous sections noted, the process of optimising the effectiveness of the probe design began with a probe spacing of 20mm. The probe spacing was then reduced gradually to 9mm which was, however, unsuccessful. The process of construction each FE model is described in Section 5.4. The details of construction of the 2D and 3D models are given in Table 5.2. The following sections detail the modelling that was undertaken for each of the spacings.

Table 5.2 Summary of the construction of FE models

Material	Probe spacing (mm)	Model	Heating needle length (mm)	Elements		Nodes
				Four-node quadrilateral	Three-node triangular	
Aerated concrete type B	9	2D	-	2710	28	2872
Aerated concrete type B	12	2D	-	2854	30	3028
		3D	45	39692	892	40886
		3D	50	41112	922	42400
		3D*	50	41112	922	42400
Aerated concrete type B	14	2D	-	2922	30	3120
		3D	45	40868	892	42128
		3D	50	42330	922	43688
		3D	60	48178	1042	49928
Aerated concrete type A	14	2D	-	2922	30	3120
Aerated concrete type A	16	2D	-	3182	30	3382
		3D	50	49004	1014	50740
		3D	60	55340	1134	57504
Aerated concrete type B	16	3D	50	49004	1014	50740
		3D	60	55340	1134	57504
Aerated concrete type A	18	2D	-	3456	30	3674
		3D	50	53282	1014	55120
		3D	60	60170	1134	62468
Aerated concrete type A	20	2D	-	3726	30	3958
		3D	40	57436	1014	59380
		3D	60	72314	1224	75212

Note:
1. * Temperature sensor needle length was modelled as 15mm.
2. The heating needle lengths were tested at 60 and 50mm for the models with probe spacings of 18 and 16mm. The FE model results (see Table 5.3) indicated that 50mm was the optimal probe length for the models with probe spacings of 18 and 16mm when testing aerated concrete type A.
3. The heating needle length was tested at 45mm for the models with probe spacings of 14 and 12mm. The FE results (see Table 5.3) of the model with heating needle length of 50mm indicated that the heating needle length could be reduced further.

5.6.1 Finite Element Modelling with a Probe Spacing of 18mm

Aerated concrete type A was tested with the 2D and 3D models with a probe spacing of 18mm. The details of construction the 2D and 3D models are given in Table 5.2. The element lengths and the corresponding locations for construction of the 2D model are shown in Figure 5.8.

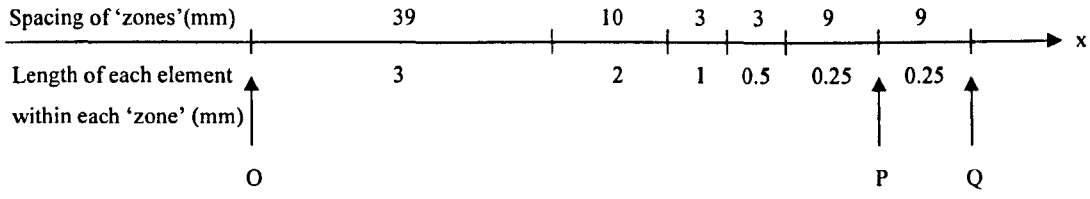

Figure 5.8 The element length and the corresponding location of the probe spacing of an 18mm model in x-direction

Based on the 2D model, a 3D model was tested to simulate the heat transfer of the dual-probe with a heating needle length of 60mm. The element lengths and the corresponding locations for construction of the 3D model are shown in Figure 5.9.

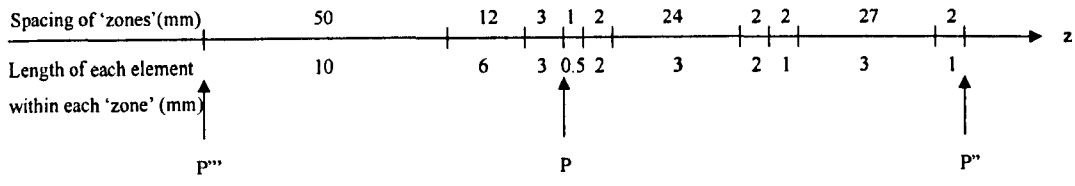

Figure 5.9 The element length and the corresponding location of the probe spacing of 18mm and 16mm models with a heating needle length of 60mm in z-direction

To further optimize the probe length, a 3D model with a heating needle length of 50mm was tested. The element lengths and the corresponding locations for construction of the 3D model are shown in Figure 5.10.

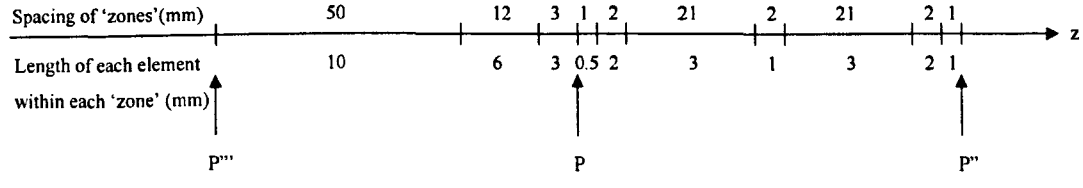

Figure 5.10 The element length and the corresponding location of the probe spacing of 18mm and 16mm models with a heating needle length of 50mm in z-direction

The temperature changes at the heating needle and the temperature sensor needle of the 2D and 3D models are shown in Figures 5.11 and 5.12. It can be seen that:

- The maximum temperature rise predicted by the 2D model was 1.15°C which was 0.07°C lower than that of the analytical solution. Thus, this probe spacing design was successful.
- The maximum temperature rise predicted by the 3D model with the heating needle length of 60mm was 1.13°C which was 0.09°C lower than that of the analytical solution. Thus, this probe length design was successful.
- The maximum temperature rise predicted by the 3D model with the heating needle length of 50mm was 1.10°C which was 0.12°C lower than that of the analytical solution. Thus, this probe length design was successful.
- Further reduction of the probe length was not undertaken, as it would result in an insufficient temperature rise compared to the analytical solution. The maximum temperature rise predicted by the 2D and 3D models was not less than 1.10°C. Thus, the successful dual-probe designs with a probe spacing of 18mm were those of the heating needle lengths of 60mm and 50mm, respectively.

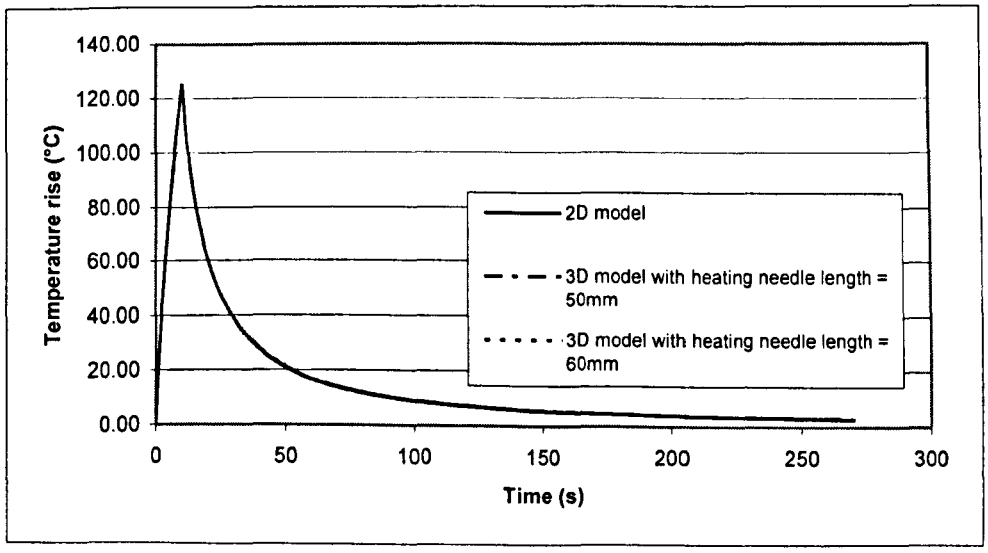

Figure 5.11 Temperature history plot at the position of the heating needle for the models with a probe spacing of 18mm (note: these three curves overlap)

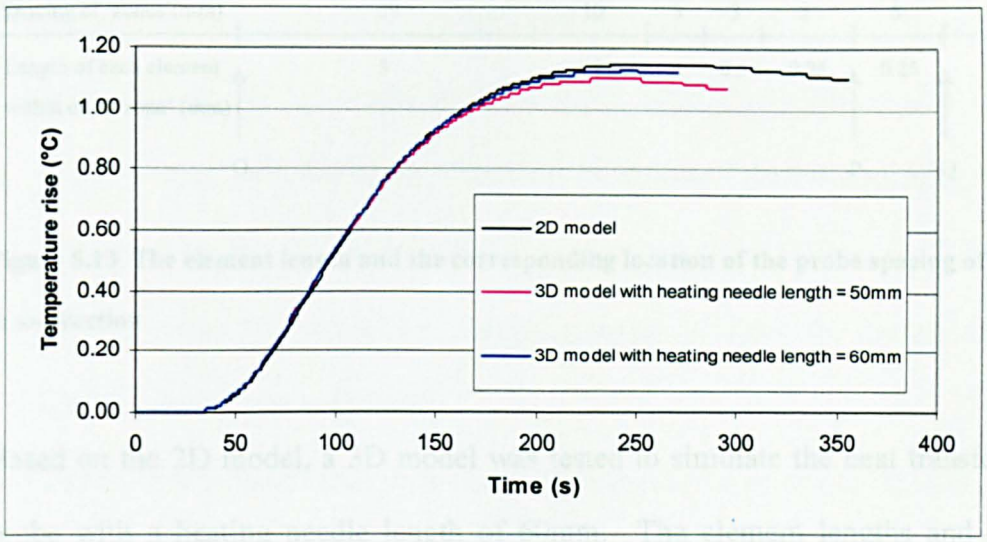

Figure 5.12 Temperature history plot at the position of the temperature sensor needle for the models with a probe spacing of 18mm

5.6.2 Finite Element Modelling with a Probe Spacing of 16mm

The 2D and 3D models with a probe spacing of 16mm were tested. Aerated concrete type A was selected as the test material first and tested with the 2D model and 3D models. Then, the modelling work moved onto testing the aerated concrete type B because it would be used in the experimental work. The probe design of spacing and needle length had to be specified to this aerated concrete. Thus, both types A and B aerated concrete were tested with the two 3D models having the heating needle length of 60mm and 50mm respectively. The details of construction the 2D and 3D models are given in Table 5.2. The element lengths and the corresponding locations for construction of the 2D model are shown in Figure 5.13.

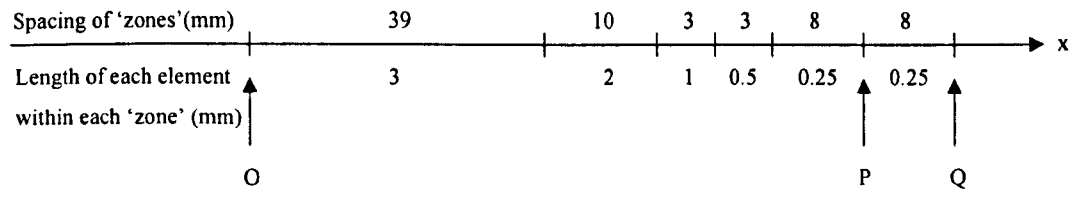

Figure 5.13 The element length and the corresponding location of the probe spacing of a 16mm model in x-direction

Based on the 2D model, a 3D model was tested to simulate the heat transfer of the dual-probe with a heating needle length of 60mm. The element lengths and corresponding locations for construction of the 3D model are shown in Figure 5.9.

To further optimize the probe length, a 3D model with a heating needle length of 50mm was tested. The element lengths and corresponding locations for construction of the 3D model are shown in Figure 5.10.

The temperature changes at the heating needle and the temperature sensor needle of the 2D and 3D models are shown in Figures 5.14 and 5.15. It can be seen that:

- The maximum temperature rise predicted by the 2D model was 1.14°C which was 0.08°C lower than that of the analytical solution. Thus, this probe spacing design was successful.
- With reference to the test of aerated concrete type A (a) the maximum temperature rise predicted by the 3D model with the probe length of 60mm was 1.12°C which was 0.10°C lower than that of the analytical solution (b) the maximum temperature rise predicted by the 3D model with the probe length of 50mm was 1.10°C which was 0.12°C lower than that of the analytical solution. Thus, the design using these probe lengths was successful.

- With reference to the test of aerated concrete type B (a) the maximum temperature rise predicted by the 3D model with the probe length of 60mm was 1.15°C which was 0.07°C lower than that of the analytical solution and (b) the maximum temperature rise predicted by the 3D model with the probe length of 50mm was 1.13°C which was 0.09°C lower than that of the analytical solution. Thus, the design using these probe lengths design was successful.
- Further reduction of the probe length with the model of testing aerated concrete type A was not undertaken, as it would result in an insufficient temperature rise compared to the analytical solution. Further reduction of the probe length with the model of testing aerated concrete type B was not undertaken, as the FE results indicated that it was possible to obtain a narrower probe spacing. The maximum temperature rise predicted by the 2D and 3D models was not less than 1.10°C. Thus, the successful dual-probe designs with a probe spacing of 16mm were those with heating needle lengths of 60mm and 50mm for types A and B of aerated concrete.

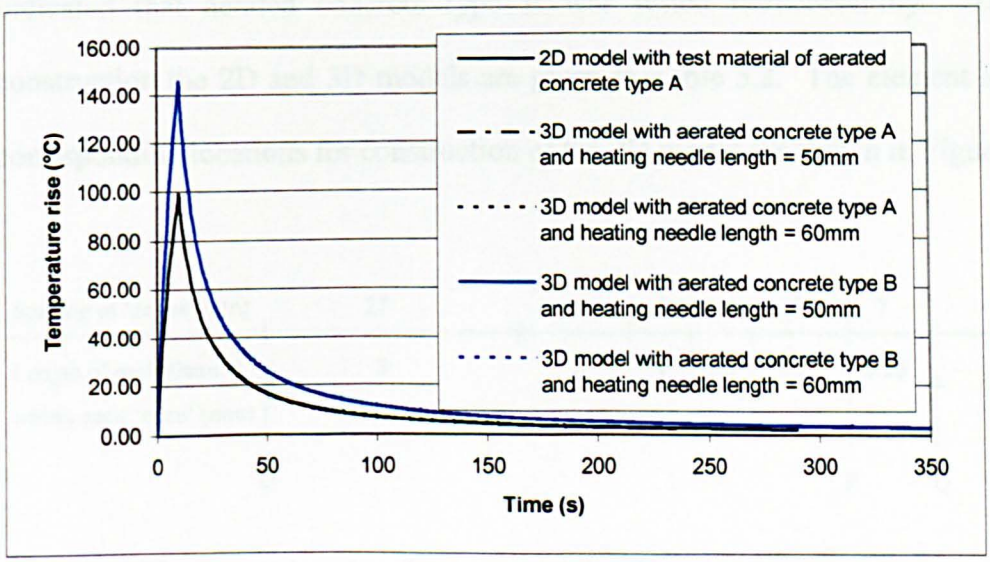

Figure 5.14 Temperature history plot at the position of the heating needle for the models with a probe spacing of 16mm (note: three curves with testing aerated concrete type A overlap and two curves with testing aerated concrete type B overlap)

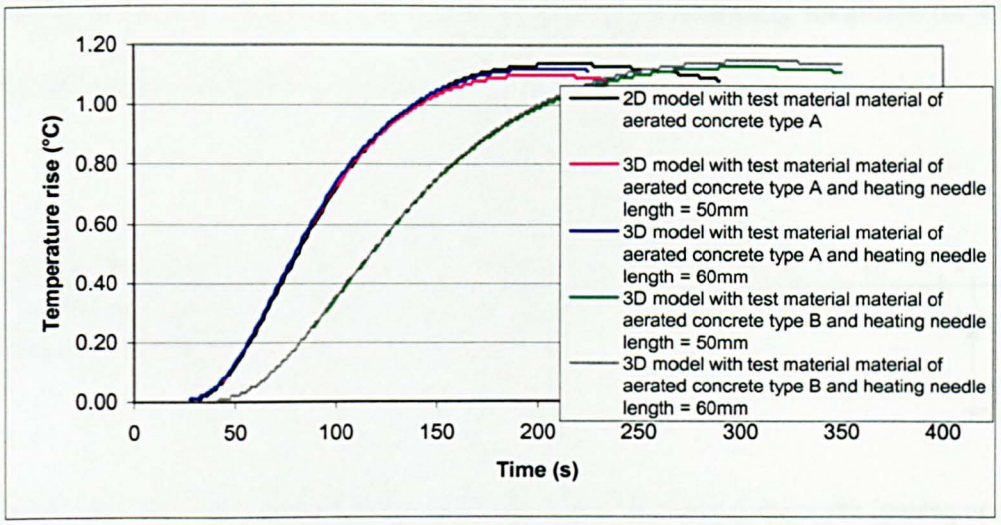

Figure 5.15 Temperature history plot at the position of the temperature sensor needle for the models with a probe spacing of 16mm

5.6.3 Finite Element Modelling with a Probe Spacing of 14mm

Types A and B of aerated concrete were tested with the 2D models. The 3D models concentrated on testing aerated concrete type B because the 2D model results (see below) indicated that aerated concrete type A was tested unsuccessfully. The details for construction the 2D and 3D models are given in Table 5.2. The element lengths and the corresponding locations for construction of the 2D model are shown in Figure 5.16.

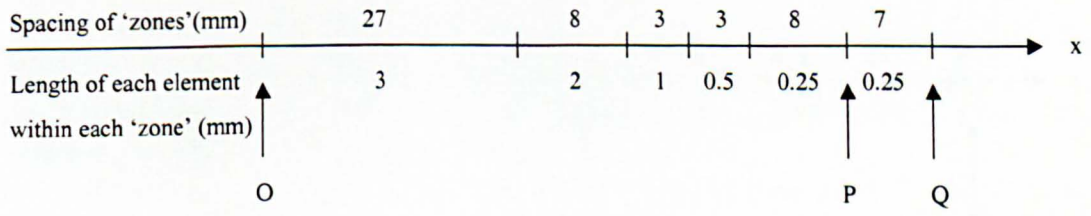

Figure 5.16 The element length and the corresponding location of the probe spacing of a 14mm model in x-direction

Based on the 2D model tested with the aerated concrete type B and stainless steel, a 3D model was tested to simulate the heat transfer of the dual-probe with a heating needle

length of 60mm. The element lengths and the corresponding locations for construction of the 3D model are shown in Figure 5.17.

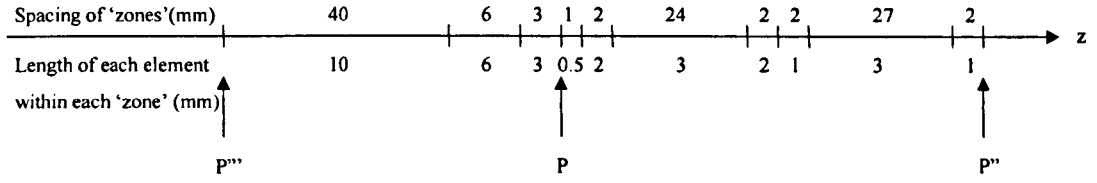

Figure 5.17 The element length and the corresponding location of the probe spacing of a 14mm model with a heating needle length of 60mm in z-direction

To further optimize the probe length, two 3D models with heating needle lengths of 50mm and 45mm were tested. The element lengths and the corresponding locations for construction of the 3D models are shown in Figures 5.18 and 5.19.

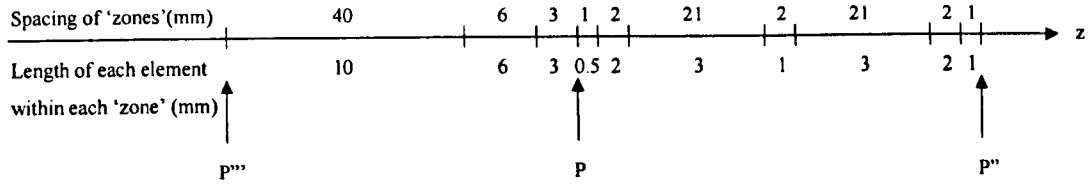

Figure 5.18 The element length and the corresponding location of the probe spacing of 14mm and 12mm models with a heating needle length of 50mm in z-direction

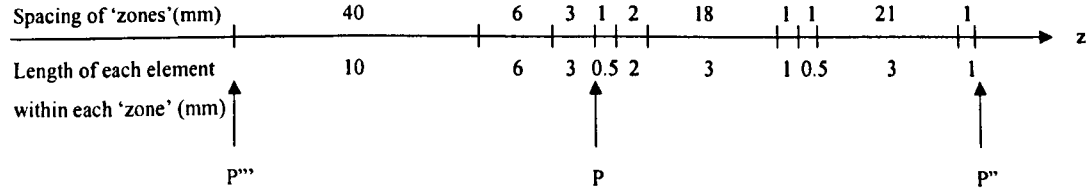

Figure 5.19 The element length and the corresponding location of the probe spacing of 14mm and 12mm models with a heating needle length of 45mm in z-direction

The temperature changes at the heating needle and the temperature sensor needle of the 2D and 3D models are shown in Figures 5.20 and 5.21. It can be seen that:

- The maximum temperature rise predicted by the 2D model to test aerated concrete type A was 1.12°C which was 0.10°C lower than that of the analytical solution. This probe spacing design was thus 'not successful' because the 3D model results would be worse than the 2D model ones which would lead to an insufficient maximum temperature rise compared to the analytical solution.
- The maximum temperature rise predicted by the 2D model to test aerated concrete type B was 1.16°C which was 0.06°C lower than that of the analytical solution. Thus, this probe spacing design was successful.
- The maximum temperature rise predicted by the 3D model with a heating needle length of 60mm was 1.14°C which was 0.08°C lower than that of the analytical solution. Thus, this probe length design was successful.
- The maximum temperature rise predicted by the 3D model with a heating needle length of 50mm was 1.13°C which was 0.09°C lower than that of the analytical solution. Thus, this probe length design was successful.
- The maximum temperature rise predicted by the 3D model with a heating needle length of 45mm was 1.12°C which was 0.10°C lower than that of the analytical solution. Thus, this probe length design was successful.
- Further reduction of the probe length was not undertaken, as the results indicated that it was possible to obtain a narrower probe spacing. The maximum temperature rise predicted by the 2D and 3D models for testing the aerated concrete type B was not less than 1.10°C. Thus, the successful dual-probe designs with a probe spacing of 14mm were those with heating needle lengths of 60mm, 50mm and 45mm, respectively.

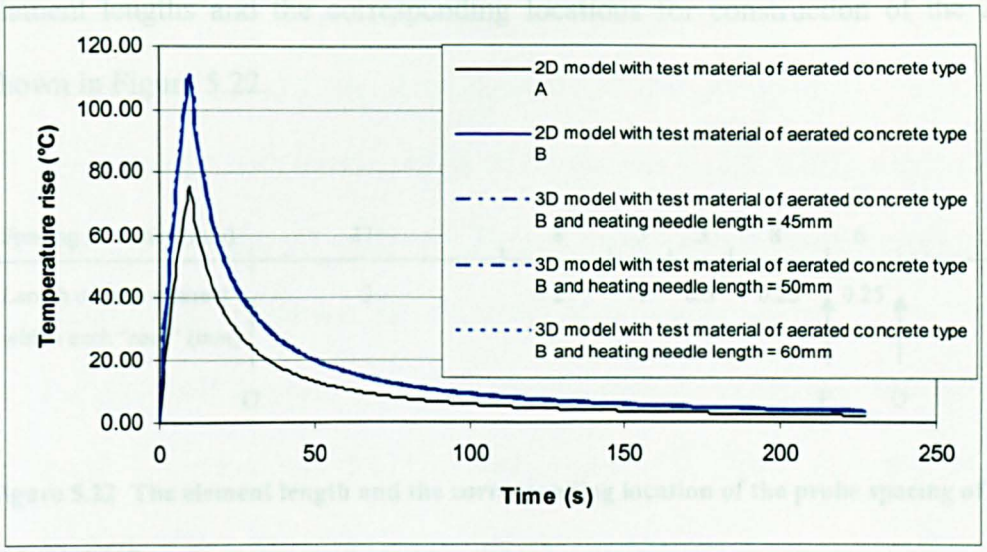

Figure 5.20 Temperature history plot at the position of the heating needle for the models with a probe spacing of 14mm (note: four curves with testing aerated concrete type B overlap)

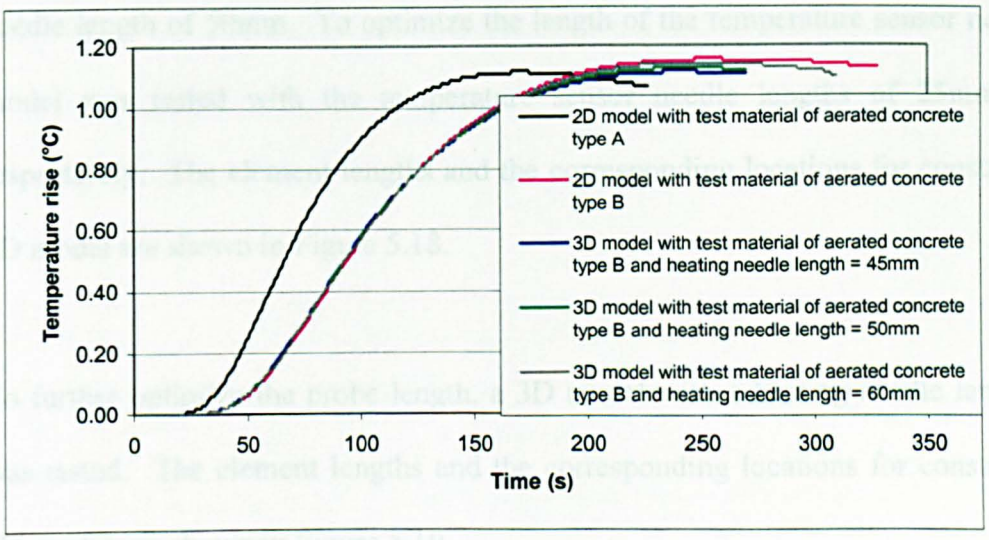

Figure 5.21 Temperature history plot at the position of the temperature sensor needle for the models with a probe spacing of 14mm

5.6.4 Finite Element Modelling with a Probe Spacing of 12mm

Aerated concrete type B was tested in the 2D and 3D models with a probe spacing of 12mm. The details of construction for the 2D and 3D models are given in Table 5.2. The

element lengths and the corresponding locations for construction of the 2D model are shown in Figure 5.22.

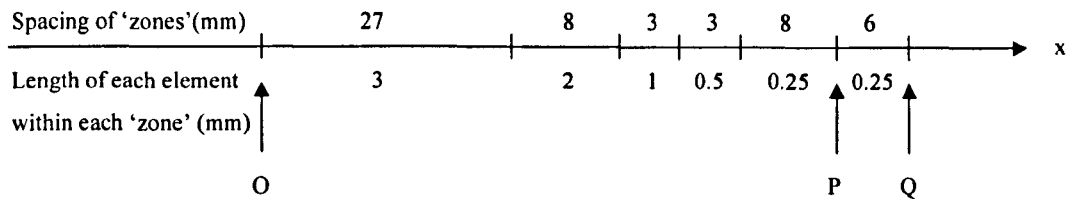

Figure 5.22 The element length and the corresponding location of the probe spacing of a 12mm model in x-direction

From previous 3D models results (Sections 5.6.1 to 5.6.3), it can be seen that the optimal heating needle length is 50mm. Thus, the first 3D model was tested to simulate a heating needle length of 50mm. To optimize the length of the temperature sensor needle, this 3D model was tested with the temperature sensor needle lengths of 25mm and 15mm respectively. The element lengths and the corresponding locations for construction of the 3D model are shown in Figure 5.18.

To further optimize the probe length, a 3D model with a heating needle length of 45mm was tested. The element lengths and the corresponding locations for construction of the 3D model are shown in Figure 5.19.

The temperature changes at the heating needle and the temperature sensor needle of the 2D and 3D models are shown in Figures 5.23 and 5.24. It can be seen that:

- The maximum temperature rise predicted by the 2D model was 1.13°C which was 0.09°C lower than that of the analytical solution. Thus, this probe spacing design was successful.
- With reference to the 3D model tests having a heating needle length of 50mm (a) the maximum temperature rise predicted by the 3D model with a temperature sensor needle

length of 25mm was 1.12°C which was 0.10°C lower than that of the analytical solution and (b) the maximum temperature rise predicted by the 3D model with a temperature sensor needle length of 15mm was 1.10°C which was 0.12°C lower than that of the analytical solution. These results indicated that the optimal temperature sensor needle length was half the length of its heating needle.

- The predicted maximum temperature rise with the 3D model with the heating needle length of 45mm was 1.11°C which was 0.11°C lower than that of the analytical solution. Thus, this probe length design was successful.
- The maximum temperature rise predicted by the 2D and 3D models was not less than 1.10°C. The probe with a heating needle length of 45mm was the shortest successful probe design. Further reduction of the probe length was not undertaken, as it would result in an insufficient temperature rise compared to analytical solution. Thus, the successful dual-probe designs with a probe spacing of 12mm were those with heating needle lengths of 50mm and 45mm, respectively.

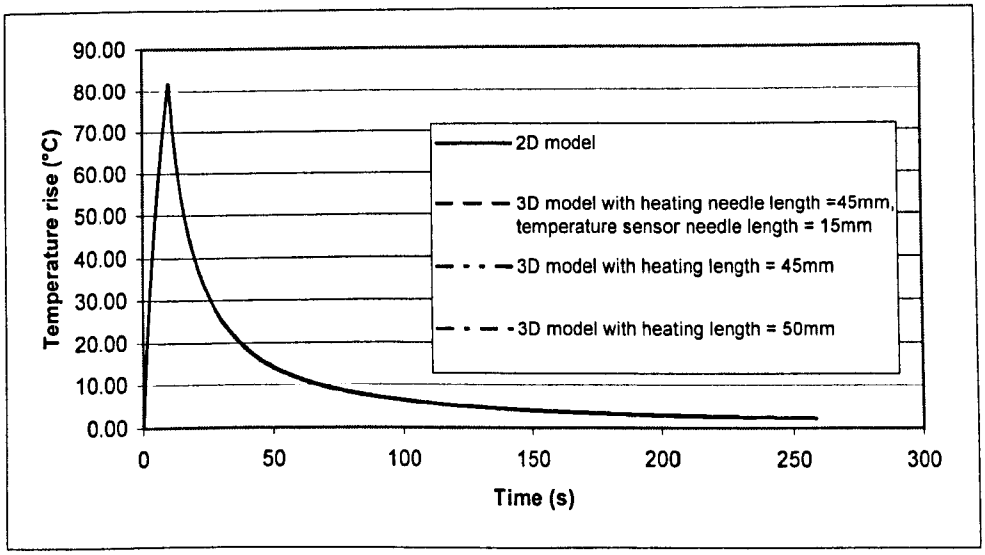

Figure 5.23 Temperature history plot at the position of the heating needle for the models with a probe spacing of 12mm (note: these four curves overlap)

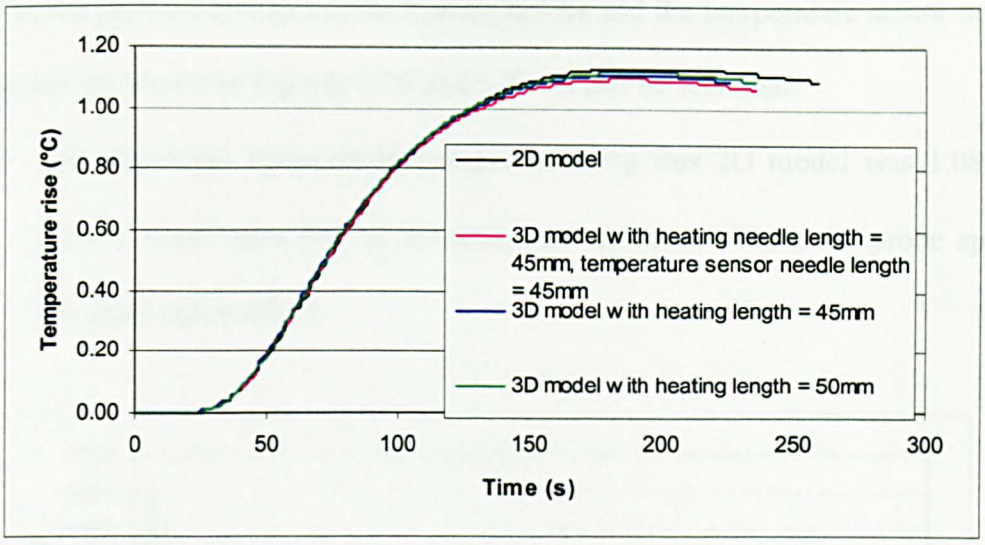

Figure 5.24 Temperature history plot at the position of the temperature sensor needle for the models with a probe spacing of 12mm

5.6.5 Finite Element Modelling with a Probe Spacing of 9mm

Because a dual-probe with a probe spacing of 12mm probe had been successfully designed, in order to further reduce the probe spacing, a 2D model with a probe spacing of 9mm was tested. Aerated concrete type B was tested with the 2D model. The details of construction the 2D model are given in Table 5.2. The element lengths and the corresponding locations for construction of the 2D model are shown in Figure 5.25.

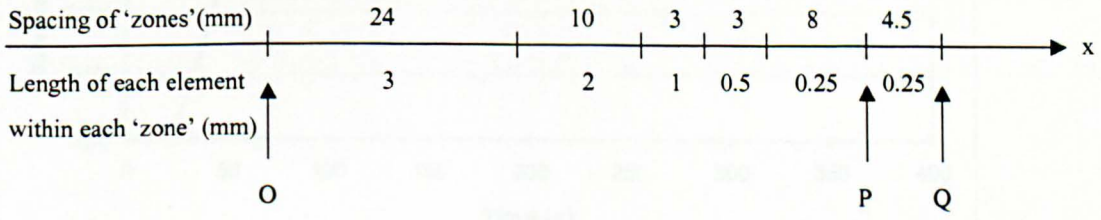

Figure 5.25 The element length and the corresponding location of the probe spacing of a 9mm model in x-direction

The temperature changes at the heating needle and the temperature sensor needle of the 2D model are shown in Figures 5.26 and 5.27. It can be seen that:

- The maximum temperature rise predicted by this 2D model was 1.08°C which was 0.14°C lower than that of the analytical solution. Thus, the probe spacing was not designed successfully.

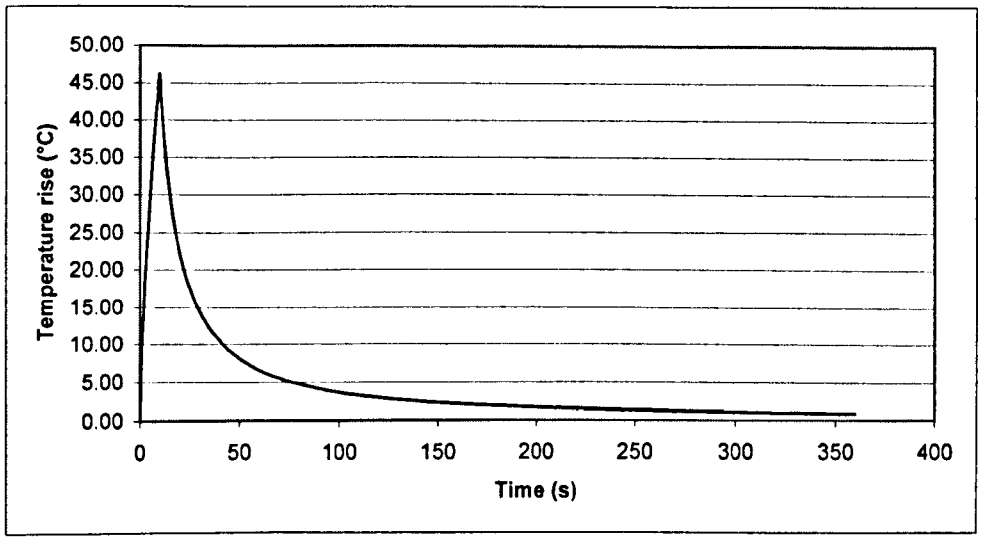

Figure 5.26 Temperature history plot at the position of the heating needle for the models with a spacing of 9mm

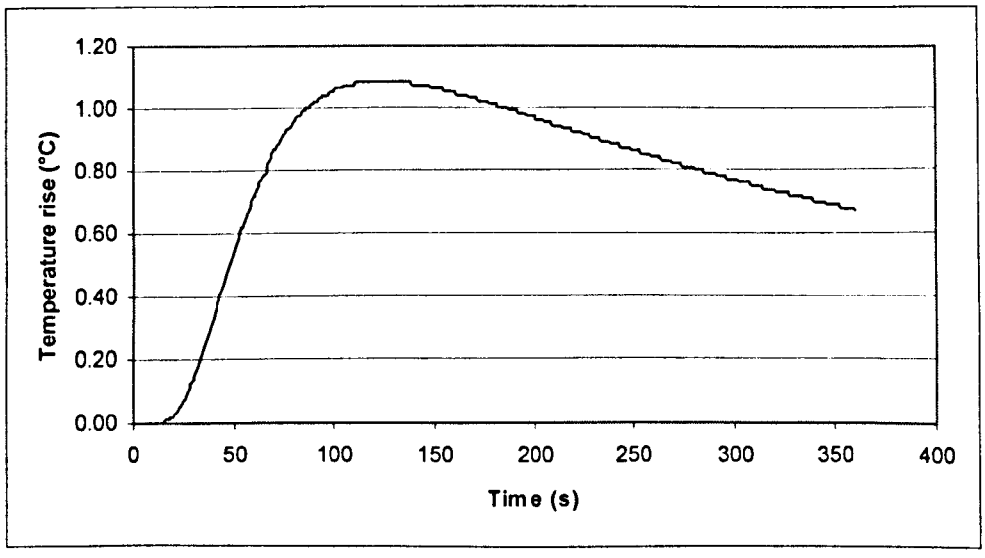

Figure 5.27 Temperature history plot at the position of the temperature sensor needle for the models with a probe spacing of 9mm

5.7 Summary of the Optimization of the Dual-probe Design

The simulation results with the 2D and 3D models are presented in Table 5.3. Firstly, the dual-probe was designed with a probe spacing of 20mm and heating needle length of 60mm. Secondly, the dual-probes were designed with a probe spacing of 18mm and heating needle lengths of 60mm and 50mm, respectively. Thirdly, the dual-probes were designed with a probe spacing of 16mm and heating needle lengths of 60mm and 50mm, respectively. Fourthly, the dual-probes were designed with a probe spacing of 14mm and heating needle lengths of 60mm, 50mm and 45mm, respectively. Fifthly, the dual-probes were designed with a probe spacing of 12mm and heating needle lengths of 50mm and 45mm, respectively. Finally, the dual-probe designed with a probe spacing of 9mm was unsuccessful because the maximum temperature rise predicted by this 2D model was 0.14°C lower than that of the analytical solution.

For the 3D model with a probe spacing of 12mm, the temperature sensor needle length was simulated as one third of the heating needle length. However, the optimal length of the temperature sensor needle was half that of the heating needle.

The work on the optimization of the dual-probe design has successfully demonstrated that, depending upon the building fabric material used, optimal probe lengths and spacings range from approximately 45 to 60mm and 12 to 20mm respectively.

The model with a probe spacing of 12mm and a heating needle length of 50mm was selected to construct the actual dual-probe. This is because the probe spacing is narrower

so that less energy input is needed, yet sufficiently large that the effect of the metal is negligible.

Table 5.3 Summary results of optimization of dual-probe design

Material	Probe spacing (mm)	Heating needle length (mm)	Energy input (J/m)	Model parameters		Numerical results	Analytical results
				Model	Time step (s)	ΔT_m (K)	ΔT_m (K)
Aerated concrete type B	9	-	549	2D	0.01	1.08	1.22
Aerated concrete type B	12	-	976	2D	0.01	*1.13*	
		45		3D	0.01	*1.11*	
		50		3D	0.01	*1.12*	
		50		3D*	0.01	*1.10*	
Aerated concrete type B	14	-	1329	2D	0.01	*1.16*	
		45		3D	0.01	*1.12*	
		50		3D	0.01	*1.13*	
		60		3D	0.01	*1.14*	
Aerated concrete type A	14	-	857	2D	0.01	*1.12*	
Aerated concrete type A	16	-	1120	2D	0.01	*1.14*	
		50		3D	0.01	*1.10*	
		60		3D	0.01	*1.12*	
Aerated concrete type B	16	50	1735	3D	0.01	*1.13*	
		60		3D	0.01	*1.15*	
Aerated concrete type A	18	-	1417	2D	0.01	*1.15*	
		50		3D	0.01	*1.10*	
		60		3D	0.01	*1.13*	
Aerated concrete type A	20	-	1750	2D	0.01	*1.16*	
		40		3D	0.01	1.03	
		60		3D	0.01	*1.12*	

Note:
1. * Temperature sensor needle length was modelled as 15mm.
2. Numerical results printed in *italic* indicate the successful probe design.

Chapter 6

Sample Preparation

6.1 Introduction

To experimentally verify the FE modelling, aerated concrete type B (CELCON, 2003) was selected as the test material. For simplicity, relating to the experimental work, aerated concrete type B will henceforth be referred to 'aerated concrete'. As noted previously (Section 5.1), the reasons for the selection of aerated concrete as the test material were that it is challenging thermally, i.e., the thermal properties of the aerated concrete and stainless steel are very different, and it is relatively easy to drill holes for installation the dual-probe. This chapter deals with the preparation of the sample (dry samples and conditioned samples) for testing with the dual-probe. Firstly, the methods of cutting the samples into suitable sizes and drilling the relevant holes are explained. Secondly, the procedures for drying the sample are detailed. Finally, the method and equipment for conditioning the sample are described.

6.2 Preparation of the Aerated Concrete Samples

Standard type aerated concrete blocks manufactured by H+H CELCON Limited, Kent, UK, were selected as the experimental test material. The dimensions of these aerated concrete blocks were 440mm×210mm×100mm. These blocks are much bigger than the sample size initially determined by the FE modelling work and have to be cut to suitable sizes (see below for detailed description of sample size determination). From the FE

modelling point of view, it is not problematic to use large samples. However, in practice, it would take a longer time to condition these large samples.

From the FE model which was used to simulate the heat transfer of a 12mm spacing dual-probe inserted into the sample, a suitable sample size was initially determined as 110mm×100mm×100mm. This was the 'ideal' size of the sample because the sample was just big enough so that there was no temperature changes at the edge of the sample when an energy pulse was applied to the dual-probe heater. To comply with the FE model and to consider the accuracy of sample cutting, the length of the sample was cut to 12mm longer than that in the FE model to ensure the holes were located 49mm away from the edge of the sample so that the sample's boundary was at the correct distance. The dimensions of the aerated concrete blocks were another factor considered for determining the width of the sample. The width of the sample was cut to 5mm wider than that required in the FE model. This is half the width of one aerated concrete block. In this way, more samples could be cut from one aerated concrete block. The depth of the sample was the same as the depth of one aerated concrete block. Thus, the sample size was determined to be 122mm×105mm×100mm in the concrete experiments. The samples were cut with a band saw, to ensure that they were cut accurately.

The spacing of the dual-probe 'needles' is an important factor affecting the measurement accuracy of moisture content. Therefore, the holes in the aerated concrete samples had to be drilled accurately in the experiment. The dual-probe was designed with a probe spacing of 12mm, heating needle length of 50mm, temperature sensor needle length of 25mm and outer diameter of 1.1mm. Therefore, the holes drilled in the aerated concreted samples had to comply with this arrangement. A long series high-speed stainless steel drill bit (product number A1511) was sourced from Drill Service Ltd., Surrey, UK, and was used to drill the holes. To ensure that the holes were drilled as required, a drilling jig was attached to the

surface of the sample. The drilling jig was made of a 10mm mild steel gauge plate. A milling machine was used to drill the holes to the required spacing of 12mm in the drilling jig. Due to the sample size being relatively small, clamps could not be applied to the jig for attaching it to the sample. The drilling jig was thus securely taped to the sample, as shown in Figure 6.1. The bench drill was set to a high speed to ensure the holes were drilled straight. Because aerated concrete is a 'soft' material, a 1mm drill was used to drill 1.1mm holes. This ensured that the dual-probe fitted the holes properly.

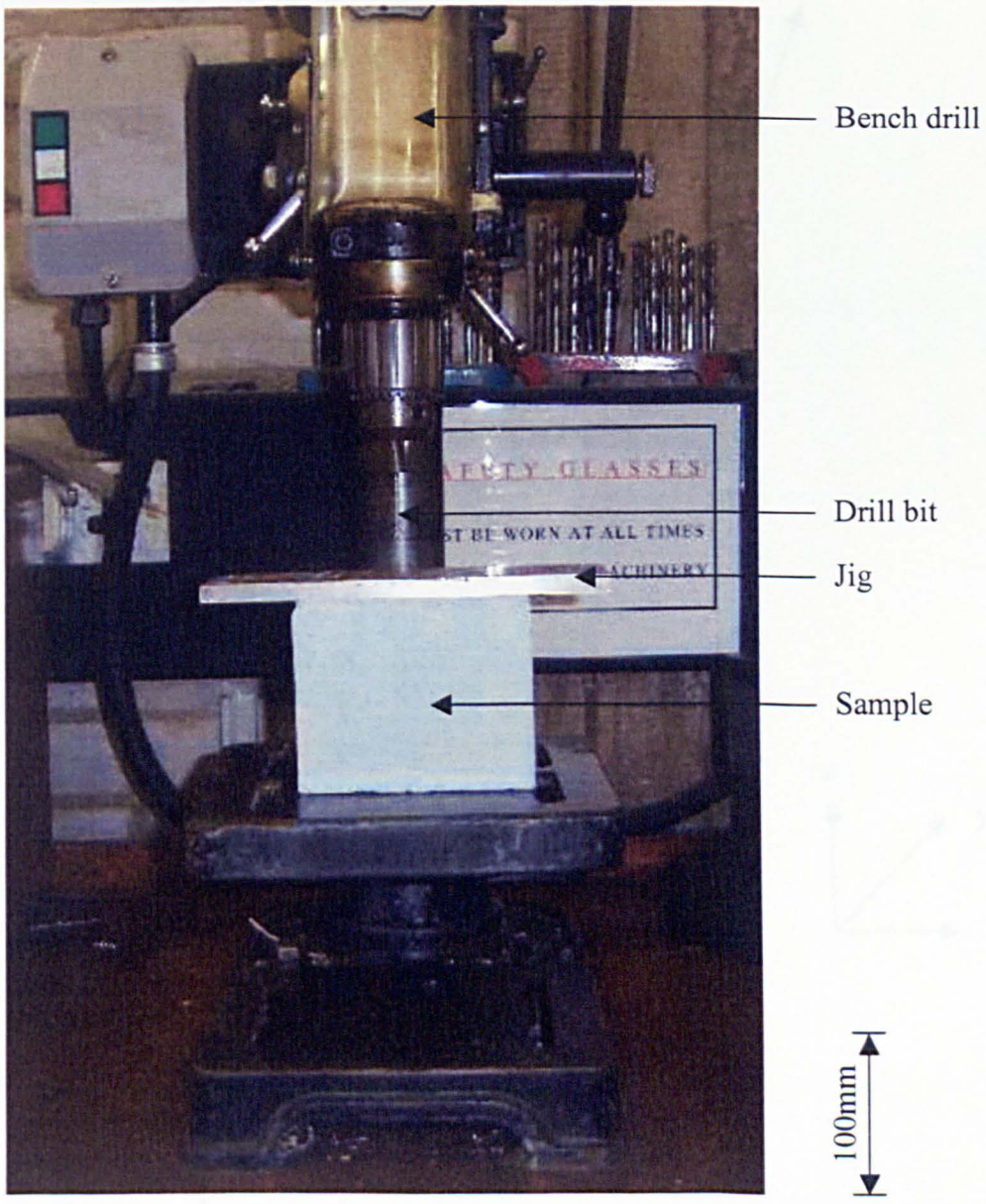

Figure 6.1 Drilling jig attached to the sample to drill holes using the bench drill

Ideally, the two holes in the aerated concrete sample should be drilled parallel and straight. However, in practice it was difficult to ensure this. Figure 6.2 shows the drilling problem three-dimensionally. When drilling further into the material, the margin of error becomes larger, as shown by the dotted tubes representing a possible error in probe spacing.

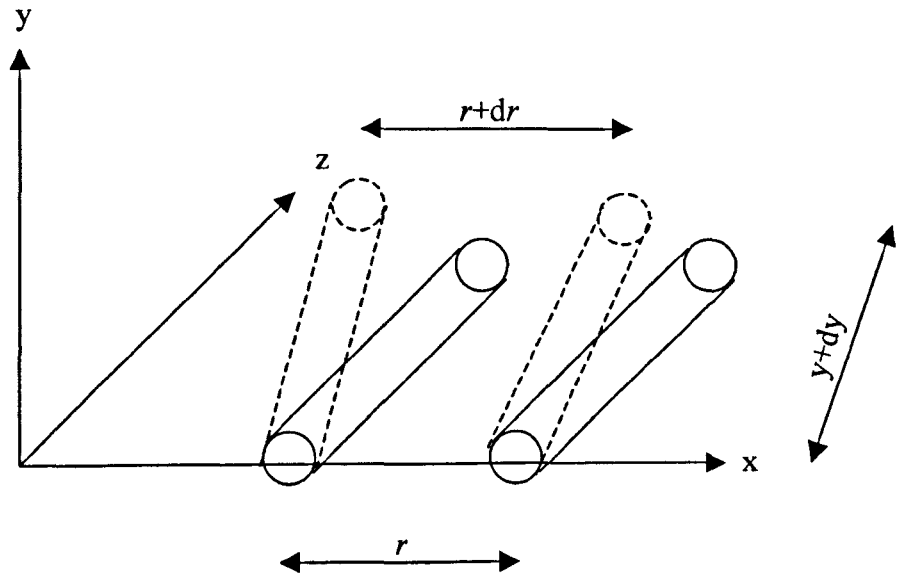

Figure 6.2 A schematic diagram of the actual drilling problem

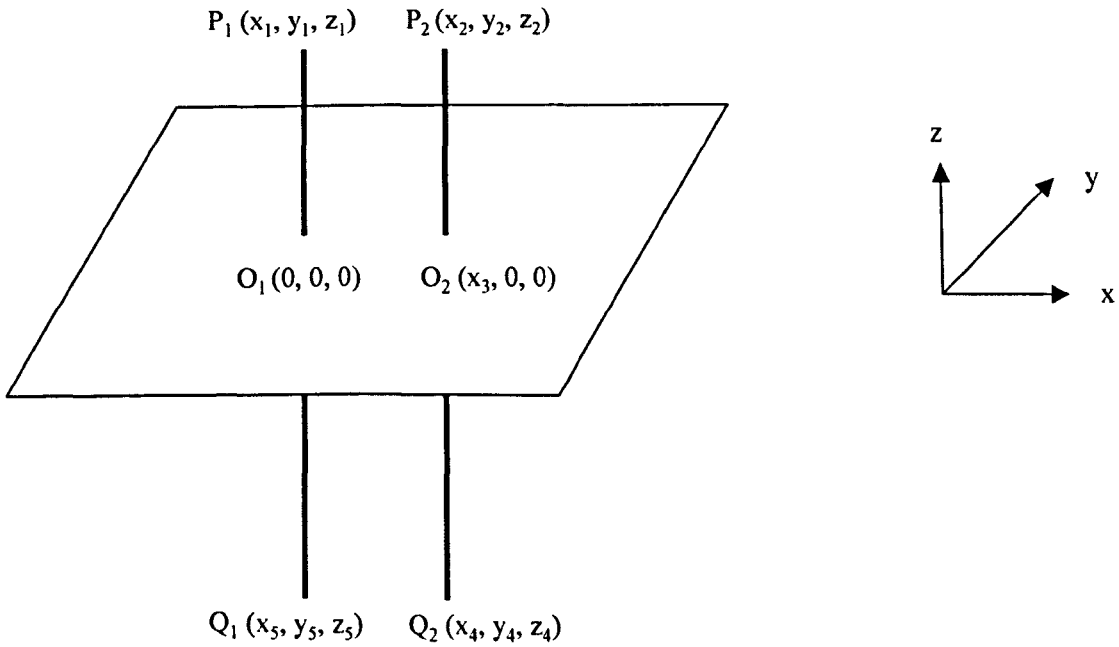

Figure 6.3 Estimation of probe spacing within a sample

The spacing of the two needles within the sample is estimated via Figure 6.3. The position of the needle within the sample can be deduced from the needle position above the sample. Two needles above the surface of the sample can be measured as P_1 (x_1, y_1, z_1) and P_2 (x_2, y_2, z_2) as shown in Figure 6.3. The two needles intersecting the surface of the sample are defined as O_1 (0, 0, 0) and O_2 (x_3, 0, 0). The tip points of the two needles below the surface of the sample are defined as Q_1 (x_5, y_5, z_5) and Q_2 (x_4, y_4, z_4). The values of z_4 and z_5 can be obtained according to the length of the needles and the values of z_1 and z_2. As the needle is free in the sample, two points can define a line. The lines that pass through points P_1 and O_1 can be written as:

$$z : y : x = z_1 : y_1 : x_1 \tag{6.1}$$

x, y and z in Equation (6.1) represent the P_1O_1 line. Equation (6.1) is equivalent to:

$$\begin{aligned} z : y &= z_1 : y_1 \\ z : x &= z_1 : x_1 \end{aligned} \tag{6.2}$$

Substitute the value z_5 to Equation (6.2), and x_5 and y_5 can be obtained. Thus, the location of Q_1 is identified. The lines passing through points P_2 and O_2 can be written as:

$$z : y : (x - x_3) = z_2 : y_2 : (x_2 - x_3) \tag{6.3}$$

x, y and z in Equation (6.3) represent the P_2O_2 line. Equation (6.3) is equivalent to:

$$\begin{aligned} z : y &= z_2 : y_2 \\ z : (x - x_3) &= z_2 : (x_2 - x_3) \end{aligned} \tag{6.4}$$

Substitute the values z_4 to Equation (6.4), and x_4 and y_4 can be obtained. Thus, the location of Q_2 is identified. The distance between points Q_1 and Q_2 is:

$$Q_1Q_2 = \sqrt{(x_4 - x_5)^2 + (y_4 - y_5)^2 + (z_4 - z_5)^2} \tag{6.5}$$

In the experiment, z_4 and z_5 are equal to 25mm, Equation (6.5) then becomes:

$$Q_1Q_2 = \sqrt{(x_4 - x_5)^2 + (y_4 - y_5)^2} \tag{6.6}$$

Thus, the central spacing of the two holes inside the sample is calculated.

To check the drilling of the holes, two stainless steel needles, which were used to make the dual-probe, were inserted into the two holes. A calliper was used to measure the spacing of the two holes on the surface of the aerated concrete sample. The tip spacing between the two stainless steel needles above the sample was also measured with the calliper. From these two spacings above the sample, it could be known whether these two holes were drilled in parallel. The two needles were examined with an engineering set square to measure if they were perpendicular to the surface of the aerated concrete sample. Therefore, it could be known whether the holes were drilled straight. In this way, the actual probe spacing within the sample could be estimated. However, as the holes were not perfectly drilled; the needle inside the sample may have been bent. In order to determine the probe spacing accurately, the aerated concrete samples were cut open after the dual-probe test had been performed to measure the real probe spacing and thus test the validity of the drilling procedure.

6.3 Drying of the Aerated Concrete Samples

After the aerated concrete blocks were cut to the required size and the holes had been drilled, the samples were dried in a ventilated oven. The aim of this drying was to enable the measurement of moisture content gravimetrically in order to allow comparison with the dual-probe method. This was done by measuring the mass of the fully dried sample and the conditioned sample. For compliance to prEN ISO 12570: ('*Hygrothermal performance of building materials – Determination of moisture by drying at elevated temperature*'), the oven temperature was set at 105°C to dry the aerated concrete samples. The oven temperature was controlled via a Proportional Integral and Derivative (PID) controller. In order to maintain a constant oven temperature, the oven controller had to be tuned before the oven was used. Otherwise, the temperature of the oven could not be controlled. The controller tuning process is described in more detail in Appendix B. The oven's temperature was tuned to 105.00±1.86°C which is within the prEN ISO 12570 requirement of temperature variation of ±2°C.

An aluminium dish was used as a container to hold the sample. The reason for selecting the aluminium dish was that it did not absorb moisture, and could tolerate temperatures over 105°C. An electronic scale with an accuracy of ±0.01g was used to measure the sample mass. The procedures of the mass measurement were:

1. Warm up the scale at least half an hour before taking the measurement.
2. Measure the mass of the container at the beginning of the experiment.
3. Measure the mass of the container and the sample over a 24 hours period until constant mass is reached, i.e., the change of mass between three consecutive weighing made 24 hours apart is less than 0.1% of the total mass.

4. The dry mass of the sample is obtained from subtracting the mass of the container from the total mass.

A total of nine aerated concrete samples were dried in the oven. After the samples had fully dried, the mass of the dry sample was calculated using Equation (6.7).

$$m_0 = m_2 - m_1 \tag{6.7}$$

where m_0 = mass of the dry sample (kg)

m_1 = mass of the container after drying (kg)

m_2 = mass of the sample and container after drying (kg)

The samples were dried in the oven until constant mass was reached. Table 6.1 shows an example of a record of a sample daily moisture loss. Figure 6.4 shows the trend of sample moisture loss. It took almost two weeks to fully dry the samples.

Table 6.1 Results of drying sample

Date	Day	Weight		
		Dish (g)	Sample and dish (g)	Sample (g)
23/06/2004	1	5.59	805.27	799.68
24/06/2004	2	5.59	776.71	771.12
28/06/2004	6	5.59	774.90	769.31
30/06/2004	8	5.59	774.93	769.34
1/07/2004	9	5.59	774.46	768.87
2/07/2004	10	5.59	774.47	768.88
5/07/2004	13	5.59	773.88	768.29
6/07/2004	14	5.59	773.93	768.34
7/07/2004	15	5.59	773.91	768.32

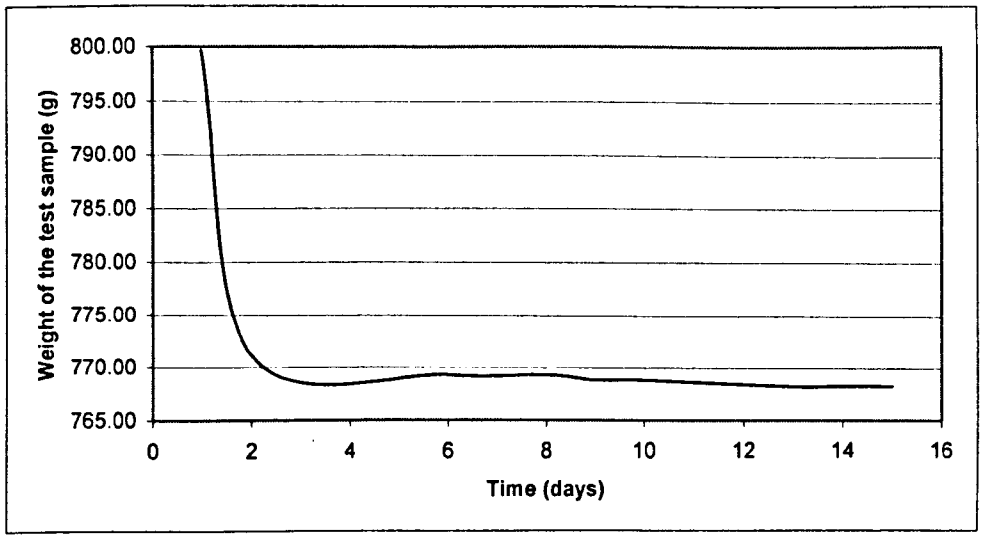

Figure 6.4 Sample mass change with time

Measuring the size of each sample and knowing the dry sample mass, the dry density of the sample can be calculated using Equation (6.8).

$$\rho_0 = \frac{m_0}{V_0} \tag{6.8}$$

where $V_0 = w \times l \times h$, the volume of the material (m^3)

w, l, h are the sides of the cuboid (m)

The dry mass of the samples, as well as the density is shown in Table 6.2. The dry density was used for calculating the moisture content after the dual-probe measurement (Section 8.8).

Table 6.2 Mass volume and density of dry samples

Sample No.	Dry mass (g)	Volume cm^3	Dry density kg/m^3
1	770.66	1329	580
2	816.22	1315	621
3	797.53	1288	619
4	781.32	1303	600
5	768.32	1307	588
6	779.06	1296	601
7	787.78	1308	602
8	778.60	1289	604
9	803.54	1292	622

6.4 Conditioning of the Aerated Concrete Samples

The aim of conditioning the sample was to ensure that the sample contained a uniformly distributed, known amount of moisture. The principle of conditioning a sample is to leave the sample in an atmosphere of known relative humidity (RH), which can be realised by an airtight container, containing a saturated salt solution at constant temperature. A stand should be used inside the container to ensure that the conditioned sample does not touch the salt solution.

The conditioning device used in the experiment thus consisted of an airtight container, a meshed stainless steel plate seated on a stand, and aluminium dishes. The sample material was exposed to a controlled atmosphere in the container. Two kinds of airtight containers were used in the experiment. Firstly, two glass desiccators shown in Figure 6.5 were used to condition four samples. However, it was found to be difficult to install the thermocouples and electric wires inside the desiccator because there was no hole available through the desiccator. To solve the problem of installation of the thermocouples and electric wires, two perspex boxes were constructed with sealable holes on either their bodies or lids.

Figure 6.5 Glass desiccator used for conditioning sample

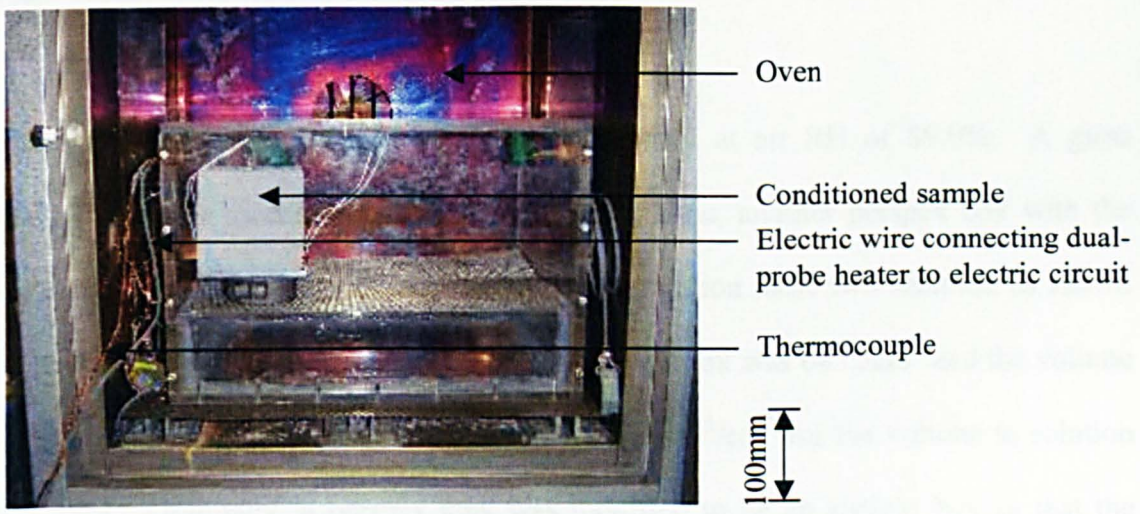

Figure 6.6 Perspex box used for conditioning sample

One airtight container was made of 8mm thickness perspex board and is shown in Figure 6.6. Two holes with a diameter of 15mm were drilled in two sides of the perspex box respectively. The dimensions of this perspex box were 416mm×316mm×266mm. According to the ASTM E104-85 (1990): ('*Standard practice for maintaining constant relative humidity by means of aqueous solutions*'), the ratio of the volume of the perspex box to its solution surface area is required not to be larger than $25cm^3/cm^2$. The solution

surface area of the airtight container was 1200cm^2 and the volume was 30000cm^3. This led to a proportion of 25cm^3/cm^2 for the volume to solution surface area. The perspex box could be tightly sealed against water vapour by means of a gasket and screws in the lid. These holes in the perspex box body were used to install thermocouples and electric wires, which connected the sample and electronic device. To solve the problem of sealing the thermocouple and electric wire in the gap of the hole, rubber bungs with a pre-cut slot were inserted into the four holes. The thermocouple and electric wire was installed to the perspex box through the pre-cut slots. Silicon rubber was used to seal the gaps around the rubber bung, hole, thermocouple and electrical wire. The perspex box was used to condition four samples at air RH of 96.4%. After the moisture content measurement of the four samples, then, the perspex box was used to condition three samples at air RH of 89.0%.

Another two samples were required to be conditioned at air RH of 89.0%. A glass desiccator was first used as the airtight container. Then, another perspex box with the dimensions 330mm×195mm×215mm was used to condition these two samples, as shown in Figure 6.7. The solution surface area of the perspex box was 643.5cm^2 and the volume was 13835.3cm^3, this then being a proportion of 21.5cm^3/cm^2 for the volume to solution surface area. Originally, a perspex tank was modified to be an airtight box so that the perspex box could be tightly sealed against water vapour by means of a gasket and screws in the lid (6mm perspex). Four holes with a diameter of 12mm were made in the lid for installation of the thermocouples and electric wires. A cable gland was installed in each hole to hold either the thermocouple or the electric wire. The cable gland (product number 444-0045) was sourced from RS, London, UK. All the airtight containers used for conditioning samples are listed in Table 6.3.

Table 6.3 Airtight containers used for conditioning samples

Date	Desiccator 1		Desiccator 2		Desiccator 3		Perspex box 1*							Perspex box 2**	
31/03/2004	Sample1	Sample 2													
2/04/2004			Sample 3												
6/04/2004				Sample 4											
18/05/2004							Sample 1	Sample 2	Sample 3	Sample 4					
9/07/2004					Sample 5										
13/07/2004						Sample 6									
19/08/2004														Sample 5	Sample 6
15/09/2004														***	
11/10/2004							***								***
14/10/2004									***						
27/10/2004								***							
3/11/2004										***					
23/11/2004											Sample 7	Sample 8	Sample 9		
19/01/2005											***				
20/01/2005												***			
25/01/2005													***		

Note:

1. * Samples 1, 2, 3 and 4 moved from desiccators 1 and 2 to perspex box 1 on 18th May 2004.
2. ** Samples moved for desiccator 3 to perspex box 2 on 19th August 2004.
3. *** This sample was tested with dual-probe.

Figure 6.7 Airtight container made of perspex tank used for conditioning sample

The meshed stainless steel plate had a sufficient open area so that the air could circulate well. Because the salt solution is corrosive, a suitable material was selected for the plate and dishes. The dish was designed to be 6mm high with three slots (3mm in depth) so that the air could access the sample from the bottom. The dish is shown in Figure 6.8.

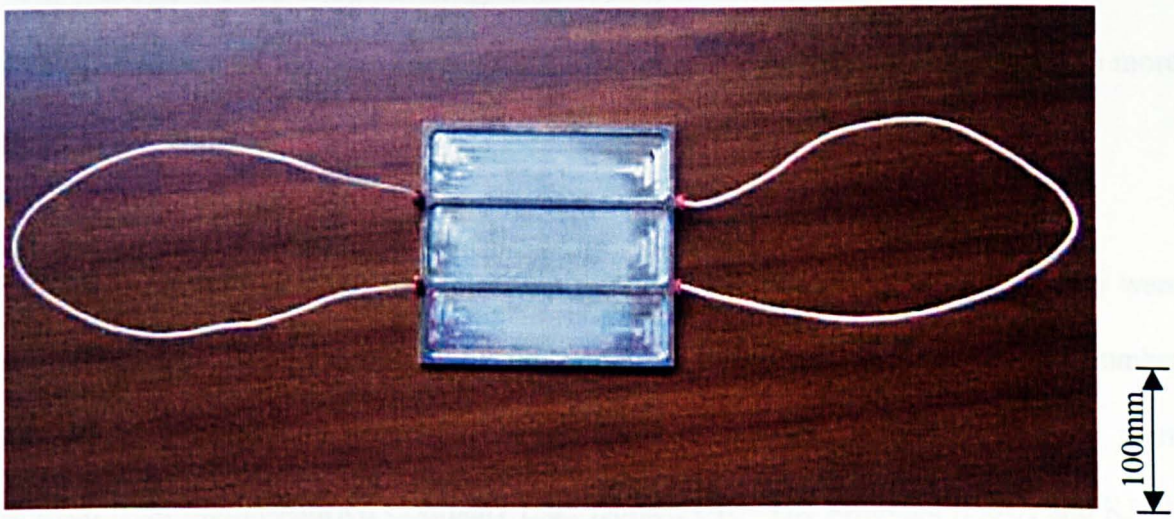

Figure 6.8 Dish used to hold the sample

For compliance with prEN ISO 12571: ('*Hygrothermal performance of building materials - Determination of hygroscopic sorption properties*'), an oven with a temperature variation of ±0.33°C at 40°C was used as a constant-temperature chamber to condition the sample. The original controller of the oven was a Proportional Integral (PI) controller, which could not control temperature accurately enough for this experiment. A EUROTHERM 2132

PID temperature controller (product number 208-2739) was thus sourced from RS, London, UK, and used to replace the original PI temperature controller. In the meantime, a 100 ohm platinum resistance temperature sensor (product number 362-9812) was sourced from RS, London, UK, and installed in the oven as the set point for the feedback control loop. The PID temperature controller was connected to the 100 ohm platinum resistance temperature sensor and a solid state relay. The solid state relay (product number 346-895) was sourced from RS, London, UK, and was used to switch on the power to the heater. At least 5°C temperature difference between the oven and room was needed so that the oven temperature could be well controlled. The oven temperature was chosen as close to room temperature as possible. In summer, the ambient temperature is lower than 35°C. Oven temperature was first set at 35°C. The controller of the oven could not be tuned. Then, the oven temperature was set to 40°C. The controller could then be tuned successfully because 40°C was above room temperature by at least 5°C, even in the hot of summer. Therefore, 40°C was chosen as the oven temperature. The oven tuning process is described in more detail in Appendix B.

Potassium sulphate (K_2SO_4) and potassium nitrate (KNO_3) of analytical grade purity were selected as the salts for conditioning the samples. Potassium sulphate (product number ALDRICH-221295) and potassium nitrate (product number ALDRICH-221325) were sourced from Sigma-Aldrich Company Ltd., Dorset, UK. The saturated K_2SO_4 and KNO_3 solutions at 40°C provided air RH of 96.4% and 89.0% respectively. The solubility of these two salts is listed in Table 6.4. The salt solutions were prepared in the following way (prEN ISO 1271; Jowitt *et al.*, 1989):

1. Weigh a certain amount of salt and pour into the airtight container.
2. Add room temperature distilled water while stirring until solids salt up to a level of about 1mm below the surface of the liquid.

3. Close the airtight container. Check and stir solutions regularly to ensure that they retain a mixture of solid and liquid and have not become contaminated.

Table 6.4 Solubility of KNO_3 and K_2SO_4 at 40°C

Substance	Solubility
	g per 100ml of distilled water
KNO_3	38.6
K_2SO_4	19.9

The quantities of salts and water used to prepare the saturated salt solutions are shown in Table 6.5.

Table 6.5 The amount of water and salts in (g) used for conditioning samples

Date	Desiccator 1		Desiccator 2		Perspex box 1*		Desiccator 3		Perspex box 2**		Perspex box 1***	
	K_2SO_4	Water	K_2SO_4	Water	K_2SO_4	Water	KNO_3	Water	KNO_3	Water	KNO_3	Water
31/03/2004	250.00	85.61										
2/04/2004			256.42	90.37								
5/04/2004		111.80		76.72								
6/04/2004		75.44		77.53								
26/04/2004		88.78		109.8								
18/05/2004					500.09	371.03						
1/06/2004						149.78						
4/06/2004					550.91	339.44						
6/07/2004						122.57						
9/07/2004							278.84	281.76				
2/08/2004						209.77						
19/08/2004									222.20	328.43		
13/09/2004						192.95						
23/11/2004											1297.70	854.45

Note:

1. * Samples moved from desiccators 1 and 2 to perspex box 1 on 18th May 2004.
2. ** Samples moved from desiccator 3 to perspex box 2 on 19th August 2004.
3. *** Perspex box 1 was used to condition 3 samples with KNO_3 after it was used to condition sample with K_2SO_4.

Whilst the aerated concrete samples were being conditioned, their moisture contents were checked regularly. Moisture content can be defined as moisture content mass by volume, moisture content mass by mass, and moisture content volume by volume. Moisture content mass by mass was used in this study and was calculated via Equation (6.9).

$$\theta_m = \frac{m - m_0}{m_0} \tag{6.9}$$

where θ_m = moisture content mass by mass (kg/kg)

m = mass of the sample before drying (kg/kg)

The procedures for determining the moisture content of the sample were as follows:

1. Prepare the saturated salt solution for the required RH in the airtight box.
2. Weigh the aluminium dish when it is empty and dry (m_1). Weigh the aluminium dish and fully dried test sample (m_3).
3. Put the sample and aluminium dish into the airtight container with the salt solution. Place the airtight container into the oven.
4. Periodically weigh the sample until it has reached constant mass. Open the oven and the lid of the airtight container, move the sample and aluminium dish onto the scale. After weighing the aluminium dish and conditioned sample (m_4), return the sample and aluminium dish to the airtight container. Close the airtight container and the oven.
5. Constant mass is reached if the change in mass between three consecutive weightings made at least 24 hours apart is less than 0.1% of the total mass of the sample.
6. Calculate the water mass within the sample (m-m_0) at equilibrium at the required relative humidity:

$$m - m_0 = m_4 - m_3 \tag{6.10}$$

7. Calculate the moisture content using Equation (6.9).

The time for conditioning aerated concrete samples such that they reach equilibrium depended on the sample and air RH. 70 days were needed to condition five aerated concrete samples with RH 89.0% saturated KNO_3 solutions to equilibrium. However, after 213 days the four aerated concrete samples conditioned with RH 96.4% saturated K_2SO_4 solutions had still not reached equilibrium. Tables 6.6 and 6.7 show examples of the rate that the aerated concrete samples absorbed moisture with air RH of 89.0% and 96.4%, respectively. The trends of samples absorbing moisture with air RH of 89.0% and 96.4% are shown in Figures 6.9 and 6.10. For the sample conditioned with air RH of 89.0%, it can be seen that the sample quickly absorbed moisture during the first few days. After 14 days, the sample absorbed less moisture daily until it reached equilibrium. For the sample conditioned with air RH of 96.4%, it can be seen that the sample quickly absorbed moisture during the first 10 days. Afterwards, the sample absorbed less moisture daily.

Table 6.6 Results of conditioning samples with RH of 89.0%

Date	Day	Weight		Absorbed moisture
		Gross weight* (g)	Net weight (g)	(g)
13/07/2004	1	801.64	781.10	-
19/07/2004	7	836.71	816.17	35.07
26/07/2004	14	841.63	821.09	4.92
2/08/2004	21	843.69	823.15	2.06
10/08/2004	29	844.43	823.89	0.74
16/08/2004	35	844.61	824.07	0.18
20/08/2004	39	844.81	824.27	0.20
23/08/2004	42	843.92	823.38	-0.89
27/08/2004	46	844.22	823.68	0.30
6/09/2004	56	844.78	824.24	0.56
10/09/2004	60	844.34	823.80	-0.44
13/09/2004	63	844.31	823.77	-0.03
17/09/2004	67	844.32	823.78	0.01
24/09/2004	74	844.84	824.30	0.52

Note:
1. * The weight of the dish and dual-probe is included.

Table 6.7 Results of conditioning samples with RH of 96.4%

Date	Day	Weight		Absorbed moisture
		Gross weight* (g)	Net weight (g)	(g)
6/04/2004	1	920.15	781.32	-
14/04/2004	9	957.99	819.16	37.84
16/04/2004	11	965.30	826.47	7.31
19/04/2004	14	964.53	825.70	-0.77
20/04/2004	15	967.88	829.05	3.35
23/04/2004	18	975.02	836.19	7.14
26/04/2004	21	978.96	840.13	3.94
28/04/2004	23	980.67	841.84	1.71
4/05/2004	29	989.92	851.09	9.25
7/05/2004	32	992.77	853.94	2.85
11/05/2004	36	996.38	857.55	3.61
18/05/2004	43	1001.47	862.64	5.09
19/05/2004	44	1002.32	863.49	0.85
21/05/2004	46	1005.31	866.48	2.99
24/05/2004	49	1009.79	870.96	4.48
28/05/2004	53	1011.60	872.77	1.81
1/06/2004	57	1016.79	877.96	5.19
4/06/2004	60	1019.80	880.97	3.01
7/06/2004	63	1023.14	884.31	3.34
11/06/2004	67	1026.04	887.21	2.90
14/06/2004	70	1028.34	889.51	2.30
18/06/2004	74	1031.76	892.93	3.42
21/06/2004	77	1034.17	895.34	2.41
28/06/2004	84	1038.85	900.02	4.68
6/07/2004	92	1043.42	904.59	4.57
13/07/2004	99	1048.74	909.91	5.32
19/07/2004	105	1052.61	913.78	3.87
26/07/2004	112	1054.58	915.75	1.97
2/08/2004	119	1058.34	919.51	3.76
10/08/2004	127	1060.12	921.29	1.78
16/08/2004	133	1061.50	922.67	1.38
23/08/2004	140	1065.77	926.94	4.27
27/08/2004	144	1066.27	927.44	0.50
6/09/2004	154	1070.44	931.61	4.17
13/09/2004	161	1071.48	932.65	1.04
20/09/2004	168	1072.40	933.57	0.92
27/09/2004	175	1078.91	940.08	6.51
5/10/2004	183	1083.98	945.15	5.07
8/10/2004	186	1084.19	945.36	0.21
13/10/2004	191	1083.28	944.45	-0.91
17/10/2004	195	1084.02	945.19	0.74
23/10/2004	201	1085.80	946.97	1.78
4/11/2004	213	1090.45	951.62	4.65

Note:

1. * The weight of the dish and dual-probe is included.

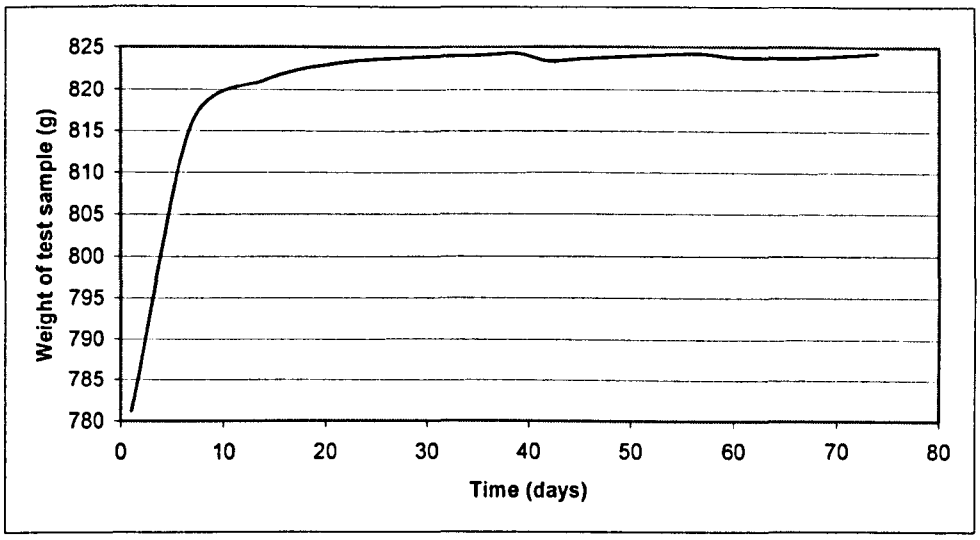

Figure 6.9 Sample conditioning process with RH of 89.0%

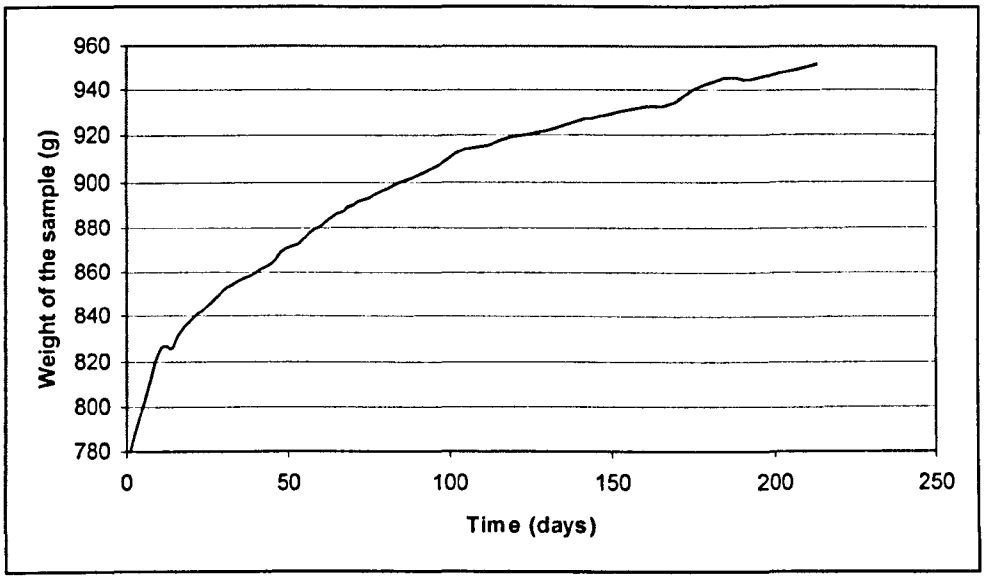

Figure 6.10 Sample conditioning process with RH of 96.4%

Chapter 7

Construction of the Dual-probe System

7.1 Introduction

Four dual-probes were constructed with a probe spacing of 12mm, heating needle length of 50mm and temperature sensor needle length of 25mm according to the results of the optimisation procedures detailed previously (Chapter 5). In this chapter, the construction of the dual-probe system will be detailed. Firstly, the methods of construction of the dual-probe needles, the dual-probe heater and the dual-probe holder are described. Secondly, the details of the method and equipment used for the construction of the dual-probe electrical control system are provided. Figure 7.1 shows the dual-probe as constructed.

7.2 Dual-probe

AISI 304/316 Hypodermic Stainless Steel Tubing (Gauge No. 19) was sourced from Coopers Needle Works Ltd., Birmingham, UK. The hypodermic tubing was used to create the needles for both the temperature sensor needle and the heating needle. The inner and outer diameters of this tubing were 0.685mm and 1.1mm respectively. The reason for choosing this tubing was based on the diameter of the thermocouple and the heater used for the dual-probe, as well as the FE modelling. The needles for making both the temperature sensor needle and the heating needle were cut to length using shears and a grinding wheel. The tubing was marked to the appropriate length first, then the shears were used to cut the

tubing to an approximate length slightly longer than the desired probe length. Finally, the grinding wheel was used to grind the tube to the desired length.

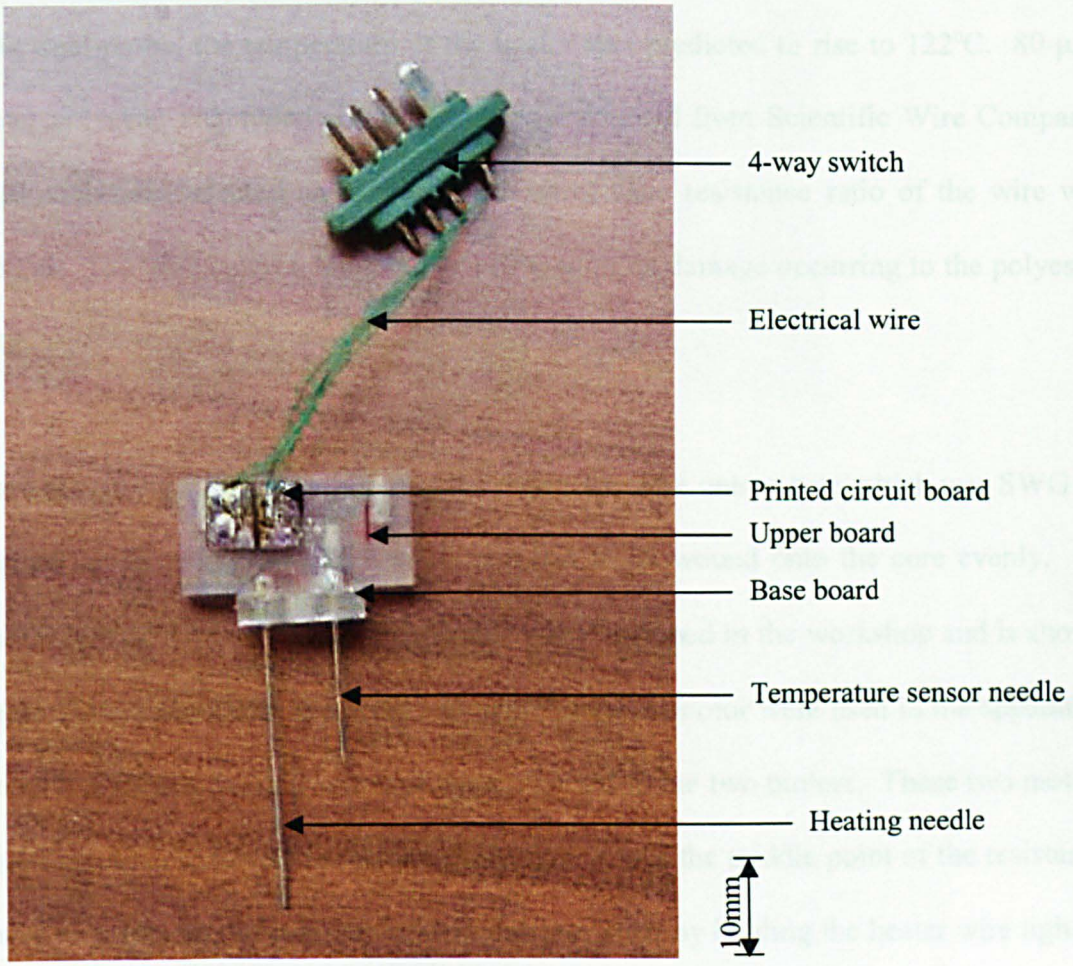

Figure 7.1 Completed dual-probe

The needles were cleaned before the thermocouple and heater were inserted into the needles. Burrs inside the needles may have formed during the cutting process. Dust was also found inside the needles. Firstly, a piece of copper wire with a diameter less than the inner diameter of the needle was dipped in detergent. Then, the copper wire was pushed in and pulled back several times inside the needles. Finally, the needles were washed with water. After the needles were fully dry, they were ready for manufacturing the temperature sensor needle and heating needle.

7.2.1 Heating Needle

The selection of the resistance wire used for making the heater was based on the limitation of the needles' inner diameter. Another factor was that with the FE model of a 12mm spacing dual-probe, the temperature of the heater was predicted to rise to 122°C. 80-μm-diameter polyester enamelled copper nickel wire sourced from Scientific Wire Company, London, UK, was selected as the resistance wire. The resistance ratio of the wire was 97.84Ω/m. The wire could tolerate up to 180°C without damage occurring to the polyester coating.

The heater was constructed by winding the resistance wire onto a core which was SWG 33 enamelled copper wire. The resistance wire had to be wound onto the core evenly. To achieve this goal, a heater winding apparatus was developed in the workshop and is shown in Figure 7.2. A clockwise motor and an anti-clockwise motor were used in the apparatus. The core was soldered onto two couplings connected to the two motors. These two motors ensured that the core turned in the same direction. Once the middle point of the resistance wire was wound onto the core, the heater could be made by holding the heater wire tightly, and turning on the heater winding apparatus.

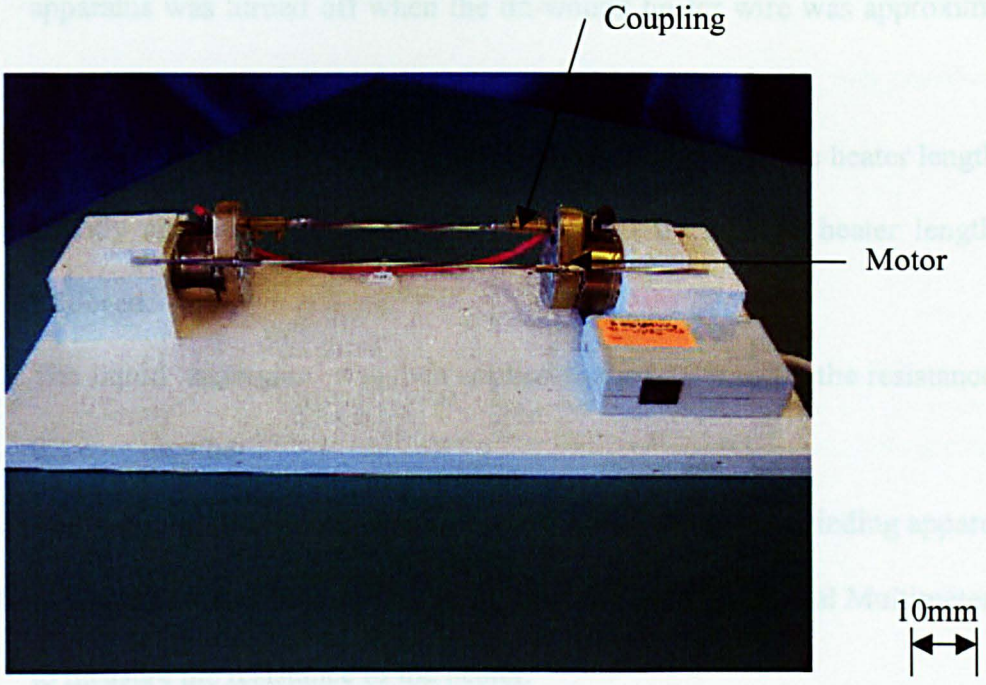

Figure 7.2 Heater winding apparatus

The procedures for making the heater were:

1. The heater resistance wire was measured to an appropriate length with a ruler. The accuracy of the ruler is ±0.5mm. The length of the heater resistance wire had to be measured accurately to within 0.5mm.
2. The core was measured to the appropriate length.
3. Sandpaper was used to peel off the coating of both ends of the core.
4. The core was tightly soldered onto the couplings which connected to the motors of the apparatus.
5. The resistance wire was folded in half. The middle point of the wire was connected to the core by twisting the resistance wire around it twice. Afterwards, liquid 'superglue' was used to glue the resistance wire's middle point and the core together. The liquid 'superglue' (product number 330-4030) was sourced from RS, London, UK. Finally, the liquid 'superglue' was allowed to fully dry.
6. The heater winding apparatus was then turned on while the resistance wires were held tightly by hand. The wire was moved evenly while the core was turned. The

apparatus was turned off when the un-wound heater wire was approximately 3cm long.

7. A calliper was used to measure the length of the heater. The heater length could be slightly adjusted by stretching it by hand if the desired heater length was not achieved.
8. The liquid 'superglue' was then applied to the heater to fix the resistance wire and the core together.
9. The two ends of the core were then cut off from the heater winding apparatus.
10. A Fluke 22 series II (accuracy of 0.3% of the reading) Digital Multimeter was used to measure the resistance of the heater.

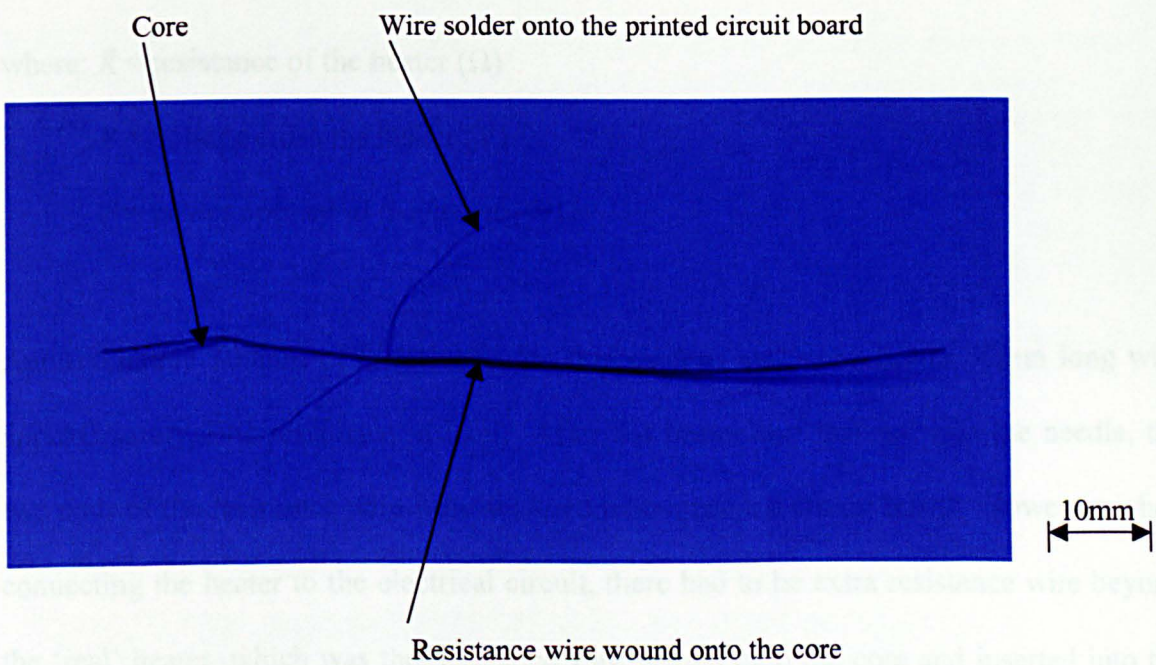

Figure 7.3 Dual-probe heater

Figure 7.3 shows a heater wire wound onto the core. To prevent an air gap occurring between the heater and inner surface of the needle, heat sink compound was applied to the heater before it was inserted into the needle. The heat sink compound (product number 554-331) was sourced from RS, London, UK. The Digital Multimeter was used to

measure the resistance of the heater after it was inserted into the needle. Comparing the resistance of the heater before and after insertion into the needle, it was possible to know whether the coating of the heater was damaged during the process of inserting the heater into the needle.

Based on the FE modelling work, with probe spacing from 12mm to 20mm, the power input to the heater varied from 4.8W to 10.4W to achieve a maximum temperature rise of approximately 1.12°C at the temperature sensor needle. The maximum voltage output of the power supply unit was 15.6V. The resistance of the heater could be calculated as:

$$R = \frac{V^2}{P} \tag{7.1}$$

where: R = resistance of the heater (Ω)

V = voltage cross the heater (V)

P = power applied to the heater (W)

Approximately 300mm of resistance wire was used to make one heater 50mm long with approximately 29Ω resistance in total. After the heater was inserted into the needle, the two ends of the resistance wire were soldered onto a printed circuit board. However, when connecting the heater to the electrical circuit, there had to be extra resistance wire beyond the 'real' heater, which was the resistance wire wound onto the core and inserted into the hole below the surface of the sample. This 'real' heater is referred as the resistance wire wound onto the core in this thesis. It was necessary to calculate the power of the heater which contributed the heat leading to the temperature rise at the temperature sensor needle. The power of the heater was calculated by total power input, multiplied by the ratio of the resistance wire length which formed the 'real' heater over the resistance wire length which formed the 'effective' heater, which was the total wire length minus the wire soldered onto

the printed circuit board. Further details of the heater power calculation is given in Section 8.2

7.2.2 Temperature Sensor Needle

Based on the temperature measurement range, a miniature 0.5mm diameter mineral insulated type T thermocouple with pot seal was used as the temperature sensor for the dual-probe. Four type T thermocouples (product number 406-491) were sourced from TC Direct Ltd., London, UK. As the diameter of the thermocouple was 0.5mm, it could be inserted into the needle easily. In order to make the temperature measurement as accurate as possible, any interference should be avoided. Therefore, a metal sheath was used to cover the lead of the thermocouple and was connected to ground as shown in Figure 7.4. Before the use of the thermocouples, they were calibrated against a quartz crystal thermometer Quat 100/200, (serial No.0015978, probe serial 08880087, ASAP Calibration Services Ltd, calibrated January 2004: certificate number No. N1115855T). The quartz crystal thermometer was sourced from Heraeus, Hanau, Germany. The thermocouple calibration is described in Appendix B.

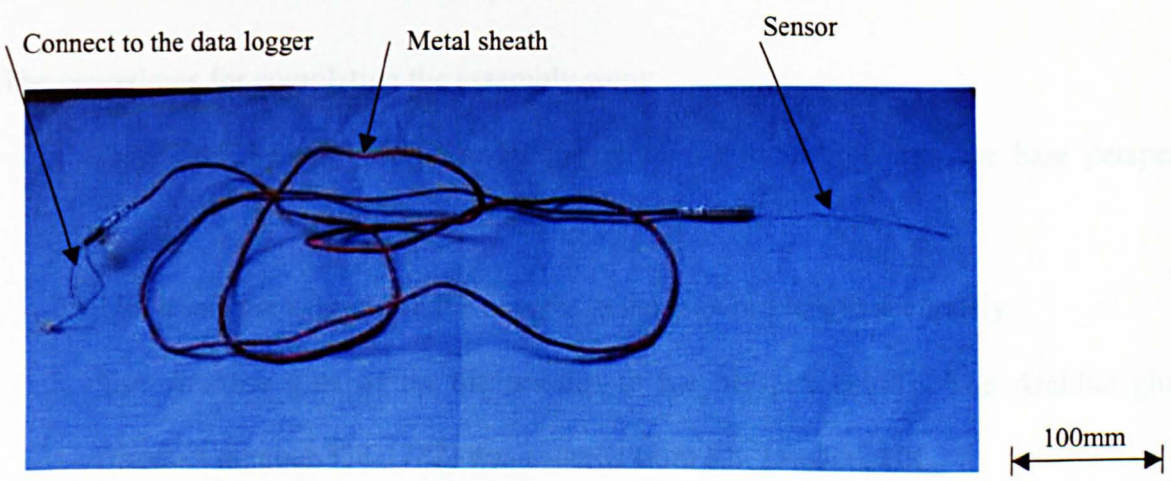

Figure 7.4 Thermocouple covered with a metal sheath

To prevent an air gap occurring between the thermocouple and the inner surface of the needle, heat sink compound (see Section 7.2.1) was applied to the thermocouple before it was inserted into the needles. The construction of temperature sensor needle was completed when the thermocouple was inserted into the needle.

The heating needle and thermocouple needle were mounted onto a perspex board. The completed dual-probe is shown in Figure 7.1.

Due to the low thermal conductivity of perspex, two pieces of 4mm thick perspex board were used to form one dual-probe holder. The dimensions of the two perspex boards were 25mm×10mm×4mm and 40mm×20mm×4mm respectively. A schematic diagram of the perspex board is shown in Figure 7.5. Two holes with a diameter of 1.1mm were drilled in one of the perspex boards (the base board). To prevent the heat from being transferred horizontally from the heating needle to the temperature sensor needle, a hole with diameter of 4mm was drilled between the two 1.1mm holes. Another piece of perspex board (the upper board) was used to hold a printed circuit board in place so that the resistance wire ends could be soldered onto it and connected to the electric circuit. The upper perspex board was fixed on top of the base perspex board by screws.

The procedures for completing the assembly were:

1. Install the heating needle and temperature sensor needle into the base perspex board.
2. Use a calliper to measure the needles to the required length accurately.
3. Use Araldite glue to fix the needles to the perspex board. The Araldite glue (product number 332-1782) was sourced from RS, London, UK.
4. Glue the printed circuit board onto the upper perspex board.
5. Solder the two ends of the resistance wire onto the printed circuit board.

6. Solder a 100mm long Kynar insulated 30 AWG wire onto a 4-way switch which connected to the electrical circuit of the dual-probe system. The Kynar insulated 30 AWG wire and the 4-way switch were sourced from RS, London, UK. Their product numbers were 209-4833 and 466-056 respectively.
7. Solder electrical wire onto the printed circuit board.

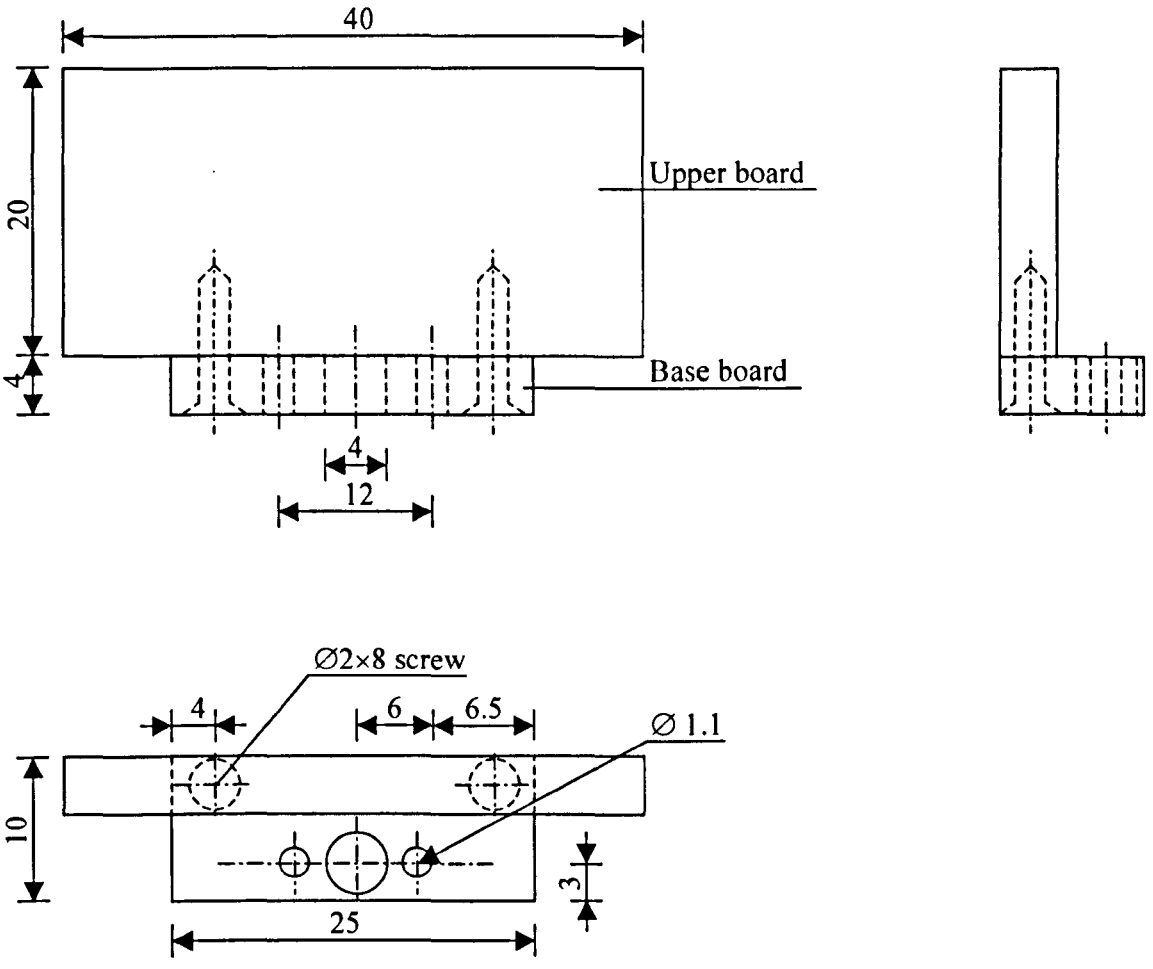

Figure 7.5 A diagram of the dual-probe holder (not to scale)

7.3 Electrical Control System

The electrical control system consisted of a power supply unit, a data logger, a computer, a dual-probe, a voltage divider and a 1Ω resistor. A schematic view of the dual-probe measurement system is shown in Figure 7.6.

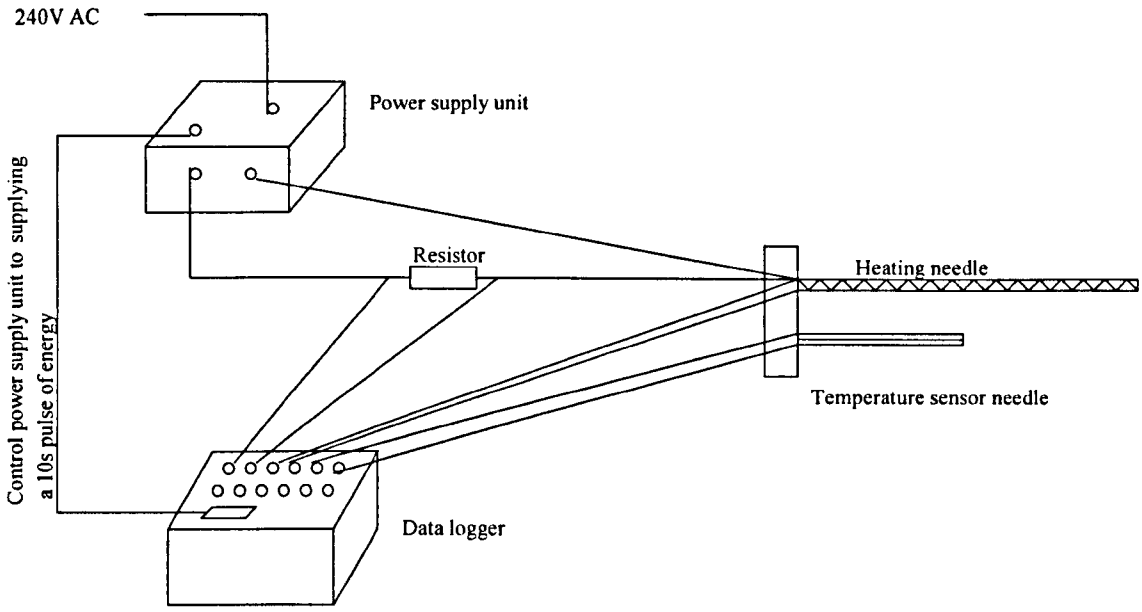

Figure 7.6 Schematic view of the dual-probe measurement system

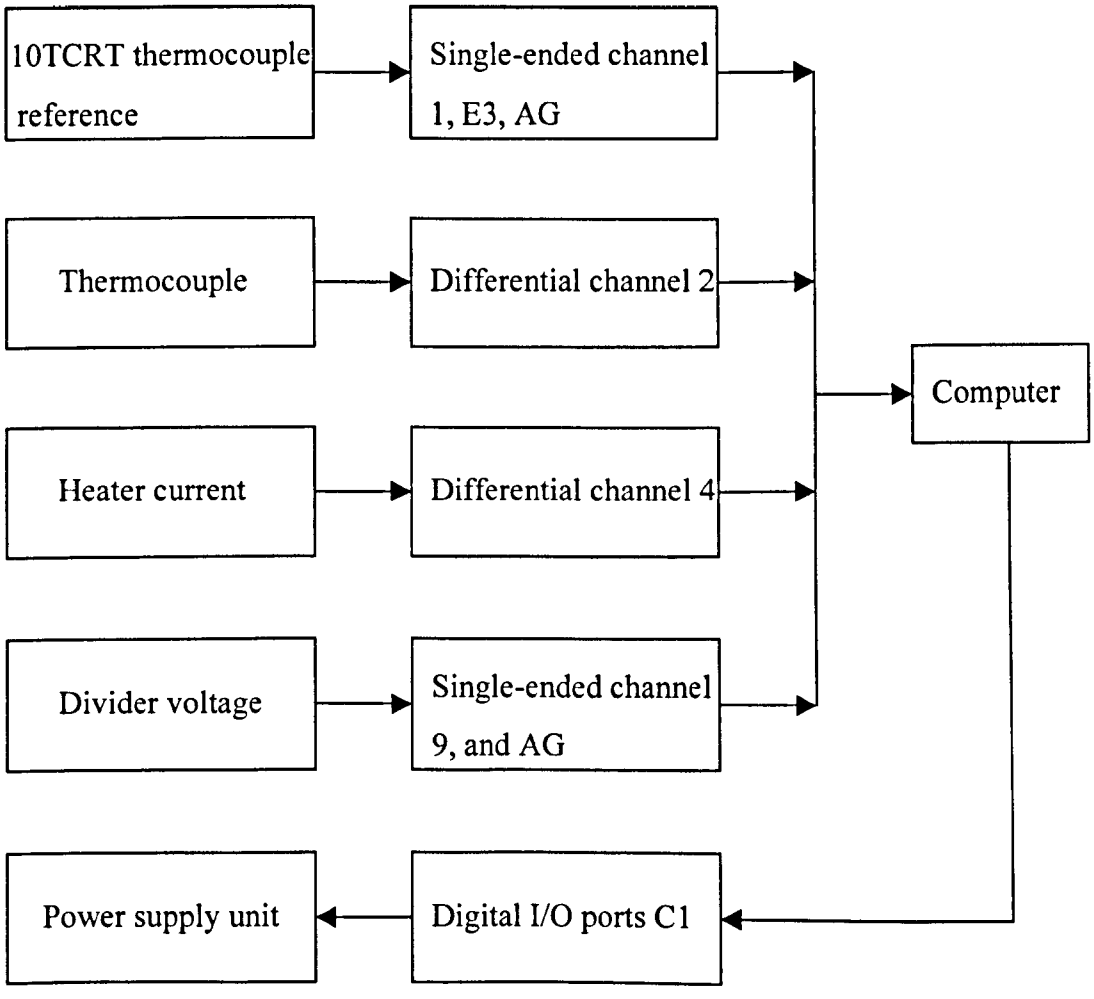

Figure 7.7 A schematic diagram for use of the data logger

7.3.1 Data Logger

A CR10X data logger (CR10X Measurement and Control Module Instruction Manual, 1997) was used in the dual-probe measurement system to control a 10s pulse power input to the heater, measure the voltage across the heater, monitor the current through the heater, and record the thermocouple temperature measurement. The CR10X data logger was sourced from Campbell Scientific Ltd., Leicestershire, UK. A schematic diagram of the use of the data logger is shown in Figure 7.7.

The CR10X data logger is a fully programmable data logger and controller in a small, rugged, sealed module. The data logger had a 9-pin serial I/O port to communicate with the computer. All the analogue signals input to the data logger were converted to digital signals and recorded by a lap top PC. The data logger had six differential channels which are labelled as 1H to 6L. These numbers refer to high and low inputs to the differential channels 1 to 6. In a differential measurement, the voltage of the H input is measured with respect to the voltage of L input. When making single-ended measurements, either the H or L input may be used as an independent channel to measure voltage with respect to the data logger analogue (AG). The data logger had eight digital I/O ports which were commonly used for reading the status of an external signal.

The data logger was powered by a 12V power source. A computer communicated to the data logger via Campbell Scientific Data Logger Support Software PC208W. A program was written using the built in language. The program is given in Appendix C.

Both the single-ended measurement method and differential measurement method could be used to connect the signal to the data logger. Since a single-ended measurement was referenced to the data logger ground, any voltage difference between the sensor ground and

data logger ground became a measurement error. Differential measurement avoided this error by measuring the signal between the two leads without reference to ground. Differential measurements were used for the thermocouple temperature measurement and the measurement of current through the heater. However, a single-ended measurement was taken for the voltage measurement of the heater (for a detailed explanation see Section 7.3.2). A 10TCRT thermocouple reference was connected to data logger channel 1, and used as a temperature reference for thermocouples monitored with the data logger. The data logger was also used to control the power supply unit to supply a 10s pulse energy to the heater every 90 minutes. All measurement data were recorded every second.

7.3.2 Electrical Control Circuit

The dual-probe measurement system essentially consisted of the dual-probe, a data logger and a power supply system. The amount of energy applied to the heater was measured by placing a 1Ω±1% precision resistor in series with the power supply unit and the dual-probe heater. The 1Ω±1% precision resistor (product number 320-4687) was sourced from RS, London, UK. According to Ohms' law, the current through the 1Ω resistor would be the same as the current through the heater. If the voltage drop across the 1Ω resistor could be measured, then the current through the 1Ω resistor could be calculated as:

$$I = \frac{V}{R} \tag{7.2}$$

where I = current through the resistor (A)

Therefore, the voltage across the precision resistor was used to determine the current applied to the heating needle. A schematic diagram of the dual-probe control system is shown in Figure 7.8

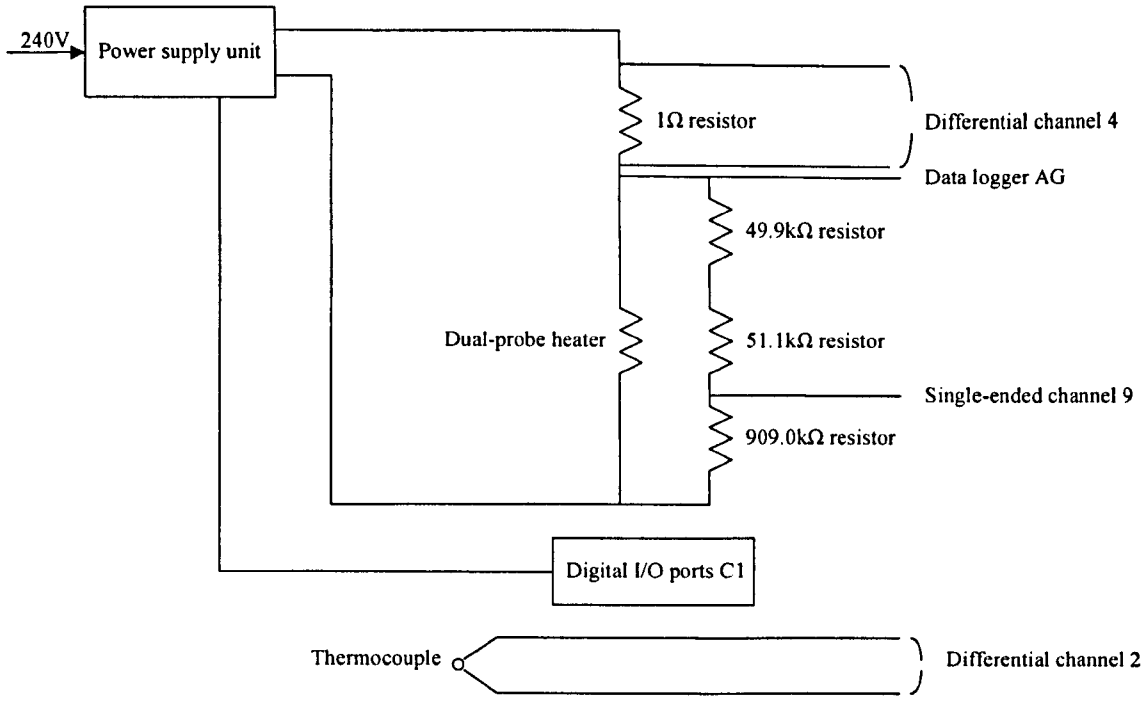

Figure 7.8 A schematic diagram of the dual-probe electric control system

The power supply unit was connected to a 240V supply. The maximum voltage output was 15.6V. The resistance of the 'effective' heater was approximately 28Ω which included the 'real' heater of the dual-probe, and the resistance wire connected to the printed circuit board. The voltage across the 'effective' heater was 15V. Due to the maximum voltage of the data logger common mode being ±2.5V, the data logger could not measure any signal which exceeded ±2.5V. To solve the problem of the data logger's common mode, a voltage divider was applied to the data logger. The voltage divider arrangement in the electric circuit is shown in Figure 7.9. The voltage divider consisted of a 909.0kΩ±0.1% resistor, a 51.1kΩ±0.1% resistor and a 49.9kΩ±0.1% resistor. The 909.0kΩ±0.1% resistor (product number 598-987), the 51.1kΩ±0.1% resistor (product number 340-819) and the 49.9kΩ±0.1% resistor (product number 340-807) were sourced from Farnell in One, Leeds, UK. The 51.1kΩ±0.1% resistor and the 49.9kΩ±0.1% resistor were connected in series and used as one resistor giving 101.0kΩ resistance in total. The relationship between the voltage across the heater V_{in} (V) and the voltage recorded by the data logger V_{out} (V) can be expressed as:

$$V_{out} = V_{in} \times \left(\frac{R_2 + R_3}{R_1 + R_2 + R_3} \right)$$

$$V_{out} = V_{in} \times \left(\frac{51.1 + 49.9}{909.0 + 51.1 + 49.9} \right) \qquad (7.3)$$

$$V_{out} = 0.1 \times V_{in}$$

where R_1, R_2 and R_3 = resistance of the divider (kΩ) shown in Figure 7.9

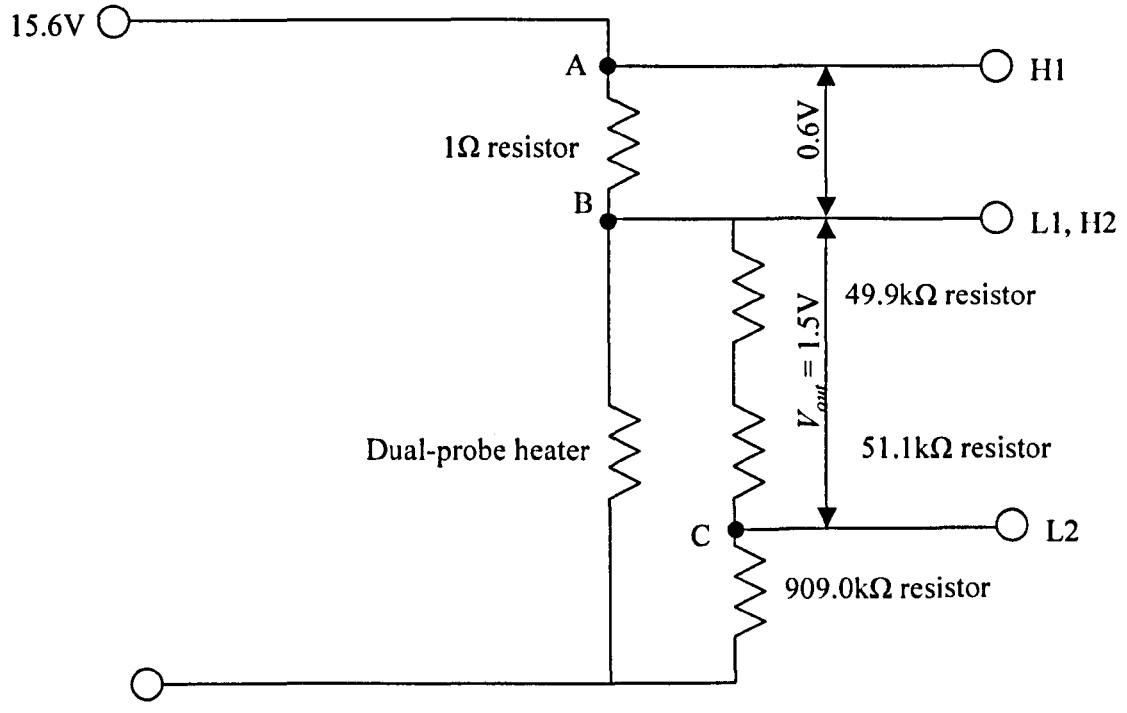

Figure 7.9 A schematic diagram of the divider arrangement in the electric circuit illustrating the problem if a differential measurement was taken for both dual-probe heater voltage and current measurements.

Although differential measurement provides better accuracy (data logger resolution 0.33μV (CR10X Measurement and Control Module Instruction Manual, 1997)), the single-ended method (data logger resolution 0.66μV (CR10X Measurement and Control Module Instruction Manual, 1997)) had to be used for the dual-probe heater voltage measurement. Figure 7.9 shows the data logger channel arrangement if differential voltage measurement had been taken for both dual-probe heater voltage and current measurement. Assuming the dual-probe was tested at full range of 15.6V, the voltage across the voltage divider must be

within the range of the data logger common model. The voltage across points A and B was 0.6V. Points A and B were connected to data logger differential channel H1 and L1. The voltage across points B and C was 1.5V. If a differential voltage measurement was taken for points B and C connected to the data logger, then the data logger differential channel H2 is L1 which would violate the data logger common mode. Therefore, a single-ended voltage measurement was taken for the voltage measurement between points B and C.

The lap top PC was used to control the data logger which was powered by a 12V power source. Control port 1 of the data logger was connected to the power supply unit to supply a pulse of energy to the heater. Differential channel 4 of the data logger was used to record the current through the heater. The signal from the heater was connected to the voltage divider first, then the single-ended measurement was applied to the divider which was installed in channel 9 and analogue ground of the data logger. One thermocouple was installed to the data logger differential channel 2.

Chapter 8

Dual-probe Test and Results

8.1 Introduction

After the four dual-probes were constructed, they were first tested with a water-agar medium to investigate whether the dual-probe would perform as expected. Then the dual-probes were used to measure the volumetric heat capacity of dry aerated concrete samples. Afterwards, the moisture content of conditioned aerated concrete samples was measured.

To achieve a temperature rise of approximately 1°C (for both the dry and conditioned sample measurements) (Section 4.4), the voltage output of the power supply unit was set at 13V (Section 8.2). The method of calculation of energy input to the dual-probe heater is discussed in Section 8.2. The same dual-probe test procedures and data acquisition protocol were applied to the dual-probe measurements of the water-agar medium test as were applied to the dry and conditioned samples test. The 'single-point' and nonlinear model fit methods were used to analyse the dual-probe measured temperature-time data to obtain the maximum temperature rise. This chapter deals with these laboratory based dual-probe tests.

Tables regarding to dual-probe test results are given in Appendix D.

8.2 Voltage and Current Settings for the Power Supply Unit

A total of four 'identical' dual-probes were constructed. Based on the FE model with a spacing of 12mm (Section 5.6.4), and an energy input of 976J/m the dual-probe was predicted to achieve an approximate 1.12°C maximum temperature rise at the temperature sensor needle. Because the heater length was 50mm, the energy input was thus $976\text{J/m} \times 50 \times 10^{-3} = 48.8\,\text{J}$.

This energy pulse was applied over a fixed interval of 10s, therefore the power input to the 'effective' heater was: $P = W/t = 4.88\text{W}$.

A Fluke 22 series II (accuracy of 0.3% of the reading) Digital Multimeter was used to measure the 'effective' heater resistance of the dual-probe, as shown in Table 8.1. The resistance of each of the four heaters was slightly different as expected. The resistance of the 'effective' heater depends on the resistance wire length measured at the beginning for making the heater and the resistance wire length soldered onto the printed circuit board. These two resistance wire lengths could not be exactly the same for the four heaters. The power supply unit had to provide a different voltage output to the four heaters in order to achieve the same power input (4.88W) to the four heaters. For simplicity of operation, the same voltage settings for the four dual-probe heaters were set before the dual-probe tests, and were not changed during the entire test period. Ideally, the energy input to the dual-probe heater experimentally should be the same as the one used in the FE modelling (Section 5.6.4). Then, the maximum temperature rise measured experimentally should be the same as the one predicted by FE modelling. As listed in Table 8.1, the resistance of the four dual-probe heaters was approximately equal to 28Ω. Thus, the heater resistance R =

28Ω was used to calculate the approximate voltage for the dual-probe tests. This voltage was not the same as the one used in FE modelling (Section 5.6.4) because the resistance used to calculate the voltage differed slightly between the dual-probe heaters. Thus, the energy input to each dual-probe heater was not exactly the same as for the FE modelling.

Table 8.1 Heater resistance

	Heater 1	Heater 1*	Heater 2	Heater 3	Heater 4
Resistance (Ω)	28.79	28.52	27.98	27.31	27.82

Note:
1. heater 1* was repaired.

The power input to the dual-probe heater was measured by placing a 1Ω resistor in series with the dual-probe heater and the power supply unit (Section 7.3.2). The electric circuit of this arrangement is shown in Figure 7.8.

To find an approximate value of voltage drop across the four dual-probe heaters, the power calculation formula $P = V^2/R$, V was calculated $V = \sqrt{P \times R} = \sqrt{4.88 \times 28} = 11.69\text{V}$.

The current flow through the heater was calculated from the power calculation formula $P = I^2 R$, I was then calculated as $I = \sqrt{\frac{P}{R}} = \sqrt{\frac{4.88}{28}} = 0.417\text{A}$.

The 1Ω resistor was placed in series with the dual-probe heater and the power supply unit. The current flow through the dual-probe heater and the 1Ω resistor was the same. Thus, the voltage drop across the 1Ω resistor was $V = IR = 0.417 \times 1 = 0.417\text{V}$.

Adding the two voltages together gives the voltage output of the power supply unit. The maximum temperature rise measured at the temperature sensor needle decreased when testing the conditioned samples. An approximately 1°C maximum temperature rise was

expected. The power supply unit output was set at approximately 13V for the dual-probe test.

8.3 Dual-probe Heater 'Effective' Power Calculation

The aim of the dual-probe test was to measure the changes in the samples' moisture content. In order to achieve this goal, it was necessary to measure accurately the power applied to the dual-probe heater.

The dual-probe heater was constructed by winding the resistance wires onto a core 50mm long. The construction of the dual-probe heater is described in detail in Section 7.2.1. The 'real' heater power was calculated by the total power input, multiplied by the ratio of the resistance wire length winding on the core, over the total resistance wire length (except for the wires soldered onto the printed circuit board).

Figure 8.1 shows a schematic diagram of the dual-probe heater used for the power calculation. The total heater resistance wire length was points A to F. AF was typically 300mm long. Points A to B and E to F were where the resistance wires were soldered onto the printed circuit board. The lengths of AB and EF varied from 7mm to 14mm for the four dual-probe heaters, depending on the soldering process. These two pieces of resistance wires could not contribute resistance to the 'effective' heater. The 'effective' heater was defined as the resistance wire length between points B and E. Resistance wires between points B to C and D to E were the wires beyond the dual-probe 'real' heater. The lengths of BC and DE varied from 11mm to 18mm for the four dual-probe heaters. The length of the resistance wire forming the 'real' heater was defined as the wires between points C to D and was typically about 250mm.

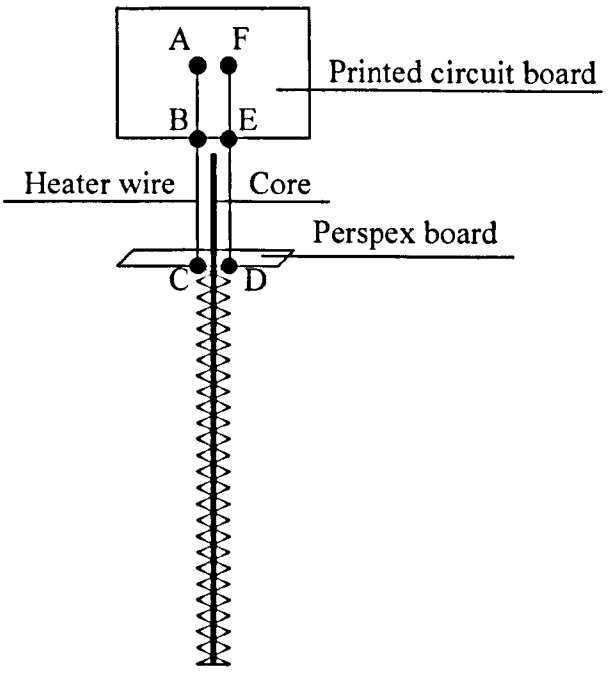

Figure 8.1 A schematic diagram of the dual-probe heater used for power calculations

The data logger measured the voltage drop across the heater, and was equal to the voltage drop across points B to E. The actual voltage drop across the 'real' heater was measured between points C and D. The length of the resistance wire forming the 'effective' heater was calculated as follows:

$$L_{BE} = L_{AF} - L_{AB} - L_{EF} \tag{8.1}$$

where L_{BE} = length of resistance wire between points B and E (mm)

L_{AF} = length of resistance wire between points A and F (mm)

L_{AB} = length of resistance wire between points A and B (mm)

L_{EF} = length of resistance wire between points E and F (mm)

The length of the resistance wire forming the 'real' heater was calculated as follows:

$$L_{CD} = L_{BE} - L_{BC} - L_{DE} \tag{8.2}$$

L_{CD} = length of resistance wire between points C and D (mm)

L_{BE} = length of resistance wire between points B and E (mm)

L_{BC} = length of resistance wire between points B and C (mm)

L_{DE} = length of resistance wire between points D and E (mm)

The ratio of the length of resistance wire forming the 'real' heater to the length of resistance wire forming the 'effective' heater was used to calculate the 'real' power P_{real}(W) input to the dual-probe 'real' heater from the 'effective' power P_{eff}(W) and can be expressed as:

$$P_{real} = P_{eff} \times \frac{L_{CD}}{L_{BE}} \tag{8.3}$$

The lengths of L_{CD} and L_{BE} were 250mm and 280mm typically.

As expressed in Equation (3.8), the energy input (q, J/m) to the heater was used to calculate changes in moisture content. Because a 10s energy pulse was applied to the dual-probe heater, and the length of the dual-probe heater was 50mm, the energy input to the heater was calculated as:

$$q = \frac{t \times P_{real}}{l_h} \tag{8.4}$$

where l_h = the length of the heater (m)

8.4 Dual-probe Test Procedures and Data Acquisition Protocol

The dual-probe test procedures were as follows: for all samples, the dual-probe test involved a 10s energy pulse applied to the dual-probe heater at 90 minute intervals. For the water-agar medium, the dry sample, the conditioned sample (RH=89.0%) and the conditioned sample (RH=96.4%) tests, the temperature at the temperature sensor needle returned to its initial temperature after 80, 75, 67 and 57 minutes of the 10s energy pulse applied to the dual-probe heater. Measurement of the maximum temperature rise for each sample was recorded every second for 24 hours. This allowed the temperature change and the corresponding time to be determined with a sufficiently high resolution. In principle, sixteen measurements were made during the 24 hours test period. However, occasionally data overflow occurred where the data logger did not record data after 00:00, and recovered only after 07:00. Thus, at least eleven measurements were taken for each sample.

The data acquisition protocol was as follows: the initial temperature of the sample T_i (°C) was measured every second and immediately prior to the application of the 10s energy pulse to the heating needle ($q \approx 1100$J/m). T_i was calculated as the average of 1 minute measured temperature before the energy pulse started. By using the average of 1 minute measured temperature data as the initial temperature, the effect of the temperature fluctuation of the thermocouple measurement could be minimized. Thus, the initial temperature could be measured more accurately. The value of the temperature rise ΔT_m (°C) was determined in three stages:

1. For each measurement at the 90 minute intervals, the thermocouple recorded the temperature from the temperature sensor needle every second for 6 minutes after

the 10s energy pulse was applied to the dual-probe heater, i.e., raw data was taken to examine the temperature response at the temperature sensor needle.

2. To find the peak value of the temperature, the raw data was analysed either by a 'single-point' method or a nonlinear model fit method (Section 8.5).
3. The value of the maximum temperature rise was determined by subtracting T_i from the peak value of the temperature obtained in stage 2.

The time t_m (s) when the maximum temperature rise occurred was also determined. The t_m was needed for obtaining maximum temperature rise when applying the 'single-point' method (Section 8.5.1). The energy applied to the dual-probe heater was calculated from recording the voltage across the heater, and the current through the heater. The voltage and current measurements are described in detail in Section 7.3.2. The individual sample dry density was measured after the sample was fully dried in the oven (Section 6.3).

8.5 Dual-probe Test Data Analysis Methods

Temperature-time ($T(t)$) data obtained from a dual-probe can be analysed with two different approaches to determine the sample moisture content. One approach, referred to as the 'single-point' method (Bristow *et al.*, 1995), is based on the accurate determination of the peak value in the temperature-time data after an energy pulse is applied to the dual-probe heater. The second approach involves a nonlinear model fit of the appropriate temperature function of the temperature-time data. Both the 'single-point' method and nonlinear model fit method were used to determine the temperature changes.

8.5.1 'Single-point' Method

For simplicity, the 'single-point' method was used first to analyse the temperature-time data. The peak value of the temperature changes, and the time when the temperature reached this peak were determined by 'visual inspection' of the measured temperature-time data. Microsoft Excel was used to plot a curve of the temperature time-data. The initial temperature was determined by averaging the temperature-time data for 1 minute before the 10s energy pulse was applied to the dual-probe heater. $\Delta T(t)$ was determined as the difference between the measured temperature-time data and the initial temperature. To ensure accurate determination of the peak value of temperature changes and eliminate the effect of temperature fluctuation caused by thermocouple temperature measurement, the peak value of temperature changes was obtained by averaging the temperature-time data over the period that the peak temperature occurred. An example of this determination of the maximum temperature rise is detailed in Section 8.7.

Noise in the $\Delta T(t)$ data is inevitable in this type of experiment. This noise affects the accuracy of temperature measurement. Noise can occur randomly, as well as being caused by an uncontrolled external signal which interferes with the dual-probes' temperature measurement system, i.e., the data logger and thermocouple. An example of the typical noise experienced in the experiment is given in Figure 8.2. The nonlinear model fit method was expected to reduce the effect of noise on the maximum temperature change measurement.

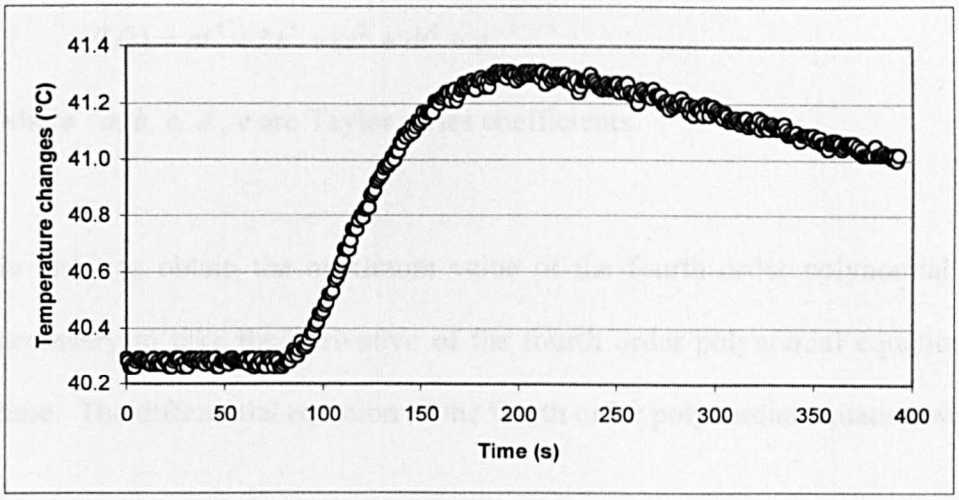

Figure 8.2 Noisy data experienced in the dual-probe measurement

8.5.2 Nonlinear Model Fit Method

The procedure of the nonlinear model fit method was as follows: first, a set of measured temperature-time data was fitted to a polynomial function with order of *n* using Microsoft Excel. The order *n* of polynomial equation varied from 2 to 6 with the R^2 value changes of each order being observed. The range of temperature-time data used to fit the polynomial equation was also changed to observe the R^2 value changes. A fourth order polynomial fit was mostly successful at giving a R^2 value closest to 1, and so the fourth order polynomial equation was chosen as the polynomial fit function. To best fit the measured temperature-time data to the fourth order polynomial equation, the range of temperature-time data was changed slightly depending on the sample used and whether it was conditioned. For the dry aerated concrete sample test, the temperature-time data of 30s to 340s after the dual-probe heater being heated was used. For the conditioned aerated concrete sample test, the temperature-time data of 40s to 340s after the dual-probe heater being heated was used. The fourth order polynomial equation was selected to be used in the nonlinear model fit method (MATLAB, The MathWorks, Inc., Massachusetts, USA):

$$T(t) = at^4 + bt^3 + ct^2 + dt^1 + e \qquad (8.5)$$

where a, b, c, d, e are Taylor series coefficients.

In order to obtain the maximum value of the fourth order polynomial equation, it was necessary to take the derivative of the fourth order polynomial equation with respect to time. The differential equation of the fourth order polynomial equation was then:

$$T'(t) = 4at^3 + 3bt^2 + 2ct + d \qquad (8.6)$$

Then, it was necessary to set the differential equation equal to zero. The software 'MATLAB' (**roots** command, (MATLAB, The MathWorks, Inc., Massachusetts, USA)) was used to obtain the t_m value relevant to the occurrence of the maximum temperature changes so that $T'(t_m) = 0$.

Finally, it was necessary to substitute the value of t_m backing to the fourth order polynomial equation. The maximum temperature changes were obtained as $T(t_m)$ via 'MATLAB' (**polyval** command, (MATLAB, The MathWorks, Inc., Massachusetts, USA)).

An example of the determination the maximum temperature rise using the nonlinear model fit method is detailed in Section 8.8.

After obtaining the peak value of the temperature changes either by the 'single-point' method, or the nonlinear model fit method, the maximum temperature rise could be obtained by subtracting the initial temperature from the maximum value of the temperature changes.

8.6 Dual-probe Test in a Water-agar Medium

The first dual-probe test was carried out in a water-agar medium after the construction of the dual-probe. These experimental results provided an indication as to whether the dual-probe was working as expected.

To prevent natural convection in the water, a water-agar medium with a concentration of 0.2% agar was used in the dual-probe test. This approach was suggested by Campbell *et al.* (1991). This small amount of agar was assumed to have a negligible effect on the specific heat of water (Campbell *et al.*, 1991). A pot with diameter of 20cm and depth of 13cm was used as the container for the water-agar medium. The agar (product number ALDRICH-28, 289-8) was sourced from the Sigma-Aldrich Company Ltd., Dorset, UK. The procedures for preparing the water-agar medium were as follows:

1. Measure the distilled water and agar powder to the required amounts.
2. Mix the agar powder and distilled water together.
3. Heat the mixture of distilled water and agar and boil for five minutes.
4. Install the dual-probe into the water-agar medium.
5. Wait for the water-agar medium to cool to room temperature.

Because the dual-probe test on the water-agar medium was conducted at room temperature, any background temperature changes of the water-agar medium affected the dual-probe temperature measurements. A thermocouple was thus used to measure the background temperature of the water-agar medium. By recording the difference between the dual-probe measured temperature and the thermocouple measured background temperature of the water-agar medium, it was therefore possible to 'remove' changes in background temperature from the signal received at the temperature sensor probe (Bristow *et al.*, 1993).

Once an energy pulse measurement had been made, the experiment was paused until the sensor and background temperature had re-equilibrated before taking another reading. A 90 minute intervals was used for each test. A schematic diagram of the temperature measurement points is shown in Figure 8.3. The locations of dual-probe and thermocouple are determined as follows:

1. The dual-probe and thermocouple were located at equal distance from pot center along the vertical axis. Thus, when the temperature of the water-agar medium was at equilibrium with the environment, the thermocouple measured temperature represented the temperature of the water-agar medium where the dual-probe was installed.
2. The thermocouple was kept a certain distance (tested experimentally) from the dual-probe so that the thermocouple background temperature measurement would not be affected by the heater when it was heated up.
3. The dual-probe was kept a certain distance from the edge of the pot so that the water-agar medium's boundary was at the correct distance (tested experimentally).

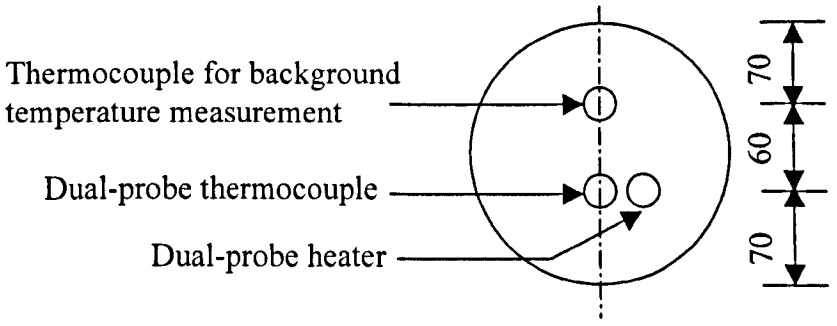

Figure 8.3 A schematic diagram of the measurement point in the water-agar medium

A fan was used for air ventilation in the laboratory where the dual-probe was tested. There was airflow through the hole where the fan was installed, even if the fan was not operated. To reduce the effect of the convective heat transfer on the water-agar medium background

temperature, the pot containing the water-agar medium and the dual-probe was packed in a box made of 25mm thick polystyrene.

Compared to aerated concrete, the 'known' volumetric heat capacity of the water-agar medium (Campbell *et al.*, 1991) was much higher. The volumetric heat capacity of aerated concrete and the water-agar medium were 0.651MJ/m^{3}K and 4.18MJ/m^{3}K, respectively. To achieve the same maximum temperature rise in both materials, the dual-probe for the water-agar medium required greater energy input. Ideally, a maximum temperature rise of approximately 1°C was expected. However, the maximum temperature which the resistance wire coating could bear was limited, and a higher energy input may have burnt out the dual-probe heater, thereby destroying the dual-probe as a whole. A test of voltage across the dual-probe heater was carried out with the resistance wire coating intact. Because more energy input was needed for the dual-probe to test the water-agar medium compared to the aerated concrete, the power supply unit used for testing aerated concrete could not provide sufficient voltage output. Thus, a DC power supply unit was used to provide a 22.3V voltage output for the dual-probe test on the water-agar medium.

A total of eleven measurements were made and are shown in Table D.1. The maximum temperature rise was determined by the 'single-point' method. The volumetric heat capacity of the water-agar medium measured by dual-probe was 3.98MJ/m^{3}K. The difference between the measurement and the standard value of water volumetric heat capacity (Incropera *et al.*, 1985) was 4.8%. Previous studies found that the probe spacing affected the experimental results significantly (Bristow *et al.*, 1993 and 1994; Noborio *et al.*, 1996; Tarara and Ham, 1997). The probe spacing was measured to 11.8mm in this test. The maximum background temperature changes were 0.01°C - this would not have affected the test results significantly.

8.7 Dual-probe Test with the Dry Aerated Concrete Samples

The dual-probe water-agar medium test results indicated that the dual-probe was working as expected. This section now considers the measurement of the moisture content of aerated concrete. As previously discussed (Section 3.2), the changes in moisture content can be calculated by knowing the maximum temperature rise of the sample at different moisture levels. The dual-probe was used to measure the maximum temperature rise; the changes in the sample moisture content could then be deduced. The aim of the dry aerated concrete test was to provide one known test condition in order to measure the changes of moisture content for samples which could later be conditioned to higher moisture content. In this experiment, accurate temperature and power measurements were key factors in ensuring the dual-probe moisture was measured successfully.

As described in Section 6.3, the aerated concrete samples were initially dried in the oven. The dual-probe dry sample test started after the sample was fully dried. To prevent any air gap occurring between the drilled hole surface of the sample, and the outer surface of the dual-probe needles, heat sink compound (product number 554-331) was applied to both the heating needle and the temperature sensor needle. As a check, the real probe spacing was also measured by cutting the sample open after the experiment of moisture content measurement had been performed. The additional procedures for the dry sample test were as follows:

1. Take the dry samples out of the oven.
2. Measure the mass of the sample.
3. Measure the mass of the dual-probe.
4. Apply heat sink compound to the dual-probe needles.

5. Measure the mass of the dual-probe and the heat sink compound.
6. Insert the dual-probe into the sample.
7. Put the sample into the airtight container and seal it.
8. Leave the airtight container in a 40°C oven.
9. Start the dual-probe test once the sample and the oven reach a stable temperature of 40°C. The details of conditioning the samples are described in Section 6.4.

A total of nine dry samples were tested, named No.1 to No.9 and are shown in Tables D.2 to D.10. The maximum temperature rise was determined by the 'single-point' method. The principle of the 'single-point' method is described in Section 8.5.1. The details of maximum temperature rise determination are described via an example which is the 4^{th} test of No.2 dry sample measurements and shown in Figure 8.4. t_0(s) refers to the time 1 minute before the energy pulse was applied to the dual-probe heater, and was assumed to be 0. Heating started at t_1 = 60s, and was terminated at t_2 = 70s. The initial temperature was determined by averaging the temperature-time data from 0 to 60s, i.e., 40.21°C. The maximum temperature rise occurred between 214s and 240s later than t_0 (154s to 180s later than t_1). The peak value of the temperature changes was obtained by averaging the temperature-time data over the period between 214s and 240s, i.e., 41.53°C. Subtracting the initial temperature (40.21°C) from the peak value of the temperature changes (41.53°C), resulted in a maximum temperature rise of 1.32°C.

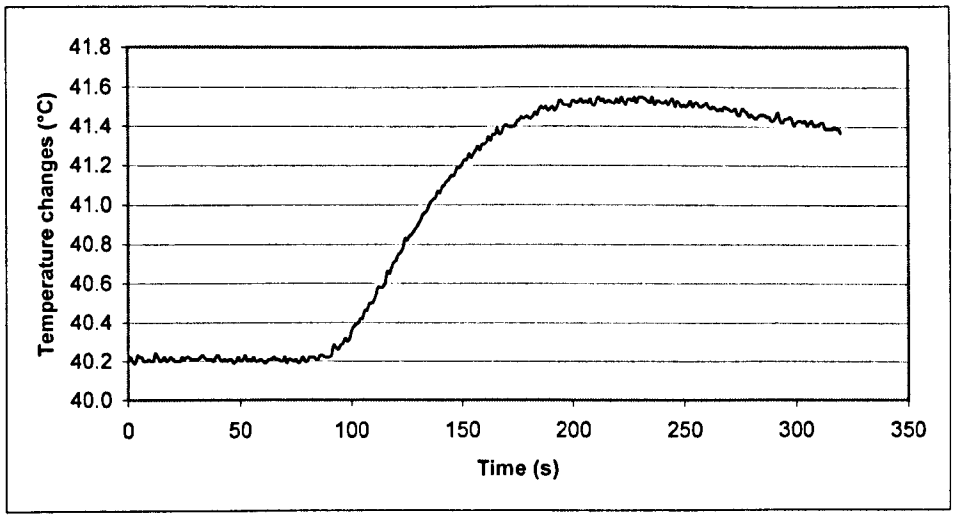

Figure 8.4 Dual-probe measured temperature changes of a dry sample test

From the dual-probe test results (Tables D.2 to D.10), it can be seen that:

1. For nine samples, the difference between the dual-probe measured and the laboratory measured volumetric heat capacities ranged between 0.2% and 7.9%. Each sample's density was measured individually in the laboratory and the results are given in Table 6.2. Note that, the specific heat of each individual sample was not measured in the laboratory due to time limitations. As a general check of the manufacturer's data of specific heat, the specific heat was measured in the laboratory (Appendix E). The difference between the laboratory measured specific heat and the manufacturer's data ranged between 1% and 3%. The laboratory measured specific heat was taken to calculate the volumetric heat capacity measured in the laboratory.
2. For the nine samples, the difference between the dual-probe measured volumetric heat capacity and the manufacture's data ranged between 0.1% and 5.2%. The manufacturer's data of density and specific heat was quoted in the literature (CELCON, 2003) of H+H CELCON Ltd. Private communication with Mr. Doug Harris (the R&D manager with H+H CELCON Ltd) confirmed that the

manufacturer's data was derived from standard measurements undertaken by CELCON R&D Department.

In general then it appears that the results of these experiments were encouraging and provided confidence in the dual-probe. The small 'errors' that were observed relate, in part at least, to the fact that a truly independent value of volumetric heat capacity was not available for each individual sample. However, the data that was used for comparative purposes was felt to be robust enough for the purposes of this experiment.

The errors will, of course, also relate to experimental errors. A series of possible errors are detailed in Section 8.10. However, it is also possible that improper installation of the thermocouple could have led to poor temperature measurement, i.e., the thermocouple may not have been installed down to the bottom of the temperature sensor needle. Secondly, contact resistance between the probe outer surface and drilled hole surface could also lead to poor temperature measurement, i.e., the heat sink compound may not have been applied to the probe surface evenly.

8.8 Dual-probe Test Using the Conditioned Aerated Concrete Samples

Aerated concrete samples were next conditioned with air RH of 89.0% and 96.4%, respectively. By testing the maximum temperature rise of the conditioned sample and knowing the dry samples' maximum temperature rise with the same energy input to the dual-probe heater, the changes of moisture content could be obtained.

The same samples were tested as for the dry sample tests (see Chapter 6 for details of the conditioning sample). Five samples were conditioned with air RH of 89.0%. These five samples reached an equilibrium moisture content after 70 days conditioning. Four other samples were conditioned with air RH of 96.4%. However, these four samples did not reach an equilibrium moisture content even after 213 days conditioning.

The testing of the conditioned samples, test method, procedures, data acquisition protocol and data analysis were the same as for the dry sample testing. The energy input to the dual-probe heater was also the same in both dry sample and conditioned sample tests. Because the heater of No.1 dual-probe had to be repaired, the heater's electrical resistance was changed. The heat output of the heater was calculated as $P = V^2/R$, therefore the heat output of the heater was changed even if the same voltage input was applied to the heater. A correction of maximum temperature rise was then applied to the conditioned sample No.1.

Figure 8.5 shows an example of conditioned sample measurements. Comparison of the dual-probe test results between dry and conditioned samples measurements is shown in Figure 8.6.

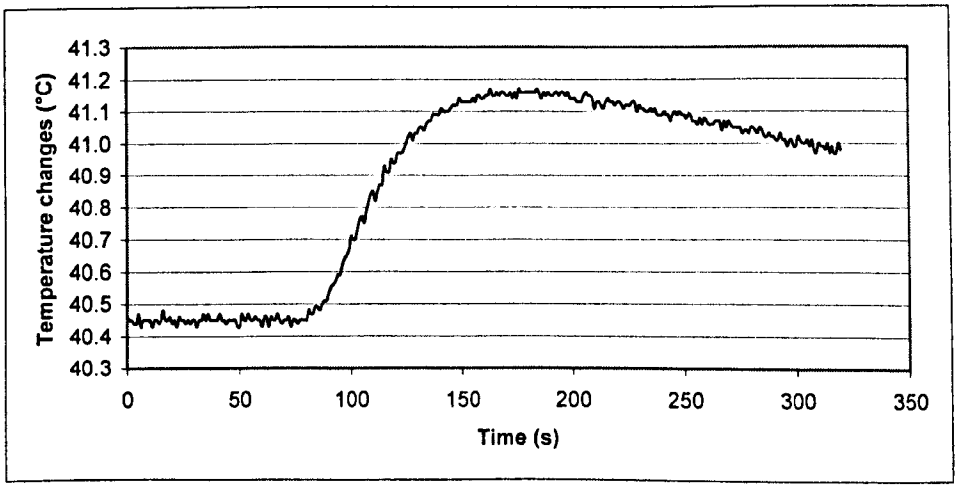

Figure 8.5 Dual-probe measured temperature changes of a conditioned sample test

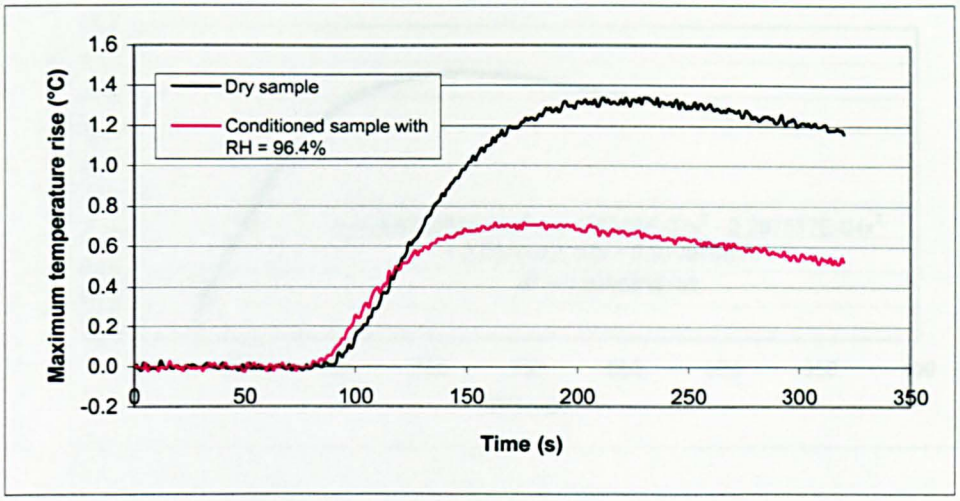

Figure 8.6 A comparison of the dual-probe measured maximum temperature rise of a sample in dry and conditioned states

The principle of the nonlinear model fit method was given in Section 8.5.2. Here, the nonlinear model fit for obtaining the maximum temperature rise is described in more detail via an example. A fourth order polynomial equation was used to fit the temperature-time data. To compare the difference between the 'single-point' method and the nonlinear model fit method, the measured temperature-time data used to determine the maximum temperature change was the same for both methods (the 4th test of No.2 dry sample measurement). With the nonlinear model fit method, the heating time was initialised at t_1=0s. Suppose the data to fit a fourth order polynomial equation was from 30s to 340s as shown in Figure 8.7. The temperature changes can be expressed as:

$$T(t) = -6.672088E-10t^4 + 5.408558E-07t^3 - 2.287517E-04t^2 + 3.987065E-02t + 3.910676E+01 \quad (8.7)$$

The corresponding R^2 value was 0.994.

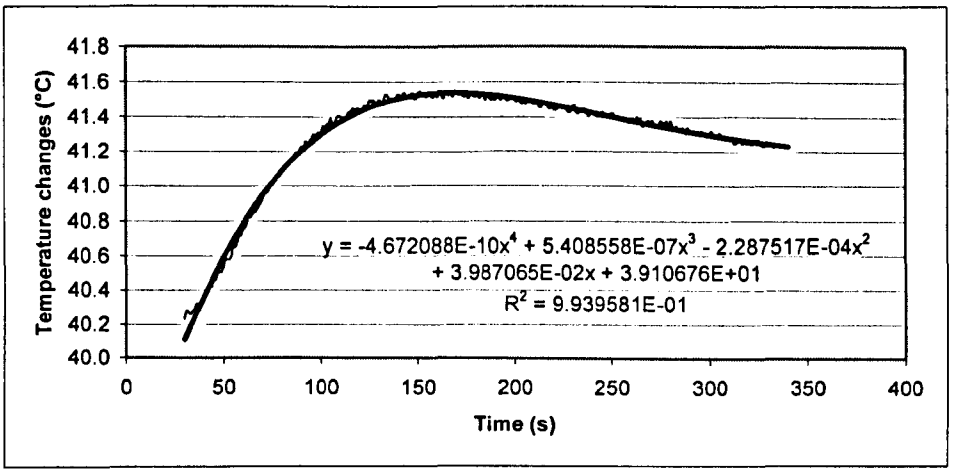

Figure 8.7 Nonlinear model fit using 30s to 340s data

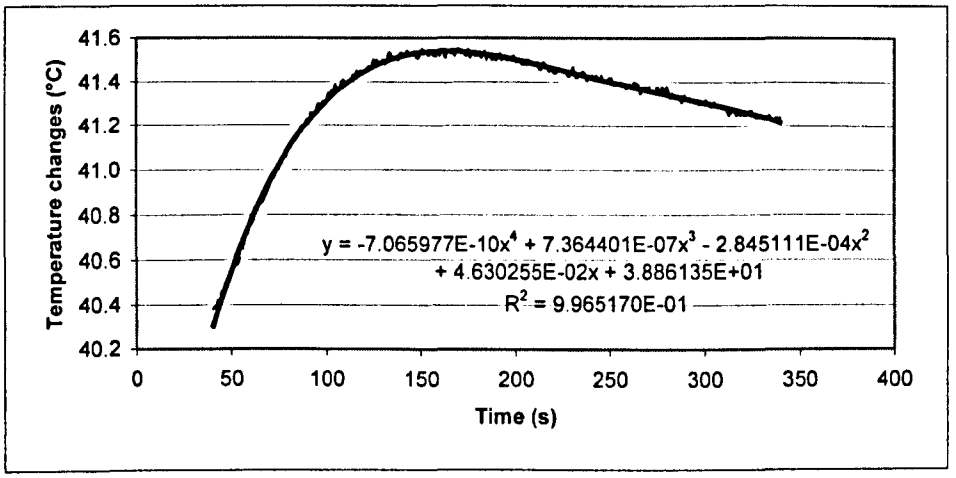

Figure 8.8 Nonlinear model fit using 40s to 340s data

Now changing the data range to fit a fourth order polynomial equation, from 40s to 340s as shown in Figure 8.8, the temperature changes can be expressed as:

$$T(t) = -7.065977E-10t^4 + 7.364401E-07t^3 - 2.845111E-04t^2 + 4.630255E-02t + 3.886135E+01 \quad (8.8)$$

The corresponding R^2 value was 0.997. After comparing these two equations' R^2 values, Equation (8.8) was selected as the fit function.

Equation (8.8) was then differentiated with respect to time and the equation was made to equal 0.

$$T'(t) = -4 \times 7.065977E-10t^3 + 3 \times 7.364401E-07t^2 - 2 \times 2.845111E-04t + 4.630255E-02 = 0 \quad (8.9)$$

By solving the third order polynomial equation, t_m was found to be 163s.

The value of t_m was then substituted back into the fourth order polynomial Equation (8.8). The peak value of the temperature changes was found to be 41.54°C. Thus, the maximum temperature changes was determined to be 1.33°C.

As noted previously (Section 8.5.2), the software 'MATLAB' was used to solve these calculations. The commands used in the MATLAB were (MATLAB, The MathWorks, Inc., Massachusetts, USA):

$p1 = [-7.065977E-10\ \ 7.364401E-07\ \ -2.845111E-04\ \ 4.630255E-02\ \ 3.886135E+01]$

$p2 = [-4 \times 7.065977E-10\ \ 3 \times 7.364401E-07\ \ -2 \times 2.845111E-04\ \ 4.630255E\text{-}02]$

$roots(p2)$

$polyval(p1,\ 163)$

where 163 was the root of $p2$, i.e., the time when maximum temperature changes occurred.

The maximum temperature rise determined by the 'single-point' method was 1.32°C (Section 8.7). The maximum temperature rise determined by the nonlinear model fit

method was 1.33°C which was 0.01°C higher than that of the 'single-point' method. The t_m determined by the 'single-point' method was 154s to 180s later than t_1 (Section 8.7). Applying the nonlinear model fit method to extract the maximum temperature rise, t_m was found to be 163s later than t_1. This was within the t_m range of the 'single-point' method.

The dual-probe test results are shown from Tables D.11 to D.19. The maximum temperature rise of samples No.1 to No.9 was determined by the 'single-point' method. To compare the effect of the 'single-point' method and the nonlinear model fit method on the maximum temperature rise and hence the moisture content, the maximum temperature rise of sample No.5 was determined both by the 'single-point' method and the nonlinear model fit method. From the test results of sample No.5 shown in Table D.20, it can be seen that:

1. The maximum temperature rise of the dry sample test determined by the 'single-point' method was 0.01°C lower than that of the nonlinear model fit method.
2. The maximum temperature rise of the conditioned sample determined by the 'single-point' method was 0.02°C lower than that of the nonlinear model fit method.
3. The moisture content obtained both by the 'single-point' method and nonlinear model fit method was thus almost the same.

Thus it appears that it was not necessary to use the nonlinear model fit method to determine the maximum temperature rise for the aerated concrete sample test. The nonlinear model fit method, however, has advantages when analysing sparse, noisy data.

From both dry sample and conditioned sample measurements, it was found that the initial temperature of the sample ranged between 39.6°C and 40.6°C. The samples were placed in different locations inside the airtight container. Two airtight containers were located in

different places inside the oven. The temperature distribution of the oven was not investigated. If uneven temperature distribution inside the oven had occurred, the samples could have had different initial temperatures. The changes of room temperature could also have affected the changes of oven temperature as the oven was located in the room without temperature control (Appendix B). However, the dual-probe results from the dry and conditioned samples measurements indicated that the initial temperature of the sample did not change significantly over the 24 hours test period. Thus it appears that the initial temperature difference of each sample did not affect the dual-probe moisture content measurements.

To verify the dual-probe moisture content measurement results, the moisture content of the conditioned sample was also measured gravimetrically. Knowing the dry and the wet mass of the sample, the moisture content of the whole sample was determined. A comparison of the dual-probe moisture content test results, and the whole sample moisture content determined by gravimetric method is shown in Table D.21. When comparing the dual-probe test results and the gravimetric test results, good agreement was achieved for all eight samples except for the sample No.1. The maximum temperature rise may not be measured accurately in sample No.1 test due to the measurement errors as discussed in Section 8.7. Error analysis results (Table D.11) show that the absolute error in sample No.1 measurement was 0.02kg/kg.

The *whole* sample moisture content was measured gravimetrically in this way. However, the moisture distribution inside the sample may have been uneven. Thus, after completion of the dual-probe conditioned sample tests, the conditioned samples of No.1 to No.6 were cut into smaller pieces weight and then dried in the oven at 105°C. Due to time limitations, the conditioned samples No.7 to No.9 were not tested. Sample No.5 was cut first. It was cut to the measurements 10mm×10mm×10mm at the start point, 10mm away from the

drilled holes of the sample in the direction of sample length. These samples were cut to a maximum 30mm deep from surface. Because the mass of the small pieces of the sample was low, any measurement error in mass would result in significant changes in moisture content. Therefore for the other samples, the size of the smaller samples was altered to 20mm×30mm×11mm. This would give approximately 4g dry mass. These samples were taken 10mm away from the two holes of the sample, in the direction of sample length. A schematic diagram of the position of the smaller pieces sample is shown in Figure 8.9.

The moisture content of the conditioned samples No.5 and 6 is shown in Table D.22. It can be seen that the difference of moisture content over 18 pieces of sample was 0.02kg/kg.

For the cases, when the samples did not reach equilibrium with RH = 96.4% moist air, the moisture content inside the conditioned samples No.1 to 4 is shown in Table D.22. It can be seen that the moisture content in the centre of the sample was higher than that in the area close to the surface and bottom of the sample. The oven temperature was varied over the whole sample conditioning period (Appendix B). The RH of the moist air was varied corresponding to the changes of temperature. It seems likely, then, that the samples started to dry out in the later stages of the sample conditioning period.

Note that samples No.7 to No.9 were also tested by an electrical resistance method (the 'protimeter'). Detailed comparison of the three methods (dual-probe, electrical resistance method and gravimetrical) is given in Appendix F.

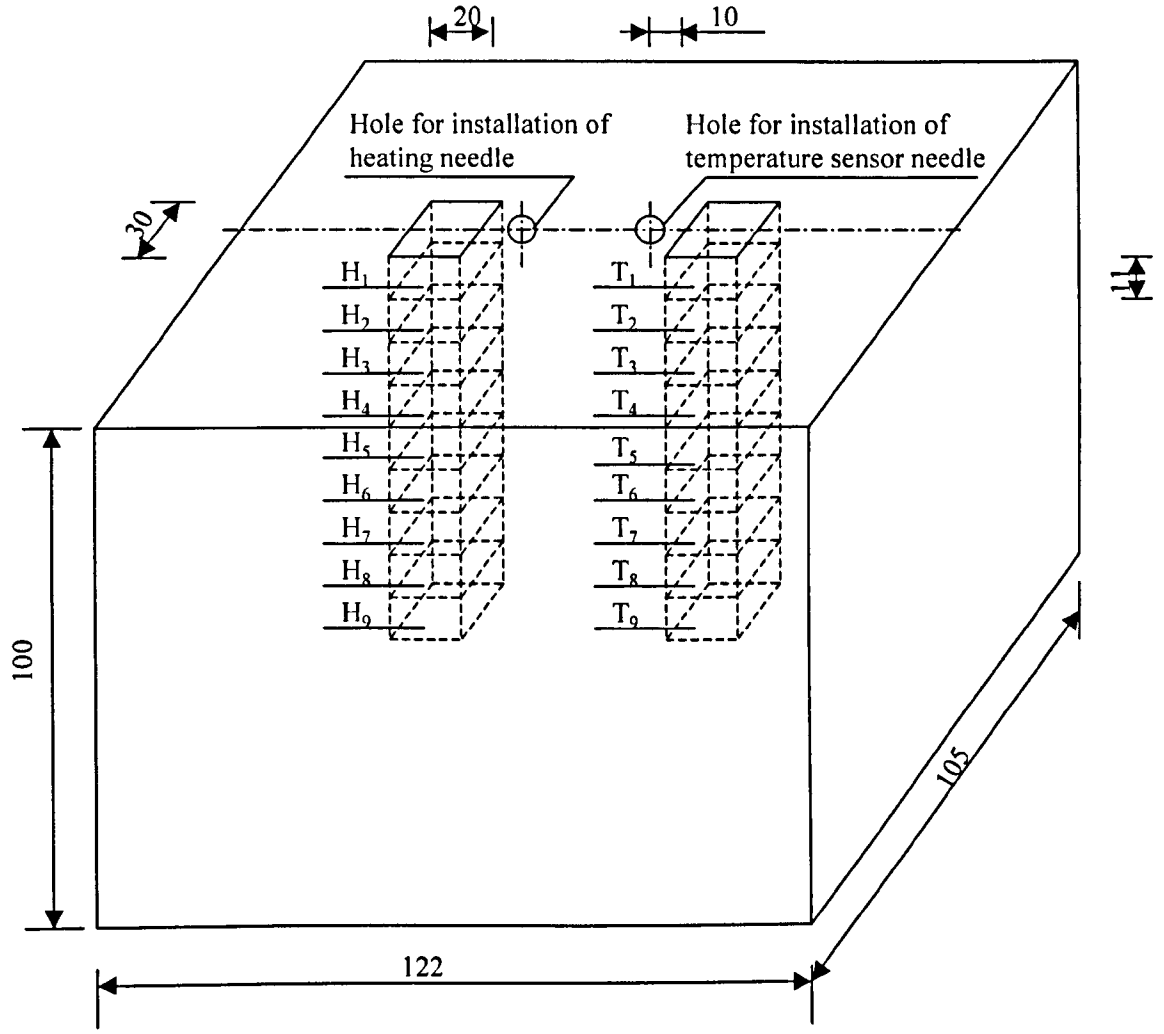

Note:

1. H_1 indicates that the sample was cut from the heating needle's side and from the sample surface to 11mm deep.
2. H_9 indicates that the sample was cut from the heating needle's side and 88mm from the surface to the start of the sample.
3. T_1 indicates that the sample was cut from the temperature sensor needle's side and from the sample surface to 11mm deep.
4. T_9 indicates that the sample was cut from the temperature sensor needle's side and 88mm from the surface to the start of the sample.

Figure 8.9 A schematic diagram of the position of the small pieces cut from an original sample

8.9 Thermal Properties and Changes of Moisture Content as Determined by Fitting the Analytically Determined Temperature Rise to the Experimental Data

The thermal properties (heat conductivity and diffusivity), of the test material can be determined by fitting the analytically determined temperature rise of a dual-probe to the experimental data. In the dual-probe theory, the temperature rise in Equation (3.1) is a function of time, energy input, probe spacing and thermal diffusivity of the test medium. In the aerated concrete moisture content measurement, the manufacturer's data for thermal conductivity and volumetric heat capacity for dry samples are provided (Table 5.1) and can be used as *initial* values to calculate the temperature rise. Equation (3.1) is used to fit the analytical temperature rise to the experimental data. Now, Q in Equation (3.4) substituted into Equation (3.1) yields:

$$\Delta T = \frac{q}{4\pi kt\rho c_p}\exp\left(\frac{-r^2}{4kt}\right) \tag{8.10}$$

The relationship between k, λ and ρc_p is expressed in Equation (4.11)

Substituting Equation (4.11) into Equation (8.10) yields:

$$\Delta T = \frac{q}{4\pi\lambda t}\exp\left(\frac{-r^2}{4kt}\right) \tag{8.11}$$

Considering the initial temperature of the test sample,

$$T = \frac{q}{4\pi\lambda t}\exp\left(\frac{-r^2}{4kt}\right) + T_i \qquad (8.12)$$

Microsoft Excel is used to fit the analytical temperature rise to the experimental data in order to determine the 'best' values of the thermal diffusivity and thermal conductivity. The volumetric heat capacity can then be calculated using Equation (4.11). By determining the volumetric heat capacity of the dry and conditioned samples, the changes in moisture content can thus be obtained.

The 4th test of dry sample No.2 and the 14th test of conditioned sample No.2 will now be taken as examples. The measured and analytically determined (best fit) plots of temperature rise versus time of these two tests are shown in Figures 8.10 and 8.11. The numerically calculated data is also shown for comparison purposes.

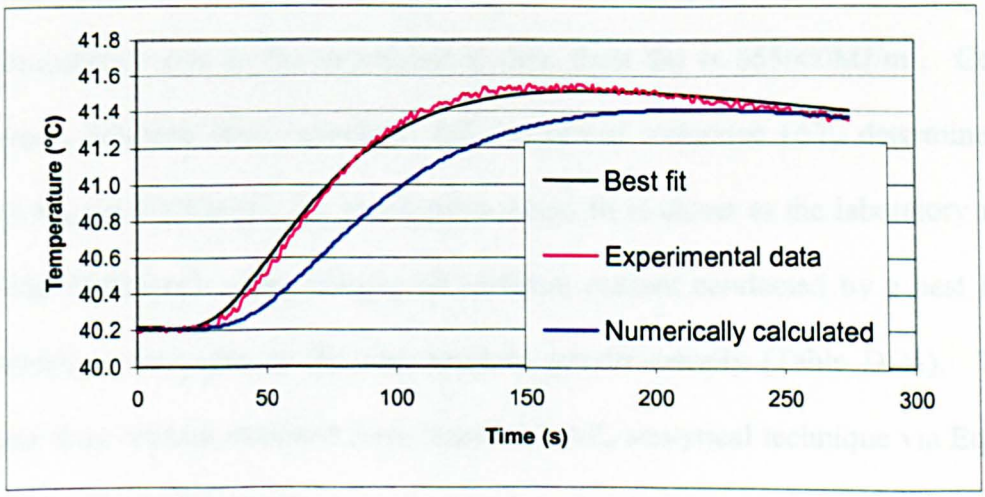

Figure 8.10 An example of numerically calculated temperature, analytically determined temperature (best fit) and measured temperature vs time for dual-probe dry sample measurement

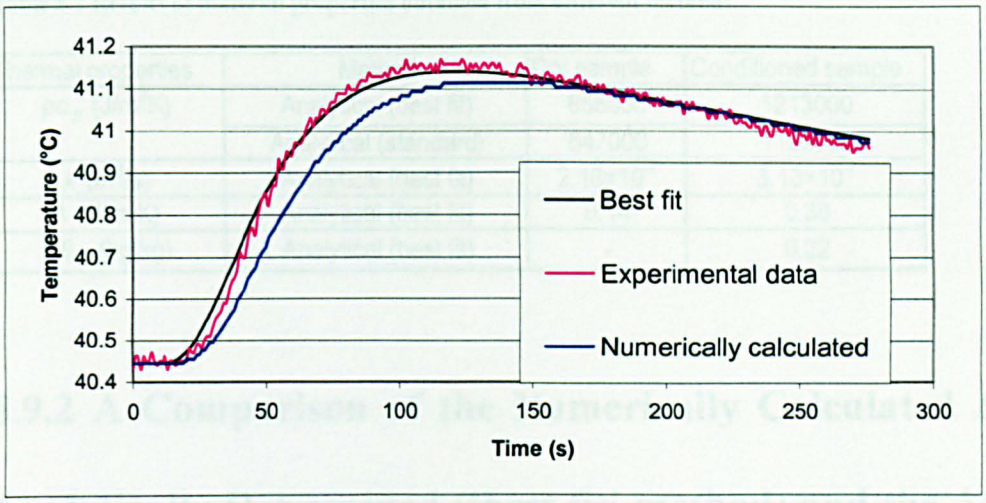

Figure 8.11 An example of numerically calculated temperature, analytically determined temperature (best fit) and measured temperature vs time for dual-probe conditioned sample measurement

8.9.1 A Comparison of Results Obtained from Fitting the Analytically Determined Temperature Rise to the Experimental Data and those from the 'Standard' ΔT_m Analytical Technique

The thermal properties measured by the dual-probe are listed in Table 8.2. The volumetric heat capacity of the dry sample No.2 obtained by fitting the analytically determined temperature rise to the experimental data (best fit) is 655000MJ/m^3. Compared to the result obtained from 'standard' ΔT_m analytical technique (ΔT_m determined by Equation (3.5)), 647000MJ/m^3, the result from a best fit is closer to the laboratory measured value (652000MJ/m^3). The changes of moisture content conducted by a best fit is 0.22kg/kg which is the same as the one obtained gravimetrically (Table D.21). The changes of moisture content obtained from 'standard' ΔT_m analytical technique via Equation (3.10) is 0.21kg/kg (Table D.12).

In general, it can be seen that the material's thermal properties and the changes of moisture contents obtained from a best fit method is closer to the real values.

Table 8.2 Results of material properties obtained from different methods

Thermal properties	Method	Dry sample	Conditioned sample
pc_p (J/m^{3}K)	Analytical (best fit)	655000	1213000
	Analytical (standard)	647000	1192000
k (m^2/s)	Analytical (best fit)	2.18×10^{-7}	3.13×10^{-7}
λ (W/mK)	Analytical (best fit)	0.14	0.38
$\Delta\theta_m$ (kg/kg)	Analytical (best fit)	-	0.22

8.9.2 A Comparison of the Numerically Calculated ΔT_m to the Analytically Determined ('best fit' method) and the Analytically Determined ('standard' method) ΔT_m

For the dry sample measurement, the maximum temperature rise obtained by numerical calculation is 0.12°C lower than the experimental measured data and 0.11°C lower than the analytically determined maximum temperature rise. This is consistent with the results of numerical model work in Chapter 5. For the conditioned sample measurement, the maximum temperature rise obtained by numerical calculation is 0.04°C lower than the experimental measured data and 0.03°C lower than the analytically determined maximum temperature rise. There is a time delay for the numerical calculated temperature to reach the peak value compared to the analytical ones. The numerical calculated temperature rise applies short-duration heat pulse to the line source, i.e., a 10s pulse of energy. The analytical temperature rise applies the theory of an instantaneous line source. The time delay was caused by the short-duration heat pulse (Bristow *et al.* 1994a and b). However, the short-duration heat pulse has little effect on the maximum temperature rise (Bristow *et al.* 1994a and b). Therefore, it is still possible to obtain accurate volumetric heat capacity by applying the instantaneous theory via Equation (3.5) with short-duration heat pulse (Bristow *et al.* 1994a and b).

8.10 Error Analysis

Errors in the dual-probe measurements will arise due to uncertainties in r, q, ΔT etc. Over the range of 6 to 50°C, for temperature (T) measurements, the four thermocouples were calibrated against a reference thermometer (quartz crystal thermometer). As a result, the *absolute* error of the thermocouple calibration was ±0.05°C. However, systematic error and random error were still present in the calibrated thermocouple. The systematic error however, will be reduced for the *relative* measurement of temperature changes (ΔT). Thus, an estimation of ±0.01°C was made for this reduction. Therefore, the thermocouple calibration error used for dual-probe temperature changes (ΔT) measurement was taken to be ±0.04°C. The details of thermocouple calibration are given in Appendix B.

If one again considers the parameters in Equation (3.5), an issue relating to the manufacturing of the heating needle becomes apparent. q, the energy supplied per unit length, may not be idealised if the resistance wire was not wound uniformly up the length of the heating needle as shown in Figure 8.12. If the resistance wire was more densely or rarely packed in this region, the energy dissipated at that point would have exceeded or been less than the proposed amount, and hence may have caused a change in ΔT_m. Although every effort was made to reduce this effect, a technique may need to be developed for improving the heater winding apparatus in the future.

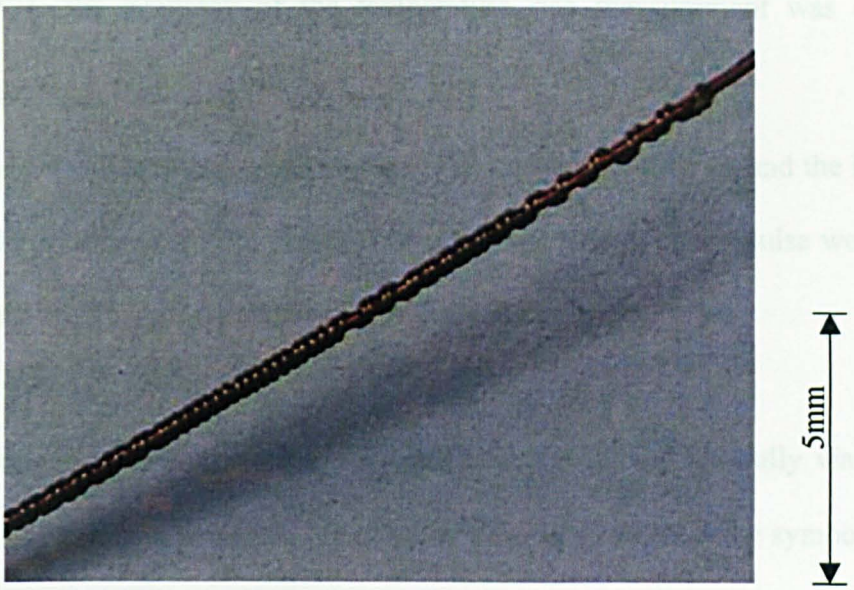

Figure 8.12 Heater was not wound uniformly

The error associated with the ρc_p and $\Delta\theta_m$ tests was analysed systematically.

8.10.1 Error Analysis in ρc_p

In order to investigate the errors associated with ρc_p it was necessary to consider the error of the parameters within Equation (3.5).

$$\rho c_p = \frac{q}{e\pi r^2 \Delta T_m}$$

Three parameters in the above equation needed to be considered with regard to the error in ρc_p. The corresponding error sources dr, $d(\Delta T_m)$ and dq are analysed as follows:

1. dr: measurement error of the real hole spacing. This was obtained by cutting the sample open after the sample test was completed.

2. $d(\Delta T_m)$: the accuracy of the temperature rise measurement was obtained by thermocouple calibration.
3. dq : dq was calculated using voltage (V), current (I), time (t) and the length of the resistance wire (l_w). The power source and the timing of the pulse were measured and recorded by the data logger with associated errors.

The errors associated with the power calculation are examined carefully via an example calculation of dry sample No.2 test. Below, the electric circuit and the symbol used in the error calculation are shown in Figure 8.13.

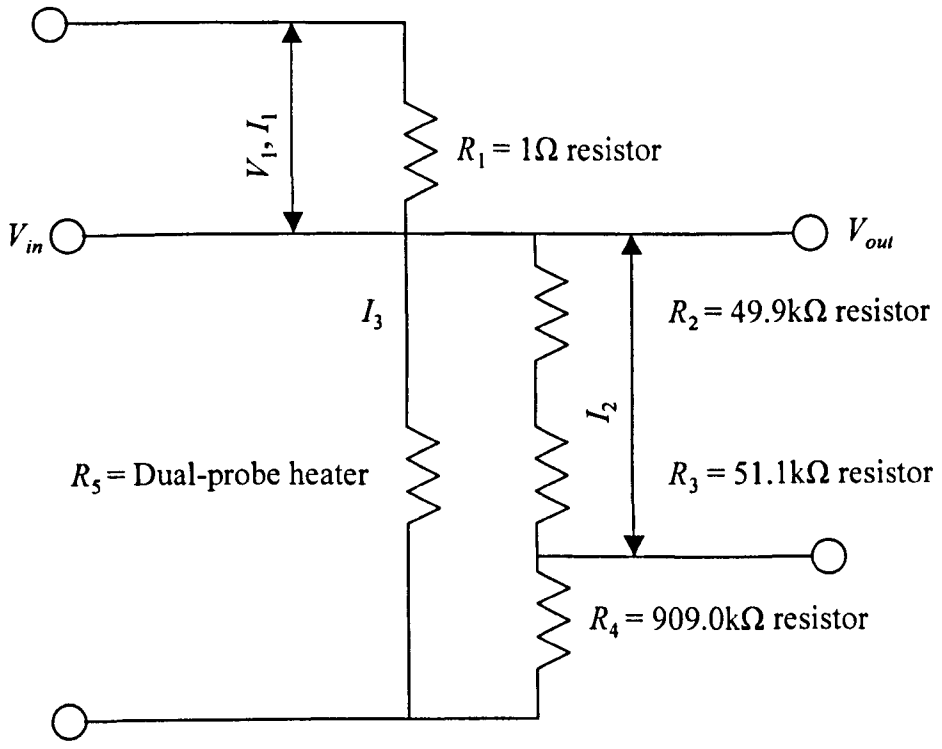

Figure 8.13 Electric circuit and sign used in the error analysis

Step 1 Relative Error of I_1

Current is calculated as $I_1 = V_1/R_1$; the relative error of I_1 could be calculated as:

$$\frac{dI_1}{I_1} = \sqrt{\left(\frac{dV_1}{V_1}\right)^2 + \left(\frac{-dR_1}{R_1}\right)^2} \tag{8.13}$$

$$\frac{dI_1}{I_1} = \sqrt{\left(\frac{2.5\times10^{-3}}{0.465}\right)^2 + \left(\frac{-0.01}{1.00}\right)^2} = 0.011$$

where $dV_1 = 2.5\times10^{-3}$ V, the data logger analogue signal measurement accuracy

$dR_1 = 0.01\Omega$, the accuracy of the 1Ω resistor

V_1 = measured voltage across the 1Ω resistor with the data logger (V)

Step 2 Relative Error of the Voltage Across the Dual-probe 'Effective' Heater

As R_2 and R_3 were in series in the voltage divider and used as one resistor, the total error of them was:

$$d(R_2 + R_3) = \sqrt{dR_2{}^2 + dR_3{}^2} \tag{8.14}$$

$$d(R_2 + R_3) = \sqrt{(0.0499\times10^3)^2 + (0.0511\times10^3)^2} = 0.0714\times10^3\Omega$$

The data logger measured voltage was the voltage across the voltage divider V_{out}. The relationship between the voltage across the dual-probe heater V_{in} and V_{out} was:

$$V_{in} = V_{out} \times \left(\frac{R_4}{R_2 + R_3} + 1\right) \tag{8.15}$$

The relative error of V_{in} was:

$$\frac{dV_{in}}{V_{in}} = \sqrt{\left(\frac{dR_4}{R_2+R_3+R_4}\right)^2 + \left(\frac{R_4 \times d(R_2+R_3)}{(R_2+R_3)\times(R_2+R_3+R_4)}\right)^2 + \left(\frac{dV_{out}}{V_{out}}\right)^2} \tag{8.16}$$

$$\frac{dV_{in}}{V_{in}} = \sqrt{\left(\frac{0.909\times10^3}{101\times10^4}\right)^2 + \left(\frac{909\times10^3\times0.071\times10^3}{101\times10^3\times101\times10^4}\right)^2 + \left(\frac{2.5\times10^{-3}}{1.299}\right)^2} = 0.00222$$

where $dR_4 = 0.909\times10^3\Omega$, the accuracy of the 909.0kΩ resistor.

Step 3 Examination of whether I_3 Can Be Replaced by I_1

According to the principle of an electric circuit as shown in Figure 8.13, the voltages across the resistors are the same in a parallel circuit, and the total current equals the sum of the current through each resistor in the series circuit.

$$I_3 \times R_5 = (R_2+R_3+R_4)\times I_2 \tag{8.17}$$

$$I_1 = I_2 + I_3 \tag{8.18}$$

where I_2 = current through the voltage divider (A)

I_3 = current through the dual-probe heater (A)

Rearranging Equation (8.17) and substituting into Equation (8.18), the relationship between I_1 and I_3 was:

$$I_3 = \frac{R_2+R_3+R_4}{R_2+R_3+R_4+R_5}\times I_1 \tag{8.19}$$

$$I_3 = \frac{49.9\times10^3+51.1\times10^3+909\times10^3}{49.9\times10^3+51.1\times10^3+909\times10^3+28}\times I_1 = 0.99997I_1$$

The difference between I_3 and I_1 was 0.003%. Therefore, I_3 can be replaced by I_1.

Step 4 Relative Error of Power Input to the Dual-probe 'Effective' Heater

According to the power, current and voltage relationship $P_{eff} = V_{in} \times I_1$, the relative error of the power was:

$$\frac{dP_{eff}}{P_{eff}} = \sqrt{\left(\frac{dV_{in}}{V_{in}}\right)^2 + \left(\frac{dI_1}{I_1}\right)^2} \tag{8.20}$$

$$\frac{dP_{eff}}{P_{eff}} = \sqrt{0.00222^2 + 0.011^2} = 0.0112$$

Step 5 Relative Error of the Power Input to the Dual-probe 'Real' Heater

In order to calculate the error in power input to the dual-probe, the error in measuring the resistance wires must be solved first. There was a 0.2mm measurement error when measuring the resistance wires in construction of the dual-probe heater. This error was examined with an example of No.2's heater. The symbol of resistance wire length used in this calculation is shown in Figure 8.1.

1. The resistance wire length of the 'effective' heater

The total resistance wire length, L_{AF} = 300.5±0.2mm

Wires soldered onto the printed circuit board, $L_{AB} + L_{EF}$ = 20.0±0.3mm

Thus, the resistance wire length of the 'effective' heater, L_{BE} = 280.5±0.4mm

2. The resistance wire length of the 'real' heater

The length of the wire not wound onto the core, $L_{BC} + L_{DE}$ = 43.8±0.3mm

Thus, the resistance wire length of the 'real' heater, L_{CD} = 256.7±0.5mm

According to the relationship between 'real' power input and 'effective' power input:

$$P_{real} = P_{eff} \times \frac{L_{CD}}{L_{BE}}$$

The relative error of 'real' power input was calculated as:

$$\frac{dP_{real}}{P_{real}} = \sqrt{\left(\frac{dL_{BE}}{L_{BE}}\right)^2 + \left(\frac{dL_{CD}}{L_{CD}}\right)^2 + \left(\frac{dP_{eff}}{P_{eff}}\right)^2} \qquad (8.21)$$

$$\frac{dP_{real}}{P_{real}} = \sqrt{\left(\frac{0.4}{280.5}\right)^2 + \left(\frac{0.5}{256.7}\right)^2 + (0.0112)^2} = 0.0115$$

Step 6 Volumetric Heat Capacity Error Caused by Measurement Error of Energy Input (q, J/m) to the Dual-probe 'Real' Heater

As expressed in Equation (8.4), the energy input to the dual-probe 'real' heater was

$$q = \frac{t}{l_h} \times P_{real}$$

The relative error of energy input was calculated as:

$$\frac{dq}{q} = \sqrt{\left(\frac{dt}{t}\right)^2 + \left(\frac{dl_h}{l_h}\right)^2 + \left(\frac{dP_{real}}{P_{real}}\right)^2} \qquad (8.22)$$

$$\frac{dq}{q} = \sqrt{\left(\frac{29.9\times10^{-3}}{10.0}\right)^2 + \left(\frac{0.0002}{0.0500}\right)^2 + 0.0115^2} = 0.0125$$

where $dt = 29.9\times10^{-3}$s, the data logger instruction execution time

$dl_h = 0.2$mm, the measurement error of the heater length

The absolute error of energy input was calculated as:

$$dq = \frac{dq}{q} \times q = 0.0125 \times 1110 = 13.9\,\text{J/m} \tag{8.23}$$

Volumetric heat capacity error caused by measurement error of energy input to the dual-probe 'real' heater was given by:

$$\frac{\partial(\rho c_p)}{\partial q} = \left| \frac{1}{e\pi r^2 \Delta T_m} \right| \tag{8.24}$$

$$\frac{\partial(\rho c_p)}{\partial q} = \left| \frac{1}{2.7183 \times \pi \times 0.01234^2 \times 1.32} \right| = 583\,\text{m}^{-2}\cdot\text{K}^{-1}$$

$$\frac{\partial(\rho c_p)}{\partial q} \times dq = 583 \times 13.9 = 8100\,\text{J/m}^3\text{K}$$

Step 7 Volumetric Heat Capacity Error Caused by the Temperature Measurement Error

The thermocouple calibration error, $d(\Delta T_m)$ was 0.04°C, which caused the moisture error:

$$\frac{\partial(\rho c_p)}{\partial(\Delta T_m)} = \left| \frac{-q}{e\pi r^2 \Delta T_m^{\,2}} \right| \tag{8.25}$$

$$\frac{\partial(\rho c_p)}{\partial(\Delta T_m)} = \left| \frac{-1110}{2.7183 \times \pi \times 0.01234^2 \times 1.32^2} \right| = 490000\,\text{J/m}^3\text{K}^2$$

$$\frac{\partial(\rho c_p)}{\partial(\Delta T_m)} \times d(\Delta T_m) = 490000 \times 0.04 = 20000\ \mathrm{J/m^3K}$$

Step 8 Volumetric Heat Capacity Error Caused by Probe Spacing Measurement Error

The measurement error of probe spacing, *dr* was 0.1mm. The volumetric heat capacity error caused by the probe spacing measurement error was:

$$\frac{\partial(\rho c_p)}{\partial r} = \left| \frac{-2q}{e\pi r^3 \Delta T_m} \right| \tag{8.26}$$

$$\frac{\partial(\rho c_p)}{\partial r} = \left| \frac{-2 \times 1110}{2.7183 \times \pi \times 0.01234^3 \times 1.32} \right| = 104900000\ \mathrm{J/m^4K}$$

$$\frac{\partial(\rho c_p)}{\partial r} \times dr = 104900000 \times 0.0001 = 10490\ \mathrm{J/m^3K}$$

Step 9 Combination of Errors

The total error of volumetric heat capacity was a geometrical addition of error caused by all factors:

$$d(\rho c_p) = \sqrt{\left(\frac{\partial(\rho c_p)}{\partial q} dq\right)^2 + \left(\frac{\partial(\rho c_p)}{\partial(\Delta T_m)} d(\Delta T_m)\right)^2 + \left(\frac{\partial(\rho c_p)}{\partial r} dr\right)^2} \tag{8.27}$$

$$\begin{aligned} d(\rho c_p) &= \sqrt{8100^2 + 20000^2 + 10490^2} \\ &= \sqrt{65610000 + 400000000 + 110040100} \\ &= 24000\mathrm{J/m^3K} \end{aligned}$$

The dual-probe measured volumetric heat capacity of sample No.2 was 647000±24000J/m^{3}K. A MATLAB program was used to calculate of the error analysis in ρc_p for nine samples. The program instructions were as follows:

%Error analysis for ρc_p

```
%calculate the relative error for I1
V1=0.465; dV1=2.5e-3; %unit is voltage
R1=1; dR1=0.01; %unit is ohm
dI1l=sqrt(dV1^2/V1^2+dR1^2/R1^2); %0.0114

%calculate the relative error for Vin
R2=49.9e3; dR2=49.9; %unit is ohm
R3=51.1e3; dR3=51.1; %unit is ohm
R4=909e3; dR4=909; %unit is ohm
Vout=1.299; dVout=2.5e-3; %unit is voltage
dVinl=sqrt(dR4^2/(R2+R3+R4)^2+dR2^2*R4^2/(R2+R3)^2/(R2+R3+R4)^2+...
   dR3^2*R4^2/(R2+R3)^2/(R2+R3+R4)^2+dVout^2/Vout^2); %0.00111

t=10; dt=29.9e-3; %time, the unit is second
lh=0.05; dlh=0.2e-3; %heater length, the unit is m.
l2=256.7e-3; dl2=0.5e-3; %wire length of real heater, the unit is m.
l1=280.5e-3; dl1=0.4e-3; %effective heater length, the unit is m.
r=0.01234; dr=0.0001; %dual probe space, the unit is m.
Tm=1.32; dTm=0.04; %maximum temperature rise the unit is deg C.

%Calculate the relative error for the effective power
```

```
dpeffl=sqrt(dVinl^2+dI1l^2); %0.0116

%calculate the relative error for the real power
dpreall=sqrt(dpeffl^2+dl1^2/l1^2+dl2^2/l2^2); %0.0118

%calculate the relative error for the heater input error
dql=sqrt(dpreall^2+dt^2/t^2+dlh^2/lh^2); %0.0128

%calculate the error for the rocp
q=t/lh*l2/l1*Vout*(R4/(R2+R3)+1)*V1/R1; %1.1056e+003
rocp=t/lh*l2/l1*Vout*(R4/(R2+R3)+1)*V1/R1/2.71828/pi/r^2/Tm; %6.4408e+005
drocpl=sqrt(dql^2+4*dr^2/r^2+dTm^2/Tm^2); %0.035
drocp=drocpl*rocp %2.2443e+004
```

The results of the nine samples' error analysis in ρc_p are shown in Tables D.2 to D.10. It can be seen that the errors regarding to the nine samples' measurement were in the range of 20000 to 24000J/m^{3}K. The ρc_p of sample No.1 was measured to 651000±25000J/m^{3}K. The ρc_p of sample No.2 was measured to 647000±24000J/m^{3}K. The ρc_p of sample No.3 was measured to 640000±23000J/m^{3}K. The ρc_p of sample No.4 was measured to 621000±22000J/m^{3}K. The ρc_p of sample No.5 was measured to 617000±23000J/m^{3}K. The ρc_p of sample No.6 was measured to 628000±22000J/m^{3}K. The ρc_p of sample No.7 was measured to 638000±24000J/m^{3}K. The ρc_p of sample No.8 was measured to 630000±22000J/m^{3}K. The ρc_p of sample No.9 was measured to 621000±24000J/m^{3}K.

8.10.2 Error Analysis in $\Delta\theta_m$

The aim of the dual-probe test was to test the moisture changes of the sample. In order to investigate the errors associated with the probe measurement of $\Delta\theta_m$, it was necessary to consider the parameters within Equation (3.10).

$$\Delta\theta_m = \frac{1}{e\pi r^2 \rho_0 c_{pw}} \left(\frac{q_0}{\Delta T_{m0}} - \frac{q_i}{\Delta T_{mi}} \right)$$

Six parameters in the equation needed to be considered with regard to whether the error could be attributed to them.

1. $q_0, q_i, \Delta T_{m0}, \Delta T_{mi}, r$: mentioned in the data analysis of ρc_p.
2. ρ_0 : dry sample density tested in the laboratory.

To examine the error in ρ_0, it was necessary to find the error in sample dry mass and volume which were tested in the laboratory. The errors associated with the dry mass and volume could be examined carefully with an example calculation of dry sample No.2 test. To examine the errors in $\Delta\theta_m$, it was necessary to find the errors in $q_0, q_i, \Delta T_{m0}, \Delta T_{mi}, r$. q_0 and ΔT_{m0} refer to the dry sample test. q_i and ΔT_{mi} refer to the conditioned sample test. The associated errors related to the $\Delta\theta_m$ test were examined carefully with an example calculation of the dry and conditioned sample No.2 tests.

Step 1 Error of the Sample Volume

The length measurement errors for all sides of the cuboid, dl, dw and dh were 0.1mm. The size of the sample No.2 was 123.8×105.7×100.5mm. The volume of the two holes

drilled in the sample was 71mm^3 i.e., total 0.005% of the sample volume, therefore the effect of volume of the holes could be ignored. The volume of the cuboids can be calculated as $V_0 = l \times w \times h$. The relative error of the volume was:

$$\frac{dV_0}{V_0} = \sqrt{\left(\frac{dl}{l}\right)^2 + \left(\frac{dw}{w}\right)^2 + \left(\frac{dh}{h}\right)^2} \tag{8.28}$$

$$\frac{dV_0}{V_0} = \sqrt{\left(\frac{0.1}{123.8}\right)^2 + \left(\frac{0.1}{105.7}\right)^2 + \left(\frac{0.1}{100.5}\right)^2} = 0.00159$$

Step 2 Absolute Error $d\rho_0$ of Density ρ_0

The sample mass measurement error dm_0 was 0.01g. The sample dry mass m_0 was 816.22g. The density could then be calculated as $\rho_0 = \frac{m_0}{V_0}$. Therefore the density error $d\rho_0$ could be deduced as:

$$\frac{d\rho_0}{\rho_0} = \sqrt{\left(\frac{dm_0}{m_0}\right)^2 + \left(-\frac{dV_0}{V_0}\right)^2} \tag{8.29}$$

$$\frac{d\rho_0}{\rho_0} = \sqrt{\left(\frac{0.01}{816.22}\right)^2 + (-0.00159)^2} = 0.00159$$

$$d\rho_0 = \frac{d\rho_0}{\rho_0} \times \rho_0 = 0.00159 \times 621 = 0.987 \text{ kg/m}^3$$

Step 3 Moisture Error Caused by Probe Spacing Measurement Error

The measurement error of probe spacing, *dr* was 0.1mm. The moisture error caused by the probe spacing measurement error was:

$$\frac{\partial(\Delta\theta_m)}{\partial r}=\left|\frac{-2}{e\pi r^3\rho_0 c_{pw}}\left(\frac{q_0}{\Delta T_{m0}}-\frac{q_i}{\Delta T_{mi}}\right)\right| \tag{8.30}$$

$$\frac{\partial(\Delta\theta_m)}{\partial r}=\left|\frac{-2}{2.7183\times\pi\times0.01234^3\times621\times4180}\left(\frac{1110}{1.32}-\frac{1110}{0.71}\right)\right|$$
$$=35\ \text{kg/kgm}$$

$$\frac{\partial(\Delta\theta_m)}{\partial r}\times dr=35\times0.0001=3.5\times10^{-3}\ \text{kg/kg}$$

Step 4 Moisture Error Caused by Measurement Error of Density ρ_0

Moisture error caused by the density measurement error was given by:

$$\frac{\partial(\Delta\theta_m)}{\partial\rho_0}=\left|\frac{-1}{e\pi r^2{\rho_0}^2 c_{pw}}\left(\frac{q_0}{\Delta T_{m0}}-\frac{q_i}{\Delta T_{mi}}\right)\right| \tag{8.31}$$

$$\frac{\partial(\Delta\theta_m)}{\partial\rho_0}=\left|\frac{-1}{2.7183\times\pi\times0.01234^2\times621^2\times4180}\left(\frac{1110}{1.32}-\frac{1110}{0.71}\right)\right|$$
$$=3.45\times10^{-4}\ \text{kg/kg}\cdot\text{m}^3/\text{kg}$$

$$\frac{\partial(\Delta\theta_m)}{\partial\rho_0}\times d\rho_0=3.45\times10^{-4}\times0.987=3.40\times10^{-3}\ \text{kg/kg}$$

Step 5 Moisture Error Caused by Measurement Error of Energy Input for Dry Sample Test q_0

The energy input error for the dry sample was calculated in Section 8.10.1, which caused the moisture error:

$$\frac{\partial(\Delta\theta_m)}{\partial q_0}=\left|\frac{1}{e\pi r^2\rho_0 c_{pw}\Delta T_{m0}}\right| \tag{8.32}$$

$$\frac{\partial(\Delta\theta_m)}{\partial q_0} = \left| \frac{1}{2.7183 \times \pi \times 0.01234^2 \times 621 \times 4180 \times 1.32} \right|$$

$$= 2.25 \times 10^{-4} \text{ kg/kg} \cdot \text{m/J}$$

$$\frac{\partial(\Delta\theta_m)}{\partial q_0} \times dq_0 = 2.25 \times 10^{-4} \times 0.0125 \times 1110 = 3.12 \times 10^{-3} \text{kg/kg}$$

Step 6 Moisture Error Caused by Temperature Measurement Error for Dry Sample ΔT_{m0}

The thermocouple calibration error was 0.04°C, which caused the moisture error:

$$\frac{\partial(\Delta\theta_m)}{\partial(\Delta T_{m0})} = \left| \frac{-q_0}{e\pi r^2 \rho_0 c_{pw} \Delta T_{m0}^2} \right| \tag{8.33}$$

$$\frac{\partial(\Delta\theta_m)}{\partial(\Delta T_{m0})} = \left| \frac{-1110}{2.7183 \times \pi \times 0.01234^2 \times 621 \times 4180 \times 1.32^2} \right| = 0.189 \text{kg/kgK}$$

$$\frac{\partial(\Delta\theta_m)}{\partial(\Delta T_{m0})} \times d(\Delta T_{m0}) = 0.189 \times 0.04 = 7.56 \times 10^{-3} \text{kg/kg}$$

Step 7 Moisture Error Caused by Measurement Error of Energy Input to the Heater for Conditioned Sample q_i

Energy input error for the conditioned sample was calculated in Section 8.10.1 and caused the moisture error:

$$\frac{\partial(\Delta\theta_m)}{\partial q_i} = \left| \frac{-1}{e\pi r^2 \rho_0 c_{pw} \Delta T_{mi}} \right| \tag{8.34}$$

$$\frac{\partial(\Delta\theta_m)}{\partial q_i} = \left| \frac{-1}{2.7183 \times \pi \times 0.01234^2 \times 621 \times 4180 \times 0.71} \right|$$

$$= 4.17 \times 10^{-4} \text{kg/kg} \cdot \text{m/J}$$

$$\frac{\partial(\Delta\theta_m)}{\partial q_i} \times dq_i = 4.17\times10^{-4} \times 0.0125 \times 1110 = 5.79\times10^{-3}\,\text{kg/kg}$$

Step 8 Moisture Error Caused by Temperature Measurement Error for the Conditioned Sample ΔT_{mi}

The thermocouple calibration error was 0.04°C, which caused the moisture error:

$$\frac{\partial(\Delta\theta_m)}{\partial(\Delta T_{mi})} = \left| \frac{q_i}{e\pi r^2 \rho_0 c_{pw} \Delta T_{mi}^{\ 2}} \right| \tag{8.35}$$

$$\frac{\partial(\Delta\theta_m)}{\partial(\Delta T_{mi})} = \left| \frac{1110}{2.7183\times\pi\times0.01234^2\times621\times4180\times0.71^2} \right| = 0.653\,\text{kg/kgK}$$

$$\frac{\partial(\Delta\theta_m)}{\partial(\Delta T_{mi})} \times d(\Delta T_{mi}) = 0.653\times0.04 = 0.026\,\text{kg/kg}$$

Step 9 Total Moisture Error of $\Delta\theta_m$

The total moisture error was a geometrical addition of error caused by all factors:

$$d(\Delta\theta_m) = \sqrt{\begin{aligned}&\left(\frac{\partial(\Delta\theta_m)}{\partial r}dr\right)^2 + \left(\frac{\partial(\Delta\theta_m)}{\partial \rho_0}d\rho_0\right)^2 + \left(\frac{\partial(\Delta\theta_m)}{\partial q_0}dq_0\right)^2 + \left(\frac{\partial(\Delta\theta_0)}{\partial(\Delta T_{m0})}d(\Delta T_{m0})\right)^2 \\ &+\left(\frac{\partial(\Delta\theta_m)}{\partial q_i}dq_i\right)^2 + \left(\frac{\partial(\Delta\theta_m)}{\partial(\Delta T_{mi})}d(\Delta T_{mi})\right)^2\end{aligned}} \tag{8.36}$$

$$d(\Delta\theta_m) = \sqrt{(3.5\times10^{-3})^2 + (3.40\times10^{-4})^2 + (3.12\times10^{-3})^2 + (7.56\times10^{-3})^2 + (5.79\times10^{-3})^2 + 0.026^2}$$
$$= \sqrt{1.2\times10^{-5} + 1.17\times10^{-7} + 9.73\times10^{-6} + 5.72\times10^{-5} + 3.35\times10^{-5} + 6.7\times10^{-4}}$$
$$= 0.03\text{kg/kg}$$

The dual-probe measured moisture content of conditioned sample No.2 was 0.21±0.03kg/kg. For the nine samples error analysis in $\Delta\theta_m$, MATLAB was used to solve the maths calculation. The program instructions were as follows:

```
% Error analysis for the moisture measurement

a=123.8e-3; da=1e-4; %the unit is m

b=105.7e-3; db=1e-4; %the unit is m

c=100.5e-3; dc=1e-4; %the unit is m

m=816.22e-3; dm=0.01e-3; %the unit is kg

r=0.01234; dr=0.0001; %the unit is m

e=2.71828; %the constant

cc=4180; %it is a constant and the unit is

q0=1110; dq0l=0.0125; %unit is J/m

tm0=1.32; dtm0=0.04; %unit is deg C

qi=1110; dqil=0.0125; %unit is J/m

tmi=0.71; dtmi=0.04; %unit is deg C

ro=m/(a*b*c-71e-9); %620.9907

the=1/pi/r^2/e/ro/cc; %2.9625e-004

theta=the*(q0/tm0-qi/tmi); %0.2153


%Relative error of the sample volume

dvl=sqrt(da^2/a^2+db^2/b^2+dc^2/c^2); %0.00159
```

```
%Error of density
dro=sqrt(dvl^2+dm^2/m^2)*ro; %0.9888

%Moisture error due to the error of spacing
dthetar=2*theta*dr/r; %0.0035

%Moisture error due to the density
dthetaro=theta*dro/ro; %3.41e-04

%Moisture error due to q0.
dthetaq0=the*dq0l*q0/tm0; %0.0031

%Moisture error due to tm0.
dthetatm0=the*q0*dtm0/tm0^2; %0.00756

%Moisture error due to qi.
dthetaqi=the*dqil*qi/tmi; %0.0058

%Moisture error due to tmi.
dthetatmi=the*qi*dtmi/tmi^2; %0.026
%Analysis the total error
derror=sqrt(dthetar^2+dthetaro^2+dthetaq0^2+dthetatm0^2+dthetaqi^2+dthetatmi^2)
%0.0280
```

The results of the nine samples' error analysis in $\Delta\theta_m$ are shown in Tables D.11 to D.19. It can be seen that the errors regarding the nine samples' measurement were in the range of 0.02kg/kg to 0.03kg/kg. The $\Delta\theta_m$ of sample No.1 was measured to 0.17±0.02kg/kg. The

$\Delta\theta_m$ of sample No.2 was measured to 0.21±0.03kg/kg. The $\Delta\theta_m$ of sample No.3 was measured to 0.20±0.02kg/kg. The $\Delta\theta_m$ of sample No.4 was measured to 0.22±0.03kg/kg. The $\Delta\theta_m$ of sample No.5 was measured to 0.07±0.02kg/kg. The $\Delta\theta_m$ of sample No.6 was measured to 0.06±0.01kg/kg. The $\Delta\theta_m$ of sample No.7 was measured to 0.7±0.02kg/kg. The $\Delta\theta_m$ of sample No.8 was measured to 0.07±0.02kg/kg. The $\Delta\theta_m$ of sample No.9 was measured to 0.07±0.02kg/kg.

Chapter 9

Summary and Conclusions

Summary

A series of thermal dual-probe moisture sensors were successfully designed with the use of numerical modelling techniques. Four dual-probes were then constructed for measuring the moisture content of aerated concrete. The moisture content was calculated from the measured values of probe spacing, the heat capacity of water, the maximum temperature rise at the temperature sensor needle and the energy input required to generate the temperature rise. The moisture contents of the aerated concrete samples determined by the dual-probe were then compared with those determined by the gravimetric method. Each of the above steps will now be briefly reviewed.

With regards to the numerical modelling, a series of 2D and 3D Finite Element (FE) models were constructed in order to optimise the design of the dual-probe, i.e. the energy input, pulse time, wall thickness, real wall boundary conditions and probe dimensions. The 2D models were used to determine the preferred probe *spacing*. The 3D models were then used to determine the optimum *lengths* of the heating needle and the temperature sensor needle. In order to ensure that the model was 'robust', 2D and 3D models were tested with the parameters that might affect the accuracy of the model simulations. The time step used in the development work did have an impact on the FE predicted maximum temperature rise. 0.01s was chosen as the time step for the 2D and 3D models because the maximum temperature rise predicted by the 3D model did not change with time steps of 0.01s and 0.0015s. The transient simulation algorithms of backward and the backward-

forward FE calculation methods were suitable for the 2D and 3D models in this study. However, the backward calculation algorithm was applied to all the 2D and 3D models because the backward algorithm was unconditionally stable, computationally reliable and efficient, and more accurate than the backward-forward algorithm under conditions of rapid temperature change. The surface convective heat transfer coefficient did not significantly affect the FE results under typical room conditions.

As the result of the simulation work, a dual-probe design with a probe spacing of 12mm and a heating needle length of 50mm was selected to construct the actual dual-probe. Four 'identical' dual-probes of these dimensions were constructed. The needles of both the heating needle and the temperature sensor needle were made of hypodermic stainless steel tubing. Calibrated type T thermocouples were used to measure the temperature rise at the temperature sensor needle. Copper nickel resistance wire wound onto a core formed the dual-probe heater. The amount of energy input to the dual-probe heater was measured by placing a precision 1Ω resistor in series with the heater and the power supply unit. A CR10X data logger was used in the dual-probe measurements to control a 10s pulse power input to the heater, measure the voltage across the heater, monitor the current through the heater, and record the thermocouple temperature measurement. The data logger measured the voltage across the heater via a voltage divider.

The dual-probe moisture content measurement relies on the accurate measurement of the maximum temperature rise, the energy input and the dual-probe spacing. In this work, the nonlinear model fit method has been developed to analyse the dual-probe measured temperature-time data to obtain the maximum temperature rise and compared to the 'single-point' method. Both methods were suitable for analysing the dual-probe measured temperature-time data. For ease and simplicity, the 'single-point' method was mainly used.

The dual-probe test began with measurement of the volumetric heat capacity of a water-agar medium. The difference between the dual-probe result and the standard value of the water volumetric heat capacity was only 4.8%. The results of the water-agar test thus indicated that the dual-probe was working as expected.

Moving on to the testing of samples of aerated concrete, the samples were cut to a suitable size and holes were drilled for installation of the dual-probe. The samples were tested in both dry and conditioned states. The dry volumetric heat capacity of nine dry samples tested by the dual-probe was then measured to be in the range of 617000±23000 (±3.7%) to 651000±25000 (±3.8%) (J/m^3K). The differences between the dual-probe measured dry volumetric heat capacity and the laboratory measured dry volumetric heat capacity were within the range of 0.2% to 7.9%. The differences between the dual-probe measured dry volumetric heat capacity and the manufacturer's data were within the range of 0.1% to 5.2%.

The moisture contents of nine conditioned samples were then tested by both the dual-probe and the gravimetric method. Initially, four conditioned samples, which were conditioned with an air RH of 96.4%, were tested by the dual-probe. The moisture content was then measured to be in the range of 17%±2% to 22%±3% (kg/kg) of each individual aerated concrete sample's dry mass. Five conditioned samples, which were conditioned with an air RH of 89.0%, were also tested by the dual-probe. The moisture content was then measured to be in the range of 6%±1% to 7%±2% (kg/kg) of each individual aerated concrete sample's dry mass. The differences between the dual-probe measured moisture content and gravimetrically determined moisture content (expressed as a percentage of a sample's dry mass) was 0 to 3% (kg/kg).

The numerical FE modelling work has successfully demonstrated that, depending upon the building fabric material, optimal probe lengths and spacing range from approximately 45-60mm and 12-20mm respectively.

In this work, the nonlinear model fit method has been developed to analyse the dual-probe measured temperature-time data to obtain the maximum temperature rise. The nonlinear model fit method has the advantage of being able to analyse noisy data in a more effective manner.

The work has shown that the temperature sensor needle length can be half that of the heating needle. Thus, the effect of metal tubing on the maximum temperature rise measurement can be reduced compared to previous work (Campbell *et al.*, 1991; Bristow *et al.*, 1993; Tarara and Ham, 1997).

From the results of moisture content measurement and associated error analysis, it was concluded that the accuracy of the prototype dual-probe for moisture content measurements (expressed as a percentage of a sample's dry mass) was ±1% to ±3% (kg/kg). This was felt to be an acceptable degree of accuracy with future development work promising the potential for even better performance.

In conclusion, and most importantly, the thesis clearly indicates that the dual-probe is capable of accurate, *in situ* moisture content measurements in building envelopes. It offers the unique combination of the following attributes. It is:

- capable of producing transient measurements

- potentially capable of producing moisture profiles through the fabric of a building envelope (via the incorporation of additional temperature sensors)
- capable of providing measurements without the need for field calibration
- insensitive to the movement of salts through the building fabrics
- sufficiently accurate
- relatively robust

Future Work

Based on the successes of the work reported in this thesis, EPSRC funding was awarded to further the work. Work will be carried out to improve the performance of the dual-probe moisture sensor. The effect of contact resistance between the surface of the probe and hole can be further investigated via simulations with FE modelling. In order to use the dual-probe to measure the moisture content in different materials, further FE modelling should be undertaken to design the dual-probe to take into account the different material properties.

The size of the aerated concrete samples tested in this work, was determined by the FE modelling. Experimentally, a large sample requires relatively long conditioning time. In order to reduce the time for conditioning samples, smaller samples are thus preferred. Further FE simulation work using models with smaller boundaries can therefore be undertaken to investigate the changes of the maximum temperature rise and the temperature changes at the edge of the boundaries. The model results should provide evidence as to whether the sample size could be further reduced.

The measurement accuracy of maximum temperature rise and energy input is critical for the dual-probe test. To improve the accuracy of temperature measurement, instead of

using a thermocouple, 100 Ohm platinum resistance thermometry (PT100) may be used. Furthermore, there is scope for improving the accuracy of dual-probe heater power measurement.

In principle, the dual-probe is capable of producing moisture profiles through the fabric of a building envelope via the incorporation of additional temperature sensors. This will be tested.

Finally, in this work, the dual-probe was tested in the laboratory, i.e. under the same condition as were simulated with the FE models. In future, the dual-probe will be developed to enable field testing.

References

1. ASTM D71-94, Standard test method for relative density of solid pitch and asphalt. *2000 Annual Book of ASTM Standards*, American Society for Testing and Materials, Philadelphia, 1999.

2. ASTM D4611-86, Standard test method for specific heat of rock and soil. *2000 Annual Book of ASTM Standards*, American Society for Testing and Materials, Philadelphia, 2000.

3. ASTM E104-85, Standard practice for maintaining constant relative humidity by means of aqueous solutions. *1990 Annual Book of ASTM Standards*, American Society for Testing and Materials, Philadelphia, 1990.

4. Batty, W. J., O'Callaghan, P. W., Probert, S. D., Assessment of the thermal probe for rapid, accurate measurements of effective thermal conductivities. *Applied Energy* 1984; 16: 83-113.

5. Beale, J. W., *The development of a probe to determine the moisture content of masonry materials.* Final year report. Brunel University. 1999.

6. Bristow, K. L., Campbell, G. S., Calissendorrf, K., Test of a heat-pulse probe for measuring changes in soil water content. *Soil Science Society American Journal* 1993; 57: 930-934.

7. Bristow, K. L., Kluitenberg, G. J., Horton, R., Measurement of soil thermal properties with a dual-probe heat-pulse technique. *Soil Science Society American Journal* 1994; 58: 1288-1294.

8. Bristow, K. L., Bilskie, J. R., Kluitenberg, G. J., Horton, R., Comparison of techniques for extracting soil thermal properties from dual-probe heat-pulse data. *Soil Science* 1995; 160: 1-7.

9. Bristow, K. L., Measurement of thermal properties and water content of unsaturated sandy soil using dual-probe heat-pulse probes. *Agricultural and Forest Meteorology* 1998; 89: 75-84.

10. BS EN ISO 6946:1997, Building components and building elements - Thermal resistance and thermal transmittance - Calculation method. British Standards, 2003.

11. Campbell, G. S., *Soil physics with BASIC-transport models for soil-plant systems.* Elsevier, New York, 1985.

12. Campbell, G. S., Calissendorff, C., Williams, J. H., Probe for measuring soil specific heat using a heat-pulse method. *Soil Science Society American Journal* 1991; 55: 291-293.

13. Carslaw, H. S., Jaeger, J. C., *Conduction of heat in solids*, 2nd Edn., Clarendon Press, Oxford, 1959.

14. CELCON, The Thin-joint System, A Complete Guide, 2003.

15. CIBSE GUIDE. *Volume A, Design data.* The Chartered Institution of Building Services Engineers, 1986.

16. CR10X Measurement and Control Module Instruction Manual. Campbell Scientific Ltd., 1997.

17. Davies, M., Tirovic, M., Ye, Z., Baker P.H., A low cost, accurate instrument to measure the moisture content of building envelopes *in situ*: a modelling study. *Building Services Engineering Research and Technology* 2004; 25, 2: 175-184.

18. De Vries, D. A., Thermal properties of soils, *In* W. R. Van Wijk (ed.) Physics of Plant Environment. North-Holland Publ. Co., Amsterdam, 1963.

19. Galbraith, G. H., *Heat and moisture transfer within porous building materials.* PhD Thesis. University of Strathclyde, UK. 1992.

20. Galbraith, G. H., Tao, Z. and McLean, R. C., *Building Services Engineering Research & Technology,* 1993; 14(3): 107-113.

21. Galbraith, G. H., McLean, R. C., Guo, J., Moisture permeability data: mathematical presentation. *Building Services Engineering Research & Technology, CIBSE Series A* 1998; 19: 31-36.

22. Galbraith, G. H., Li, J., McLean, R. C., Baker, P. H., The influence of space discretization on the accuracy of numerical simulation of heat and moisture transport in porous building materials. *Journal of Thermal Envelope & Building Science* 2001a; 24: 143-160.

23. Galbraith, G. H., Li, J., Guo, J., Kelly, D., McLean, R. C., Grunewald, J., Evaluation of discretized transport properties for numerical modelling of heat & moisture transfer in building structures. *Journal of Thermal Envelope & Building Science* 2001b; 24: 240-260.

24. Goual, M. S., de Barquin, F., Benmalek, M. L., Bali, A., Quéneudec, M., Estimation of the capillary transport coefficient of clayey aerated concrete using a gravimetric technique. *Cement and Concrete Research* 2000; 30: 1559-1563.

25. Hansen, K. K., *Sorption isotherms: a catalogue and a data base. Water vapour transmission through building materials and systems: mechanisms and measurement.* ASTM STP 1039, American Society for Testing and Materials, Philadelphia, 1989.

26. Haupl, P., Stopp, H., *Measuring method for the in situ measurements of the insulating materials in envelope parts.* IEA Annex 24, 1992.

27. http://www.ugsplm.co.uk

28. http://www.wufi.de

29. Incropera, F. P., DeWitt, D. P., *Introduction to heat transfer.* Chichester UK: John Wiley & Sons, Inc., 1985.

30. Instructions for Protimeter Mini BLD2000, GE Protimeter plc, Meter House, Fieldhouse Lane, Marlow, Bucks, SL7 1LW, UK. 2004.

31. Jowitt, R., Wagstaffe, P. J., *The certification of the water content of microcrystalline cellulose (MCC) at 10 water activities.* CRM 302. BCR information EUR 12429 EN, 1989.

32. Kluitenberg, G. J., Ham, J. M., Bristow, K. L., Error analysis of the heat pulse method for measuring soil volumetric heat capacity. *Soil Science Society American Journal* 1993; 57: 1444-1451.

33. Kluitenberg, G. J., Bristow, K. L., Das, B. S., Error analysis of heat pulse method for measuring soil heat capacity, diffusivity, and conductivity. *Soil Science Society American Journal* 1995; 59: 719-726.

34. Krishnamoorthy, C. S., *Finite element analysis theory and programming, 2nd Edn.,* New Delhi, Tata Mcgraw-Hill Publishing Company Limited. 1996.

35. Kumuran, M. K., *Moisture diffusivity of gypsum board from gamma-ray attenuation measurements.* IEA Annex 24, 1993.

36. Kumaran, M. K., *Material properties.* IEA Annex 24, 1996.

37. Linscott, P., *The further development of a dual-probe to determine the moisture content of masonry materials*. Final year report. Brunel University, UK. 2000.

38. MATLAB, The MathWorks, Inc., Massachusetts, USA.

39. Morris, A. S., *Measurement and calibration requirements for quality assurance to ISO 9000*. John Wiley & Sons, 1994.

40. Nicholas, J. V. and White, D. R., *Traceable temperatures: an introductory guide to temperature measurement and calibration.* Wellington: DSIR Science Information Division, 1982.

41. Noborio, K., McInnes K. J., Heilman, J. L., Measurements of soil water content, heat capacity, and thermal conductivity with a single TDR probe. *Soil Science* 1996; 161: 22-28.

42. Pedersen, C. R., *Combined heat and moisture transfer in building constructions.* PhD Thesis. Technical University of Denmark, Denmark. 1990.

43. Pel, L., Kopinga, K., Otten, H. P., *Moisture measurement with NMR.* IEA Annex 24, 1992.

44. prEN ISO 12570, *Hygrothermal performance of building materials – Determination of moisture by drying at elevated temperature.*

45. prEN ISO 12571, *Hygrothermal performance of building materials - Determination of hygroscopic sorption properties.*

46. Sanders, C., *Environmental conditions.* IEA Annex 24, 1996.

47. Tarara, J. M., Ham, J. M., Measuring soil water content in the laboratory and field with dual-Probe heat-capacity sensors in the laboratory and field. *Agronomy Journal* 1997; 89: 535-542.

48. TC Direct, TC Ltd., PO Box 130, Uxbridge, UB8 2YS, UK. 2003.

49. Ye, Z., Davies, M., Tirovic, M., Baker, P. H., The thermal dual-probe: its application to the in situ measurement of building envelope moisture content. *World Renewable Energy Congress VIII*, Denver, USA, 2004.

Appendix A

The Sensitivity of θ and $\Delta\theta$ to r

A.1 Introduction

Bristow *et al.* (1993) outlined three examples with soil properties to analyse the errors in θ and $\Delta\theta$ that could be expected due to the errors in assumed respective parameters as shown in Equations (3.7) and (3.8). From the calculation results of the examples, the sensitivity of θ and $\Delta\theta$ to r is evident.

To verify the calculation results of three examples outlined by Bristow *et al.* (1993) the examples were also examined by another mathematical calculation method.

A.2 The Sensitivity of θ to r

The sensitivity of θ to r was examined via the calculation results of Example 1.

Example 1

Examine the errors in θ that could be expected due to an error in r.

Letting

$q = 600\text{J/m}$

$r = 0.0060\text{m}$

$\Delta T_m = 0.80°\text{C}$

$\rho_b = 1200\text{kg/m}^3$

$c_{pb} = 875\text{J/kg}^3\text{K}$

$\rho_w c_{pw} = 4.18\text{MJ/m}^3\text{K}$

$$\theta = \frac{\frac{600}{2.7183\times\pi\times0.0060^2\times0.80} - 1200\times875}{4.18\times10^6} = 0.33\text{m}^3/\text{m}^3 \qquad \text{(A.1)}$$

If r changed from 0.0060m to 0.0058m, a relative error of 3.3%, this would lead to θ changing from 0.33 to $0.37\text{m}^3/\text{m}^3$, i.e., a 12% error.

$$r = 0.0060\times(1-0.0333) = 0.0058\text{m} \qquad \text{(A.2)}$$

$$\theta = \frac{\frac{600}{2.7183\times\pi\times0.0058^2\times0.80} - 1200\times875}{4.18\times10^6} = 0.37\text{m}^3/\text{m}^3 \qquad \text{(A.3)}$$

$$\Delta\theta = 0.37 - 0.33 = 0.04\text{m}^3/\text{m}^3 \qquad \text{(A.4)}$$

$$\text{Relative error} = \frac{0.04}{0.33}\times100 \approx 12\% \qquad \text{(A.5)}$$

Verification of Example 1

From a mathematical perspective, Example 1 can also be understood by another approach. The parameter θ varies with the variable r. The changes of θ caused by the changes of r, i.e., the derivative of θ with respect to r can be expressed as:

$$\frac{d\theta}{dr} = -\frac{2q}{e\pi\Delta T_m \rho_w c_{pw} r^3} \qquad \text{(A.6)}$$

Substitute the same parameters as in the Example 1, with r remaining to equal 0.0060m, and the calculation of the derivative of θ with respect to r becomes:

$$\frac{d\theta}{dr} = -\frac{2\times 600}{2.7183\times\pi\times 0.80\times 4.18\times 10^{6}\times 0.0060^{3}} = -195\text{m}^2/\text{m}^3 \qquad \text{(A.7)}$$

It can be seen that a small change of r leads to a large change of θ, because the derivative of θ with respect to r is large. Equation (A.7) verifies Bristow *et al.*'s (1993) conclusion that θ is extremely sensitive to the value of r. This then reaffirms the importance of measuring accuracy.

As with the Example 1, assume r is changed from 0.0060m to 0.0058m. $\Delta\theta$ is calculated as:

$$\Delta\theta = 195\times 0.0002 = 0.039\text{m}^3/\text{m}^3 \qquad \text{(A.8)}$$

which confirms the results of Bristow *et al.* (1993).

A.3 The Sensitivity of θ to r and ΔT_m

The sensitivity of θ to r and ΔT_m was examined via the calculation results of Example 2.

Example 2

In the second example, Bristow *et al.* (1993) analysed the error in θ caused by the changes in the probe spacing r, and the measured maximum temperature rise ΔT_m. It was

determined that if the soil dries out (the maximum temperature rise increases) the water content will be significantly affected, considering the same error in r. This is shown by assuming ΔT_m to be 1.60°C, leading to a 48% error in θ (θ changes from 0.041 to 0.060m^3/m^3).

$$\theta = \frac{\frac{600}{2.7183 \times \pi \times 0.0060^2 \times 1.60} - 1200 \times 875}{4.18 \times 10^6} = 0.041\,\mathrm{m^3/m^3} \qquad \text{(A.9)}$$

$$\theta = \frac{\frac{600}{2.7183 \times \pi \times 0.0058^2 \times 1.60} - 1200 \times 875}{4.18 \times 10^6} = 0.060\,\mathrm{m^3/m^3} \qquad \text{(A.10)}$$

$$\text{Relative error} = \frac{0.060 - 0.041}{0.041} \times 100 = 48\% \qquad \text{(A.11)}$$

Verification of Example 2

The relative error of θ in the above calculation is verified by the following calculation. The relative error $d\theta/\theta$ corresponding to the probe space change dr is a function of the maximum temperature rise ΔT_m.

$$\frac{d\theta}{\theta} = -\frac{2qdr}{r(q - e\pi r^2 \Delta T_m \rho_b c_{pb})} \qquad \text{(A.12)}$$

Substitute the values of the parameter used in the Examples 1 and 2, and ΔT_m equals 0.80°C and 1.60°C respectively, with the relative errors of the two examples being 12% and 48%.

$$\frac{d\theta}{\theta} = -\frac{2\times 600\times(0.0060-0.0058)}{0.0060(600-2.7183\times\pi\times 0.0060^2\times 0.80\times 1200\times 875)} = 12\% \quad \text{(A.13)}$$

$$\frac{d\theta}{\theta} = -\frac{2\times 600\times(0.0060-0.0058)}{0.0060(600-2.7183\times\pi\times 0.0060^2\times 1.60\times 1200\times 875)} = 48\% \quad \text{(A.14)}$$

Which confirms the results of Bristow *et al.* (1993).

A.4 The Sensitivity of $\Delta\theta$ to r and ΔT_m

The sensitivity of $\Delta\theta$ to r and ΔT_m was examined via the calculation results of Example 3.

Example 3

In the third example, Bristow *et al.* (1993) analysed the error in $\Delta\theta$ caused by the changes in the probe spacing r, and the measured maximum temperature rise ΔT_m. Retaining the same parameters in Example 1 for the initial condition, and the parameters in Example 2 as the final condition, if r changed from 0.0060m to 0.0058m, a relative error of 3.3%, this would then lead to $\Delta\theta$ changing from 0.29 to 0.31m^3/m^3, i.e., a 7% error.

$$\Delta\theta = \frac{1}{2.7183\times\pi\times 0.0060^2\times 4.18\times 10^6}\left(\frac{600}{0.80}-\frac{600}{1.60}\right) = 0.29\,m^3/m^3 \quad \text{(A.15)}$$

$$\Delta\theta = \frac{1}{2.7183\times\pi\times 0.0058^2\times 4.18\times 10^6}\left(\frac{600}{0.80}-\frac{600}{1.60}\right) = 0.31\,m^3/m^3 \quad \text{(A.16)}$$

$$\text{Relative error} = \frac{0.31 - 0.29}{0.29} \times 100 = 7\% \tag{A.17}$$

Verification of Example 3

To verify the above calculation, taking the derivative of $\Delta\theta$ (Equation (3.8)) with respect to r, the error in $\Delta\theta$ caused by the changes in the probe spacing r can be obtained.

$$\frac{\partial(\Delta\theta)}{\partial r} = \frac{-2}{e\pi r^3 \rho_w c_{pw}} \left(\frac{q_0}{\Delta T_{m0}} - \frac{q_i}{\Delta T_{mi}} \right) \tag{A.18}$$

Substitute the same parameters as in the Examples 1 and 2, with r remaining equal to 0.0060m, and the calculation of the derivative of $\Delta\theta$ with respect to r is:

$$\frac{\partial(\Delta\theta)}{\partial r} = \frac{-2}{2.7183 \times \pi \times 0.0060^3 \times 4.18 \times 10^6} \left(\frac{600}{0.80} - \frac{600}{1.60} \right) = -97.32\ \text{m}^2/\text{m}^3 \tag{A.19}$$

It can be seen that a small change of r leads to a large change of $\Delta\theta$, because the derivative of $\Delta\theta$ with respect to r is large. In comparison to Equation (A.7), it can be seen that the calculation result of the derivative of $\Delta\theta$ with respect to r is 50% smaller than that of the derivative of θ with respect to r. Therefore, the sensitivity of $\Delta\theta$ to r is reduced.

As with the Example 3, now r is assumed to be changed from 0.0060m to 0.0058m. The changes of $\Delta\theta$ are calculated as:

$$d(\Delta\theta) = 97.32 \times 0.0002 = 0.019\,\text{m}^3/\text{m}^3 \tag{A.20}$$

$$\text{Relative error} = \frac{0.019}{0.29} \times 100 = 7\% \qquad \text{(A.21)}$$

Which confirms the results of Bristow *et al.* (1993).

The calculation results of the three examples are summarized in Table A.1. Further calculation was undertaken to explore the effects of r and ΔT_m to θ. Keeping the same parameters used in the previous three examples, the relative error in θ is listed in Table A.1. Measured ΔT_m increased from 0.50°C to 1.60°C and r changed from 0.0060m to 0.0058m. It is then obvious that with the same errors in r, the relative error in θ will be increased corresponding to the measured ΔT_m increasing as a result of the moisture drying out. Figure A.1 shows that the relative error of the moisture content increases very quickly when the maximum temperature rises up to 1.30°C. The relationship between the maximum temperature rise and the relative error of the moisture content can be expressed as a fourth order polynomial equation.

Table A.1 Summary the calculation results of examples

Example No.	r_0 (m)	r_i (m)	ΔT_m (K)	θ_0 (m^3/m^3)	θ_i (m^3/m^3)	$\Delta\theta$ (m^3/m^3)	Error in θ (%)	Error in $\Delta\theta$ (%)
1	0.0060	0.0058	0.80	0.33	0.37	-	12	-
2	0.0060	0.0058	1.60	0.041	0.060	-	48	-
3(1)	0.0060	-	0.80	-	-	0.29	-	-
3(2)	0.0058	-	1.60	-	-	0.31	-	7

Note:

1. r_0 is the initial probe spacing.
2. r_i is the changed probe spacing.
3. 3(1) and 3(2) are the initial and final conditions of Example 3.

Table A.2 Relative error of moisture content corresponding to the maximum temperature rise

r (mm)	ΔT_m (K)	$d\theta/\theta$ %
5.8	0.5	9.12
5.8	0.6	9.84
5.8	0.7	10.69
5.8	0.8	11.70
5.8	0.9	12.92
5.8	1.0	14.42
5.8	1.1	16.32
5.8	1.2	18.79
5.8	1.3	22.15
5.8	1.4	26.97
5.8	1.5	34.47
5.8	1.6	47.75

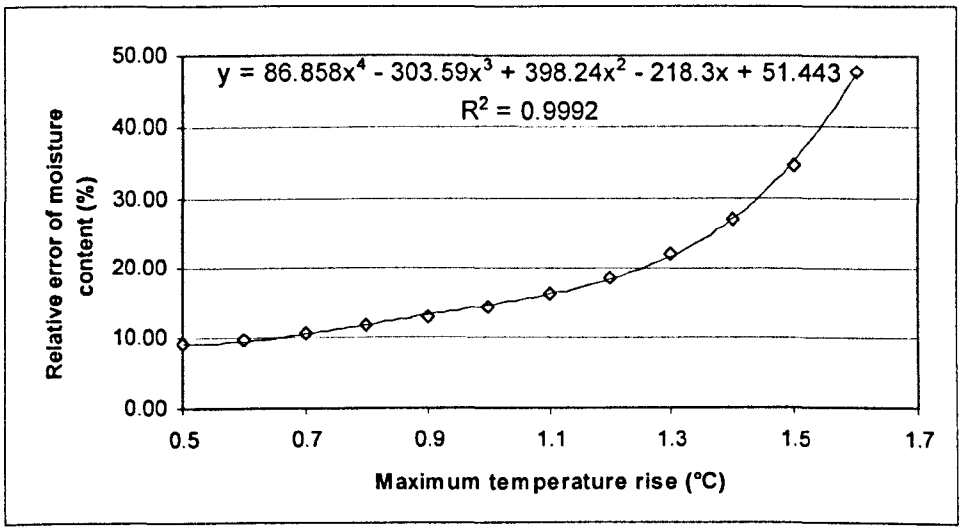

Figure A.1 Effect of probe spacing and maximum temperature rise on the measured moisture content

Appendix B

Equipment Calibration

B.1 Introduction

Before testing the aerated concrete samples, the measuring equipment must be calibrated. Accurate temperature measurement requires the calibration of the thermocouples. The thermocouples were thus calibrated against a reference thermometer.

Two ovens were used for drying and conditioning the samples. A small oven was kept at 40°C for conditioning the aerated concrete samples. A larger oven was kept at 105°C to dry the aerated concrete samples. PID controllers were used to maintain a constant oven temperature with suitable input values of the P, I and D parameters.

B.2 Thermocouple Calibration

A thermocouple consists of two different types of conductors with their ends joined together to form a circuit (Nicholas *et al.*, 1982). A current will occur in the closed circuit when the two junctions of the thermocouple are at different temperatures. Figure B.1 illustrates the current formed in the closed circuit. In principle, the aim of thermocouple calibration was to convert the thermocouple output voltage into a temperature reading. The aim of thermocouple calibration in this project was to correct the thermocouple temperature reading from the data logger.

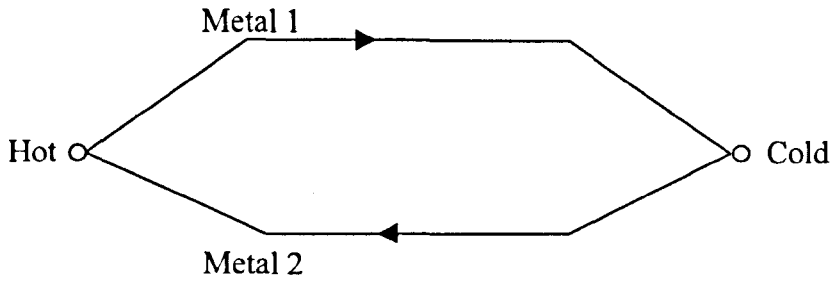

Figure B.1 An emf produces a current in the closed circuit due to the junctions of the thermocouple at different temperatures

Type T thermocouples with sheath diameters of 0.5mm were used for measuring the maximum temperature rise of the sample. The thermocouples were calibrated against a reference thermometer. The apparatus of the thermocouple calibration is shown in Figure B.2, and consisted of a Dewar flask, water, a polystyrene cover, a reference thermometer, a stirrer, a CR10X data logger and computer. The Dewar flask contained water. Two cable ties were used to tie the thermocouple and temperature probe of the reference thermometer together. The measuring thermocouple junction was connected to the data logger differential channel 2. A 10TCRT thermocouple reference temperature device was used to measure the temperature of the reference junction (cold thermocouple junction). The 10TCRT was connected to the data logger single-ended channel 1, switched excitation outputs channel 1 and analogue ground. A polystyrene cover was placed on the open side of the Dewar flask to reduce heat transfer between the water and environment. The thermocouples' warm junction, as well as the temperature probe, were inserted through a hole in the polystyrene cover into the water bath. For the purpose of thermocouple calibration, the warm junction of the thermocouple was immersed 20cm into the Dewar flask containing water. When the water temperature was changed, the water was stirred for at least 5 minutes to achieve a uniform temperature throughout the water inside the flask. The bath was left for 15 minutes before the data was recorded. Unfortunately a small temperature gradient could occur in the water in both axial and radial directions. To

minimise the temperature gradient effect, the thermocouples and the temperature probe of the reference thermometer had to be located in the same temperature layer. Two methods for achieving this are given below:

- The thermocouple and the temperature probe of the reference thermometer were tied in a bundle by wrapping cable ties approximately 4cm from the sensing ends.
- Space was given to the thermocouple end and temperature probe end of the reference thermometer, because if the thermocouple end and temperature probe end of the reference thermometer were tied together, it could affect water circulation and increase the probability of a non-uniform temperature of the water inside the flask.

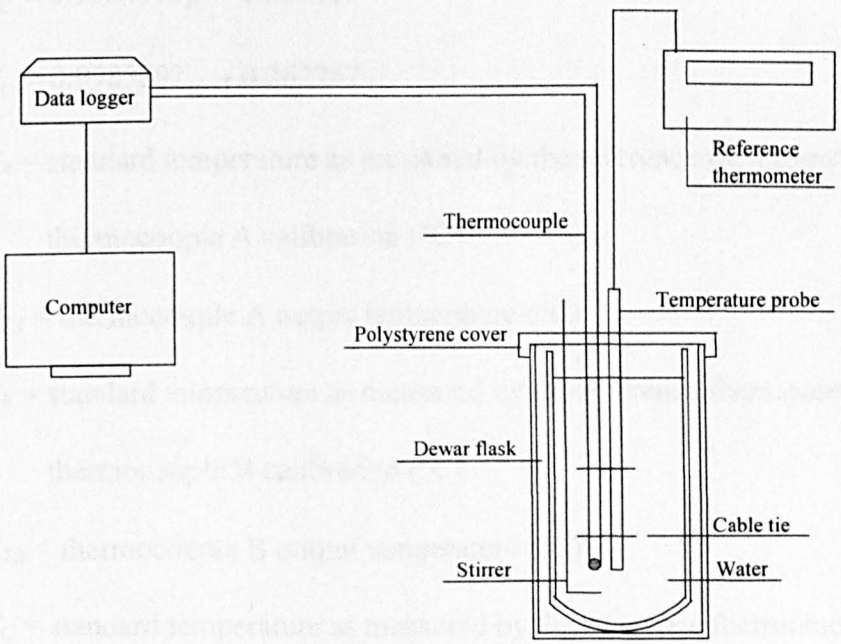

Figure B.2 Apparatus of the thermocouple calibration

A total of four thermocouples were calibrated. The data logger differential channel 2 was used for all temperature measurements' of the dual-probe test and so the four thermocouples were connected to the data logger differential channel 2 individually for calibration. Thirteen different temperature calibration points, from 6 to 50°C, were used. The bath temperature was measured using a reference thermometer (quartz crystal thermometer), Model Quat 100/200, (serial No.0015978, probe serial 08880087, ASAP

Calibration Services Ltd, calibrated January 2004: certificate number No. N1115855T). The uncertainty of the reference thermometer calibration was ±0.02°C.

Microsoft Excel was used to analyse the thermocouple calibration data. The data logger measured thermocouple temperature was related linearly to the reference thermometer measured temperature (Morris, 1994) as follows:

$$T_A = 0.998867T_{TA} + 0.302272 \quad \text{(B.1)}$$

$$T_B = 0.998760T_{TB} + 0.300400 \quad \text{(B.2)}$$

$$T_C = 0.998479T_{TC} + 0.308869 \quad \text{(B.3)}$$

$$T_D = 0.998359T_{TD} + 0.362262 \quad \text{(B.4)}$$

where T_A = standard temperature as measured by the reference thermometer for thermocouple A calibration (°C)

T_{TA} = thermocouple A output temperature (°C)

T_B = standard temperature as measured by the reference thermometer for thermocouple B calibration (°C)

T_{TB} = thermocouple B output temperature (°C)

T_C = standard temperature as measured by the reference thermometer for thermocouple C calibration (°C)

T_{TC} = thermocouple C output temperature (°C)

T_D = standard temperature as measured by the reference thermometer for thermocouple D calibration (°C)

T_{TD}= thermocouple D output temperature (°C)

An example of thermocouple temperature output related to standard temperature is shown in Figure B.3.

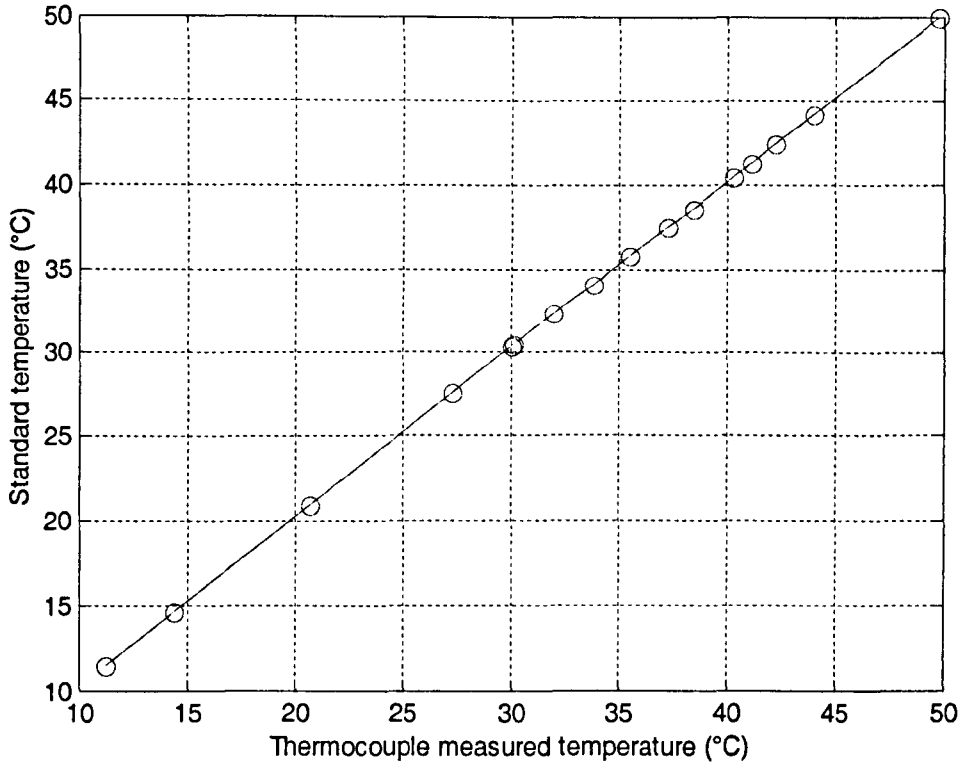

Figure B.3 Thermocouple measured temperature related to standard temperature

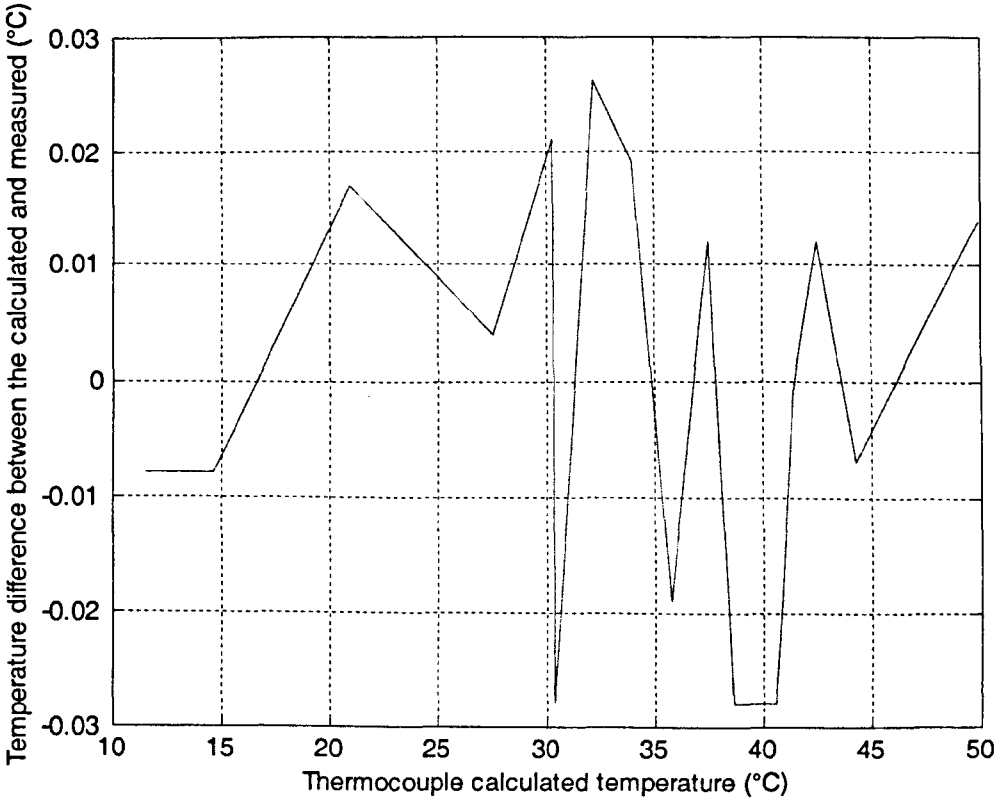

Figure B.4 Temperature errors in the calculated value

Applying the calibration equations (Equations B.1 to B.4) to calculate the 'real' thermocouple measured temperature at the temperature calibration points, for four thermocouples, the temperature difference (error) between the thermocouple calculated temperature and the reference thermometer measured temperature was ±0.03°C and an example is shown in Figure B.4. Thus, the typical error value of four thermocouples calibrated against the reference thermometer was ±0.03°C. Considering the uncertainty of the reference thermometer (±0.02°C), the absolute error of the four thermocouples for temperature (T) measurement was ±0.05°C.

The data logger resolution for thermocouple temperature measurement is another factor that affects the accuracy of thermocouple temperature measurement. Thus, the data logger resolution for thermocouple temperature measurement had to be converted to temperature resolution. The temperature range used for thermocouple calibration was between 6°C and 50°C. The value of thermocouple emf/μV was as follows (TC Direct, 2003):

At 6°C = 234μV

At 50°C = 2036μV

The thermocouple emf output was assumed to be linear at the range of 6°C to 50°C. Therefore, the emf per deg C could be calculated as (2036-234)/(50-6) = 41μV/°C. The data logger resolution for differential thermocouple temperature measurement was ±0.33μV (CR10X Measurement and Control Model Instruction Manual, 1997). The data logger resolution for thermocouple measurement in deg C was calculated as ±(0.33/41)×1=±0.008°C.

Considering the data logger resolution for thermocouple temperature measurement and error associated with the thermocouple calibration obtained via the calibration against the reference thermometer, the final error associated with the thermocouple calibration for temperature (T) measurement was calculated as $\pm\sqrt{0.05^2+0.008^2}=\pm 0.05°C$. It is noted that the data logger resolution for thermocouple measurement in deg C was much smaller than that of the thermocouple calibration error. Thus, the data logger resolution for thermocouple measurement in deg C did not contribute significantly to the total error.

Instrument calibration can, in theory 'eliminate' the systematic error. To minimise random error and obtain the *absolute* value of systematic error, lots of measurements must be taken for one measurement point. However, in practise for thermocouple calibration, only one measurement was taken for each temperature point. Thus, systematic error and random error were still present in the calibrated thermocouple. Applying the thermocouple calibration function (Equations B.1 to B.4) to calculate the temperature changes (ΔT), the systematic error will be reduced for the *relative* measurement of temperature changes. Thus, an estimation of ±0.01°C was made for this reduction. Subtracting ±0.01°C from the typical error of the thermocouple calibration of ±0.03°C, the thermocouple calibration error for the measurement of temperature changes (ΔT) was obtained, i.e., ±0.02°C. Considering the uncertainty of the reference thermometer (±0.02°C), the total error of the four thermocouples for the measurement of temperature changes (ΔT) was ±0.04°C.

Again, considering the effects of the data logger resolution for thermocouple temperature measurement, the final thermocouple calibration error used for the dual-probe test was calculated as $\pm\sqrt{0.04^2+0.008^2}=\pm 0.04°C$.

B.3 Oven Temperature Calibration

A small oven was used to condition the aerated concrete samples. Control of the oven temperature was achieved using a PID feedback control system. The heating element of the oven was composed of a heater and a fan. The oven's temperature fluctuation was ±2.5°C controlled by the original PI temperature controller. To comply with the requirement of prEN ISO 12571: (*'Hygrothermal performance of building materials - Determination of hygroscopic sorption properties'*), the temperature variety should be within ±0.5°C. To achieve this, the oven's original PI temperature controller was replaced by a PID temperature controller (Section 6.4). To get accurate temperature measurements, the oven's original temperature probe was replaced by a PRT100 temperature sensor (Section 6.4). The oven's temperature measured by the PRT100 was used to compare the set point temperature of the controller. If a temperature difference between the PRT100 and the set point of controller occurred, then a solid state relay connected to the controller was used to control the current magnitude of the power supply to the heater of the oven. A schematic diagram in Figure B.5 shows the connection loop of the controller to the oven heater.

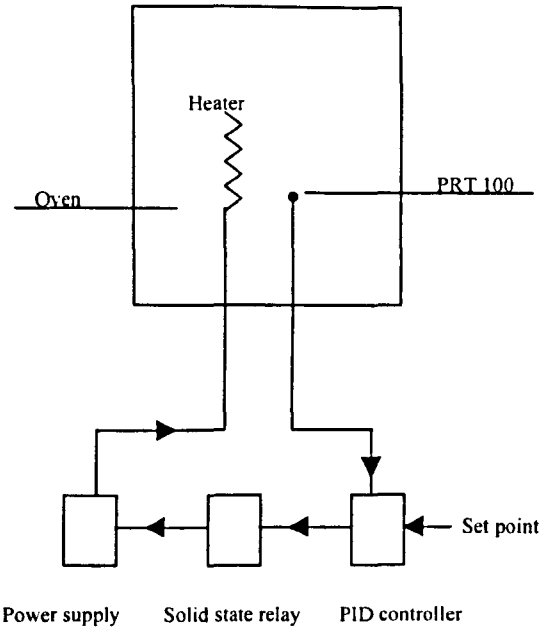

Figure B.5 Schematic diagram of the small oven's temperature control

The aim of the oven controller tuning was to obtain a constant oven temperature. The auto tuning method was used to tune the oven temperature at 40°C. The P, I, D values were 7.93, 932 and 155 respectively. The auto tuning process was completed within 2 hours. To check the stability of the oven's temperature, the oven was left to run for 24 hours. The temperature varied within ±0.10°C. Figure B.6 shows the temperature oscillation of the controller tuning process. To eliminate an offset of the controller effect on the oven's temperature, the temperature of the oven was checked against a PT100 thermometer with an accuracy of ±0.23°C at 40.00°C. The PT100 thermometer's measurement was used to find the actual temperature of the oven. In this case it was 39.18°C. There was, then, a discrepancy between this and the controller's measurement of 40°C. The difference was then added to the controller's temperature; 0.82°C. Thus, the oven's temperature was tuned to 40.00±0.33°C. However, the oven was located in a room without air conditioning, with changes in room temperature affecting the temperature of the oven. It was found that the samples' initial temperature measured from 39.6°C to 40.6°C. The dual-probe measurements results indicated that the initial temperature did not changed

significantly over the 24 hours dry and conditioned samples test period (Sections 8.7and 8.8).

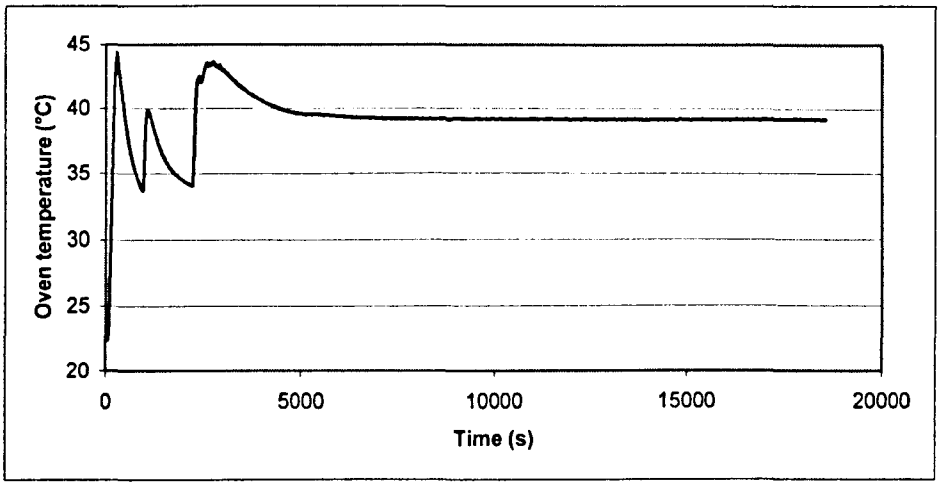

Figure B.6 The temperature oscillation of the controller during tuning process of the small oven

A larger oven was used to dry the aerated concrete samples. A heater and a fan formed the heating element of the oven. To comply with the requirement of prEN ISO 12570: (*'Hygrothermal performance of building materials – Determination of moisture content by drying at elevated temperature'*), the drying temperature should be maintained at 105°C and the temperature variety should be within ±2°C. Applying the auto tuning method, the oven's temperature was set at 105°C. The P, I and D values were 0.2, 2.7 and 27 respectively. The auto tuning process was completed within 1 hour. To check the stability of the oven's temperature, the oven was left to run for 24 hours. The temperature varied within ±1.50°C. Figure B.7 shows the temperature oscillation of the controller tuning process. To obtain an accurate oven temperature, the temperature of the oven was checked against a PT100 thermometer with an accuracy of ±0.36°C at 105.00°C. The PT100 thermometer's measurement was used to find the actual temperature of the oven. In this case it was 101°C. There was, then, a discrepancy between this and the controller's

measurement of 105°C. The difference was then added to the controller's temperature; 4°C. Thus, the oven's temperature was tuned to 105.00±1.86°C.

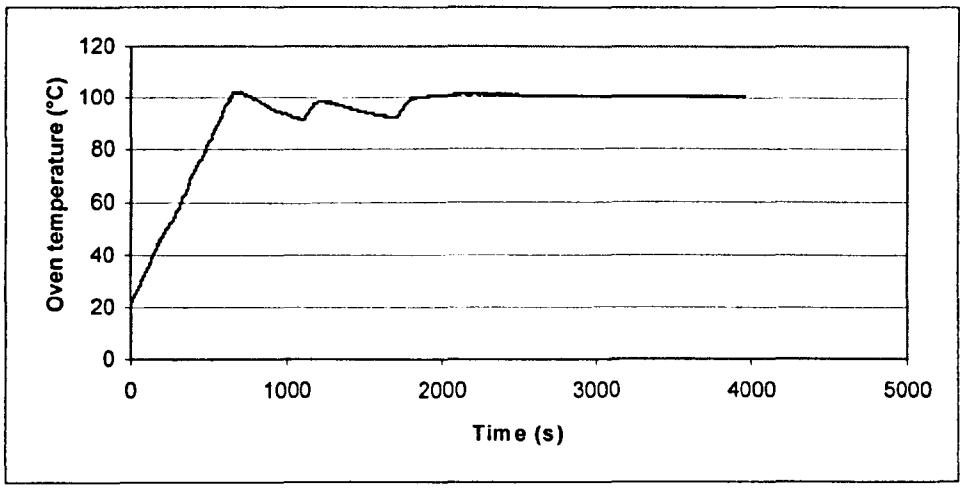

Figure B.7 The temperature oscillation of the controller during tuning process of the large oven

Appendix C

Data Logger Program

The data logger program used for dual-probe was as follows:

```
;
*Table 1 Program
  01: 1          Execution Interval (seconds)
;----------Measure 107-------

1:  Temp (107) (P11)
 1: 1          Reps
 2: 1          SE Channel
 3: 1          Excite all reps w/E1
 4: 1          Loc [ CR10XTemp ]
 5: 1.0        Mult
 6: 0.0        Offset
;--------- Measure Thermocouple----

2:  Thermocouple Temp (DIFF) (P14)
 1: 1          Reps
 2: 1          2.5 mV Slow Range
 3: 2          DIFF Channel
 4: 1          Type T (Copper-Constantan)
 5: 1          Ref Temp (Deg. C) Loc [ CR10XTemp ]
 6: 2          Loc [ TCTemp_1  ]
 7: 1.0        Mult
 8: 0.0        Offset
;--------- Differential Voltage (P2) Measurements----
```

```
3:  Volt (Diff) (P2)
 1: 1         Reps
 2: 35        2500 mV 50 Hz Rejection Range
 3: 4         DIFF Channel
 4: 4         Loc [ voltres    ]
 5: 1.0       Mult
 6: 0.0       Offset
;---------Single ended volts (P1) Measurements-----

4:  Volt (SE) (P1)
 1: 1         Reps
 2: 35        2500 mV 50 Hz Rejection Range
 3: 9         SE Channel
 4: 5         Loc [ voltheate ]
 5: 1.0       Mult
 6: 0.0       Offset
;*****************************************************
;*********** Set a Control Port **********************
;*****************************************************

5:  If time is (P92)
 1: 0         Minutes (Seconds --) into a
 2: 90        Interval (same units as above)
 3: 41        Set Port 1 High

6:  Time (P18)
 1: 0         Seconds into current minute (maximum 60)
 2: 60        Mod/By
 3: 6         Loc [ time       ]

7:  If (X<=>F) (P89)
 1: 6         X Loc [ time       ]
 2: 3         >=
```

```
 3: 10        F
 4: 51        Set Port 1 Low

8:  Do (P86)
 1: 10        Set Output Flag High (Flag 0)

9:  Real Time (P77)
 1: 1111      Year,Day,Hour/Minute,Seconds (midnight = 0000)

10:  Sample (P70)
 1: 1         Reps
 2: 1         Loc [ CR10XTemp ]

11:  Sample (P70)
 1: 1         Reps
 2: 2         Loc [ TCTemp_1  ]

12:  Sample (P70)
 1: 1         Reps
 2: 4         Loc [ voltres   ]

13:  Sample (P70)
 1: 1         Reps
 2: 5         Loc [ voltheate ]

14:  Sample (P70)
 1: 1         Reps
 2: 6         Loc [ time      ]

*Table 2 Program
  02: 0.0000    Execution Interval (seconds)
```

```
*Table 3 Subroutines


End Program
```

Appendix D

Tables of Dual-probe Test Results

Table D.1 Dual-probe measured ρc_p of a water-agar medium

Test No.	I (A)	V (V)	P_{real} (W)	q (J/m)	ΔT_m (K)	Background ΔT_m (K)	Measured ρc_p (MJ/m^3K)	Standard ρc_p (MJ/m^3K)	'Error' (%)
1	0.748	21.53	13.97	2790	0.58	0.00	4.05		3.1%
2	0.748	21.53	13.97	2790	0.59	0.01	3.98		4.8%
3	0.748	21.53	13.97	2790	0.60	0.01	3.91		6.5%
4	0.748	21.53	13.97	2790	0.59	0.01	3.98		4.8%
5	0.748	21.52	13.97	2790	0.59	0.00	3.98		4.8%
6	0.748	21.53	13.97	2790	0.59	0.00	3.98		4.8%
7	0.748	21.53	13.97	2790	0.59	0.00	3.98		4.8%
8	0.748	21.53	13.97	2790	0.59	0.00	3.98	4.18	4.8%
9	0.748	21.53	13.97	2790	0.59	0.00	3.98		4.8%
10	0.748	21.53	13.97	2790	0.59	0.00	3.98		4.8%
11	0.748	21.53	13.97	2790	0.59	0.00	3.98		4.8%
12	0.748	21.53	13.97	2790	0.59	0.00	3.98		4.8%
13	0.748	21.53	13.97	2790	0.60	0.00	3.91		6.5%
14	0.748	21.53	13.97	2790	0.59	0.00	3.98		4.8%
15	0.748	21.53	13.97	2790	0.59	0.00	3.98		4.8%
16	0.748	21.53	13.97	2790	0.59	0.00	3.98		4.8%
Average							3.98		4.8%

Note:

1. 'Error' was the difference between dual-probe measured ρc_p and the standard ρc_p of water.

Table D.2 Dual-probe measured ρc_p of dry sample No.1

Test No.	I (A)	V (V)	P_{real} (W)	q (J/m)	ΔT_m (K)	ρc_p (J/m^{3}K)	$d(\rho c_p)$ (J/m^{3}K)	ρc_p* (J/m^{3}K)	ρc_p** (J/m^{3}K)	'Error^{1}' (%)	'Error^{2}' (%)
1	0.452	13.02	5.12	1020	1.25	651000	25000 (3.8%)			8.0%	0.0%
2	0.452	13.02	5.12	1020	1.25	651000	25000 (3.8%)			8.0%	0.0%
3	0.452	13.02	5.12	1020	1.26	646000	25000 (3.9%)			7.1%	0.8%
4	0.452	13.02	5.12	1020	1.25	651000	25000 (3.8%)			8.0%	0.0%
5	0.452	13.02	5.12	1020	1.25	651000	25000 (3.8%)			8.0%	0.0%
6	0.452	13.02	5.12	1020	1.25	651000	25000 (3.8%)	609000	651000	8.0%	0.0%
7	0.452	13.02	5.12	1020	1.25	651000	25000 (3.8%)			8.0%	0.0%
8	0.452	13.02	5.12	1020	1.25	651000	25000 (3.8%)			8.0%	0.0%
9	0.452	13.02	5.12	1020	1.25	651000	25000 (3.8%)			8.0%	0.0%
10	0.452	13.02	5.12	1020	1.25	651000	25000 (3.8%)			8.0%	0.0%
11	0.452	13.02	5.12	1020	1.25	651000	25000 (3.8%)			8.0%	0.0%
Average				1020	1.25	651000	25000 (3.8%)			7.9%	0.1%

Note:

1. ρc_p as measured by dual-probe.
2. $d(\rho c_p)$ was the measurement error of ρc_p (see Section 8.10.1 for details of error analysis).
3. ρc_p* as measured in the laboratory. Table 6.2 shows the measured ρ. Table E.2 shows the measured c_p.
4. ρc_p** was the manufacturer's data (CELCON, 2003).
5. 'Error^{1}' was the difference between the dual-probe measured and laboratory measued ρc_p.
6. 'Error^{2}' was the difference between the dual-probe measured ρc_p and manufacturer's data.

Table D.3 Dual-probe measured ρc_p of dry sample No.2

Test No.	I (A)	V (V)	P_{real} (W)	q (J/m)	ΔT_m (K)	ρc_p (J/m^{3}K)	$d(\rho c_p)$ (J/m^{3}K)	ρc_p* (J/m^{3}K)	ρc_p** (J/m^{3}K)	'Error^{1}' (%)	'Error^{2}' (%)
1	0.465	12.99	5.53	1110	1.32	647000	24000 (3.7%)			0.2%	0.6%
2	0.465	12.99	5.53	1110	1.32	647000	24000 (3.7%)			0.2%	0.6%
3	0.465	12.99	5.53	1110	1.32	647000	24000 (3.7%)			0.2%	0.6%
4	0.465	12.99	5.53	1110	1.32	647000	24000 (3.7%)			0.2%	0.6%
5	0.465	12.99	5.53	1110	1.33	642000	24000 (3.7%)			0.6%	1.4%
6	0.465	12.99	5.53	1110	1.31	652000	24000 (3.7%)			0.9%	0.2%
7	0.465	12.99	5.53	1110	1.32	647000	24000 (3.7%)			0.2%	0.6%
8	0.465	12.99	5.53	1110	1.31	652000	24000 (3.7%)	652000	651000	0.9%	0.2%
9	0.465	12.99	5.53	1110	1.33	642000	24000 (3.7%)			0.6%	1.4%
10	0.465	12.99	5.53	1110	1.32	647000	24000 (3.7%)			0.2%	0.6%
11	0.465	12.99	5.53	1110	1.32	647000	24000 (3.7%)			0.2%	0.6%
12	0.465	12.99	5.53	1110	1.32	647000	24000 (3.7%)			0.2%	0.6%
13	0.465	12.99	5.53	1110	1.32	647000	24000 (3.7%)			0.2%	0.6%
14	0.465	12.99	5.53	1110	1.32	647000	24000 (3.7%)			0.2%	0.6%
15	0.465	12.99	5.53	1110	1.32	647000	24000 (3.7%)			0.2%	0.6%
16	0.465	12.99	5.53	1110	1.32	647000	24000 (3.7%)			0.2%	0.6%
Average				1110	1.32	647000	24000 (3.7%)			0.2%	0.6%

Note:

1. ρc_p as measured by dual-probe.
2. $d(\rho c_p)$ was the measurement error of ρc_p (see Section 8.10.1 for details of error analysis).
3. ρc_p* as measured in the laboratory. Table 6.2 shows the measured ρ. Table E.2 shows the measured c_p.
4. ρc_p** was the manufacturer's data (CELCON, 2003).
5. 'Error^{1}' was the difference between the dual-probe measured and laboratory measued ρc_p.
6. 'Error^{2}' was the difference between the dual-probe measured ρc_p and manufacturer's data.

Table D.4 Dual-probe measured ρc_p of dry sample No.3

Test No.	I (A)	V (V)	P_{real} (W)	q (J/m)	ΔT_m (K)	ρc_p (J/m^{3}K)	$d(\rho c_p)$ (J/m^{3}K)	ρc_p* (J/m^{3}K)	ρc_p** (J/m^{3}K)	'Error^{1}' (%)	'Error^{2}' (%)
1	0.475	12.99	5.67	1130	1.40	641000	23000 (3.6%)			0.5%	1.5%
2	0.475	12.98	5.67	1130	1.41	636000	22000 (3.5%)			1.2%	2.3%
3	0.475	12.98	5.67	1130	1.40	641000	23000 (3.6%)			0.5%	1.5%
4	0.475	12.98	5.67	1130	1.41	636000	22000 (3.5%)			1.2%	2.3%
5	0.475	12.98	5.67	1130	1.40	641000	23000 (3.6%)			0.5%	1.5%
6	0.475	12.98	5.67	1130	1.40	641000	23000 (3.6%)			0.5%	1.5%
7	0.475	12.98	5.67	1130	1.40	641000	23000 (3.6%)			0.5%	1.5%
8	0.475	12.98	5.67	1130	1.40	641000	23000 (3.6%)	650000	651000	0.5%	1.5%
9	0.475	12.98	5.67	1130	1.40	641000	23000 (3.6%)			0.5%	1.5%
10	0.475	12.98	5.67	1130	1.40	641000	23000 (3.6%)			0.5%	1.5%
11	0.475	12.98	5.67	1130	1.40	641000	23000 (3.6%)			0.5%	1.5%
12	0.475	12.98	5.67	1130	1.40	641000	23000 (3.6%)			0.5%	1.5%
13	0.475	12.98	5.67	1130	1.40	641000	23000 (3.6%)			0.5%	1.5%
14	0.475	12.99	5.67	1130	1.40	641000	23000 (3.6%)			0.5%	1.5%
15	0.475	12.99	5.67	1130	1.40	641000	23000 (3.6%)			0.5%	1.5%
16	0.475	12.99	5.67	1130	1.40	641000	23000 (3.6%)			0.5%	1.5%
17	0.475	12.99	5.67	1130	1.40	641000	23000 (3.6%)			0.5%	1.5%
Average				1130	1.40	640000	23000 (3.6%)			0.6%	1.6%

Note:

1. ρc_p as measured by dual-probe.
2. $d(\rho c_p)$ was the measurement error of ρc_p (see Section 8.10.1 for details of error analysis).
3. ρc_p* as measured in the laboratory. Table 6.2 shows the measured ρ. Table E.2 shows the measured c_p.
4. ρc_p** was the manufacturer's data (CELCON, 2003).
5. 'Error^{1}' was the difference between the dual-probe measured and laboratory measued ρc_p.
6. 'Error^{2}' was the difference between the dual-probe measured ρc_p and manufacturer's data.

Table D.5 Dual-probe measured ρc_p of dry sample No.4

Test No.	I (A)	V (V)	P_{real} (W)	q (J/m)	ΔT_m (K)	ρc_p (J/m^{3}K)	$d(\rho c_p)$ (J/m^{3}K)	$\rho c_p{}^*$ (J/m^{3}K)	$\rho c_p{}^{**}$ (J/m^{3}K)	'Error^1' (%)	'Error^2' (%)
1	0.467	13.00	5.48	1100	1.39	627000	22000 (3.5%)			0.5%	3.7%
2	0.467	12.99	5.47	1090	1.40	617000	22000 (3.6%)			1.1%	5.2%
3	0.467	12.99	5.47	1090	1.40	617000	22000 (3.6%)			1.1%	5.2%
4	0.467	12.99	5.47	1090	1.39	621000	22000 (3.5%)			0.5%	4.6%
5	0.467	12.99	5.47	1090	1.40	617000	22000 (3.6%)			1.1%	5.2%
6	0.467	12.99	5.47	1090	1.40	617000	22000 (3.6%)			1.1%	5.2%
7	0.467	13.00	5.48	1100	1.39	627000	22000 (3.5%)			0.5%	3.7%
8	0.467	13.00	5.48	1100	1.40	623000	22000 (3.5%)	630000	651000	0.2%	4.3%
9	0.467	13.00	5.48	1100	1.39	627000	22000 (3.5%)			0.5%	3.7%
10	0.467	13.00	5.48	1100	1.40	623000	22000 (3.5%)			0.2%	4.3%
11	0.467	13.00	5.48	1100	1.40	623000	22000 (3.5%)			0.2%	4.3%
12	0.467	13.00	5.48	1100	1.40	623000	22000 (3.5%)			0.2%	4.3%
13	0.467	13.00	5.48	1100	1.40	623000	22000 (3.5%)			0.2%	4.3%
14	0.467	12.99	5.47	1090	1.41	613000	22000 (3.6%)			1.8%	5.8%
15	0.467	12.99	5.47	1090	1.40	617000	22000 (3.6%)			1.1%	5.2%
16	0.467	12.99	5.47	1090	1.39	621000	22000 (3.5%)			0.5%	4.6%
Average				1100	1.40	621000	22000 (3.5%)			0.7%	4.6%

Note:

1. ρc_p as measured by dual-probe.
2. $d(\rho c_p)$ was the measurement error of ρc_p (see Section 8.10.1 for details of error analysis).
3. $\rho c_p{}^*$ as measured in the laboratory. Table 6.2 shows the measured ρ. Table E.2 shows the measured c_p.
4. $\rho c_p{}^{**}$ was the manufacturer's data (CELCON, 2003).
5. 'Error^1' was the difference between the dual-probe measured and laboratory measued ρc_p.
6. 'Error^2' was the difference between the dual-probe measured ρc_p and manufacturer's data.

Table D.6 Dual-probe measured ρc_p of dry sample No.5

Test No.	I (A)	V (V)	P_{real} (W)	q (J/m)	ΔT_m (K)	ρc_p (J/m^{3}K)	$d(\rho c_p)$ (J/m^{3}K)	$\rho c_p{}^*$ (J/m^{3}K)	$\rho c_p{}^{**}$ (J/m^{3}K)	'Error^1' (%)	'Error^2' (%)
1	0.456	13.01	5.20	1040	1.34	618000	23000 (3.7%)			1.0%	5.1%
2	0.456	13.01	5.20	1040	1.34	618000	23000 (3.7%)			1.0%	5.1%
3	0.456	13.01	5.20	1040	1.35	613000	22000 (3.6%)			0.2%	5.8%
4	0.456	13.01	5.20	1040	1.34	618000	23000 (3.7%)			1.0%	5.1%
5	0.456	13.01	5.20	1040	1.34	618000	23000 (3.7%)	617000	651000	1.0%	5.1%
6	0.456	13.01	5.20	1040	1.34	618000	23000 (3.7%)			1.0%	5.1%
7	0.456	13.01	5.20	1040	1.34	618000	23000 (3.7%)			1.0%	5.1%
8	0.456	13.01	5.20	1040	1.34	618000	23000 (3.7%)			1.0%	5.1%
9	0.456	13.01	5.20	1040	1.35	613000	22000 (3.6%)			0.2%	5.8%
10	0.456	13.01	5.20	1040	1.34	618000	23000 (3.7%)			1.0%	5.1%
11	0.456	13.02	5.20	1040	1.34	618000	23000 (3.7%)			1.0%	5.1%
Average				1040	1.34	617000	23000 (3.7%)			0.8%	5.2%

Note:

1. ρc_p as measured by dual-probe.
2. $d(\rho c_p)$ was the measurement error of ρc_p (see Section 8.10.1 for details of error analysis).
3. $\rho c_p{}^*$ as measured in the laboratory. Table 6.2 shows the measured ρ. Table E.2 shows the measured c_p.
4. $\rho c_p{}^{**}$ was the manufacturer's data (CELCON, 2003).
5. 'Error^1' was the difference between the dual-probe measured and laboratory measued ρc_p.
6. 'Error^2' was the difference between the dual-probe measured ρc_p and manufacturer's data.

Table D.7 Dual-probe measured ρc_p of dry sample No.6

Test No.	I (A)	V (V)	P_{real} (W)	q (J/m)	ΔT_m (K)	ρc_p (J/m^{3}K)	$d(\rho c_p)$ (J/m^{3}K)	ρc_p* (J/m^{3}K)	ρc_p** (J/m^{3}K)	'Error^{1}' (%)	'Error^{2}' (%)
1	0.474	12.96	5.65	1130	1.41	626000	22000 (3.5%)			0.2%	3.8%
2	0.474	12.96	5.65	1130	1.41	626000	22000 (3.5%)			0.2%	3.8%
3	0.474	12.96	5.65	1130	1.40	630000	22000 (3.5%)			0.8%	3.2%
4	0.474	12.96	5.65	1130	1.41	626000	22000 (3.5%)			0.2%	3.8%
5	0.474	12.96	5.65	1130	1.41	626000	22000 (3.5%)			0.2%	3.8%
6	0.474	12.96	5.65	1130	1.40	630000	22000 (3.5%)			0.8%	3.2%
7	0.475	12.96	5.66	1130	1.40	630000	22000 (3.5%)			0.8%	3.2%
8	0.475	12.96	5.66	1130	1.41	626000	22000 (3.5%)	631000	651000	0.2%	3.8%
9	0.475	12.96	5.66	1130	1.40	630000	22000 (3.5%)			0.8%	3.2%
10	0.475	12.96	5.66	1130	1.41	626000	22000 (3.5%)			0.2%	3.8%
11	0.475	12.96	5.66	1130	1.41	626000	22000 (3.5%)			0.2%	3.8%
12	0.475	12.96	5.66	1130	1.41	626000	22000 (3.5%)			0.2%	3.8%
13	0.475	12.96	5.66	1130	1.40	630000	22000 (3.5%)			0.8%	3.2%
14	0.475	12.96	5.66	1130	1.41	626000	22000 (3.5%)			0.2%	3.8%
15	0.475	12.96	5.66	1130	1.40	630000	22000 (3.5%)			0.8%	3.2%
16	0.475	12.96	5.66	1130	1.41	626000	22000 (3.5%)			0.2%	3.8%
17	0.475	12.96	5.66	1130	1.40	630000	22000 (3.5%)			0.8%	3.2%
Average				1130	1.41	628000	22000 (3.5%)			0.4%	3.6%

Note:

1. ρc_p as measured by dual-probe.
2. $d(\rho c_p)$ was the measurement error of ρc_p (see Section 8.10.1 for details of error analysis).
3. ρc_p* as measured in the laboratory. Table 6.2 shows the measured ρ. Table E.2 shows the measured c_p.
4. ρc_p** was the manufacturer's data (CELCON, 2003).
5. 'Error^{1}' was the difference between the dual-probe measured and laboratory measued ρc_p.
6. 'Error^{2}' was the difference between the dual-probe measured ρc_p and manufacturer's data.

Table D.8 Dual-probe measured ρc_p of dry sample No.7

Test No.	I (A)	V (V)	P_{real} (W)	q (J/m)	ΔT_m (K)	ρc_p (J/m^{3}K)	$d(\rho c_p)$ (J/m^{3}K)	ρc_p* (J/m^{3}K)	ρc_p** (J/m^{3}K)	'Error^{1}' (%)	'Error^{2}' (%)
1	0.456	13.04	5.20	1040	1.27	640000	24000 (3.8%)			2.2%	1.7%
2	0.456	13.04	5.20	1040	1.28	635000	24000 (3.8%)			1.4%	2.5%
3	0.456	13.04	5.20	1040	1.28	635000	24000 (3.8%)			1.4%	2.5%
4	0.456	13.04	5.20	1040	1.28	635000	24000 (3.8%)			1.4%	2.5%
5	0.456	13.04	5.20	1040	1.27	640000	24000 (3.8%)			2.2%	1.7%
6	0.456	13.04	5.20	1040	1.27	640000	24000 (3.8%)	632000	651000	2.2%	1.7%
7	0.456	13.04	5.20	1040	1.28	635000	24000 (3.8%)			1.4%	2.5%
8	0.456	13.04	5.20	1040	1.27	640000	24000 (3.8%)			2.2%	1.7%
9	0.456	13.04	5.20	1040	1.27	640000	24000 (3.8%)			2.2%	1.7%
10	0.456	13.04	5.20	1040	1.28	635000	24000 (3.8%)			1.4%	2.5%
11	0.456	13.04	5.20	1040	1.27	640000	24000 (3.8%)			2.2%	1.7%
Average				1040	1.28	638000	24000 (3.8%)			1.9%	2.0%

Note:

1. ρc_p as measured by dual-probe.
2. $d(\rho c_p)$ was the measurement error of ρc_p (see Section 8.10.1 for details of error analysis).
3. ρc_p* as measured in the laboratory. Table 6.2 shows the measured ρ. Table E.2 shows the measured c_p.
4. ρc_p** was the manufacturer's data (CELCON, 2003).
5. 'Error^{1}' was the difference between the dual-probe measured and laboratory measued ρc_p.
6. 'Error^{2}' was the difference between the dual-probe measured ρc_p and manufacturer's data.

Table D.9 Dual-probe measured ρc_p of dry sample No.8

Test No.	I (A)	V (V)	P_{real} (W)	q (J/m)	ΔT_m (K)	ρc_p (J/m^{3}K)	$d(\rho c_p)$ (J/m^{3}K)	ρc_p* (J/m^{3}K)	ρc_p** (J/m^{3}K)	'Error^{1}' (%)	'Error^{2}' (%)
1	0.475	12.98	5.67	1130	1.40	627000	22000 (3.5%)			0.2%	3.7%
2	0.475	12.98	5.67	1130	1.39	632000	22000 (3.5%)			0.6%	2.9%
3	0.475	12.98	5.67	1130	1.39	632000	22000 (3.5%)			0.6%	2.9%
4	0.475	12.98	5.67	1130	1.40	627000	22000 (3.5%)			0.2%	3.7%
5	0.475	12.98	5.67	1130	1.40	627000	22000 (3.5%)			0.2%	3.7%
6	0.475	12.98	5.67	1130	1.40	627000	22000 (3.5%)	634000	651000	0.2%	3.7%
7	0.475	12.98	5.67	1130	1.39	632000	22000 (3.5%)			0.6%	2.9%
8	0.475	12.98	5.67	1130	1.39	632000	22000 (3.5%)			0.6%	2.9%
9	0.475	12.98	5.67	1130	1.40	627000	22000 (3.5%)			0.2%	3.7%
10	0.476	12.98	5.68	1140	1.39	637000	23000 (3.6%)			1.4%	2.2%
11	0.476	12.98	5.68	1140	1.40	633000	22000 (3.5%)			0.8%	2.8%
Average				1130	1.40	630000	22000 (3.5%)			0.5%	3.2%

Note:

1. ρc_p as measured by dual-probe.
2. $d(\rho c_p)$ was the measurement error of ρc_p (see Section 8.10.1 for details of error analysis).
3. ρc_p* as measured in the laboratory. Table 6.2 shows the measured ρ. Table E.2 shows the measured c_p.
4. ρc_p** was the manufacturer's data (CELCON, 2003).
5. 'Error^{1}' was the difference between the dual-probe measured and laboratory measued ρc_p.
6. 'Error^{2}' was the difference between the dual-probe measured ρc_p and manufacturer's data.

Table D.10 Dual-probe measured ρc_p of dry sample No.9

Test No.	I (A)	V (V)	P_{real} (W)	q (J/m)	ΔT_m (K)	ρc_p (J/m^{3}K)	$d(\rho c_p)$ (J/m^{3}K)	ρc_p* (J/m^{3}K)	ρc_p** (J/m^{3}K)	'Error^{1}' (%)	'Error^{2}' (%)
1	0.467	12.99	5.47	1090	1.27	622000	24000 (3.9%)			3.9%	4.5%
2	0.467	12.99	5.47	1090	1.28	618000	24000 (3.9%)			4.5%	5.1%
3	0.467	12.99	5.47	1090	1.28	618000	24000 (3.9%)			4.5%	5.1%
4	0.467	12.99	5.47	1090	1.28	618000	24000 (3.9%)			4.5%	5.1%
5	0.467	12.99	5.47	1090	1.27	622000	24000 (3.9%)			3.9%	4.5%
6	0.467	12.99	5.47	1090	1.27	622000	24000 (3.9%)			3.9%	4.5%
7	0.467	12.99	5.47	1090	1.28	618000	24000 (3.9%)			4.5%	5.1%
8	0.467	12.99	5.47	1090	1.27	622000	24000 (3.9%)			3.9%	4.5%
9	0.467	12.99	5.47	1090	1.27	622000	24000 (3.9%)	653000	651000	3.9%	4.5%
10	0.467	12.99	5.47	1090	1.28	618000	24000 (3.9%)			4.5%	5.1%
11	0.467	12.99	5.47	1090	1.27	622000	24000 (3.9%)			3.9%	4.5%
12	0.467	12.99	5.47	1090	1.27	622000	24000 (3.9%)			3.9%	4.5%
13	0.467	12.99	5.47	1090	1.27	622000	24000 (3.9%)			3.9%	4.5%
14	0.467	12.99	5.47	1090	1.27	622000	24000 (3.9%)			3.9%	4.5%
15	0.467	12.99	5.47	1090	1.27	622000	24000 (3.9%)			3.9%	4.5%
16	0.467	12.99	5.47	1090	1.27	622000	24000 (3.9%)			3.9%	4.5%
17	0.467	12.99	5.47	1090	1.27	622000	24000 (3.9%)			3.9%	4.5%
Average				1090	1.27	621000	24000 (3.9%)			4.0%	4.7%

Note:

1. ρc_p as measured by dual-probe.
2. $d(\rho c_p)$ was the measurement error of ρc_p (see Section 8.10.1 for details of error analysis).
3. ρc_p* as measured in the laboratory. Table 6.2 shows the measured ρ. Table E.2 shows the measured c_p.
4. ρc_p** was the manufacturer's data (CELCON, 2003).
5. 'Error^{1}' was the difference between the dual-probe measured and laboratory measued ρc_p.
6. 'Error^{2}' was the difference between the dual-probe measured ρc_p and manufacturer's data.

Table D.11 Dual-probe measured moisture content of conditioned sample No.1

Test No.	I (A)	V (V)	P_{real} (W)	q (J/m)	ΔT_m (K)	Corrected ΔT_m* (K)	$\Delta\theta_m$ (kg/kg)	$d(\Delta\theta_m)$ (kg/kg)
1	0.457	13.04	5.22	1040	0.80	0.78	0.17	0.02
2	0.457	13.04	5.22	1040	0.80	0.78	0.17	0.02
3	0.457	13.04	5.22	1040	0.81	0.79	0.17	0.02
4	0.457	13.04	5.22	1040	0.80	0.78	0.17	0.02
5	0.457	13.04	5.22	1040	0.81	0.79	0.17	0.02
6	0.457	13.04	5.22	1040	0.81	0.79	0.17	0.02
7	0.457	13.04	5.22	1040	0.80	0.78	0.17	0.02
8	0.457	13.04	5.22	1040	0.80	0.78	0.17	0.02
9	0.457	13.04	5.22	1040	0.80	0.78	0.17	0.02
10	0.457	13.04	5.22	1040	0.81	0.79	0.17	0.02
11	0.457	13.04	5.22	1040	0.81	0.79	0.17	0.02
12	0.457	13.04	5.22	1040	0.80	0.78	0.17	0.02
Average							0.17	0.02

Note:

1. $d(\Delta\theta_m)$ was the measurement error of $\Delta\theta_m$ (see Section 8.10.2 for details of error analysis).
2. * ΔT_m was corrected because heater No.1 was repaired.

Table D.12 Dual-probe measured moisture content of conditioned sample No.2

Test No.	I (A)	V (V)	P_{real} (W)	q (J/m)	ΔT_m (K)	$\Delta\theta_m$ (kg/kg)	$d(\Delta\theta_m)$ (kg/kg)
1	0.464	12.98	5.51	1100	0.71	0.21	0.03
2	0.464	12.98	5.51	1100	0.71	0.21	0.03
3	0.464	12.99	5.52	1100	0.71	0.21	0.03
4	0.464	12.99	5.52	1100	0.71	0.21	0.03
5	0.464	12.99	5.52	1100	0.71	0.21	0.03
6	0.464	12.99	5.52	1100	0.71	0.21	0.03
7	0.464	12.99	5.52	1100	0.71	0.21	0.03
8	0.464	12.99	5.52	1100	0.71	0.21	0.03
9	0.464	12.99	5.52	1100	0.71	0.21	0.03
10	0.464	12.98	5.51	1100	0.71	0.21	0.03
11	0.464	12.99	5.52	1100	0.70	0.22	0.03
12	0.464	12.99	5.52	1100	0.71	0.21	0.03
13	0.464	12.99	5.52	1100	0.71	0.21	0.03
14	0.464	12.99	5.52	1100	0.71	0.21	0.03
Average						0.21	0.03

Note:

1. $d(\Delta\theta_m)$ was the measurement error of $\Delta\theta_m$ (see Section 8.10.2 for details of error analysis).

Table D.13 Dual-probe measured moisture content of conditioned sample No.3

Test No.	I (A)	V (V)	P_{real} (W)	q (J/m)	ΔT_m (K)	$\Delta\theta_m$ (kg/kg)	$d(\Delta\theta_m)$ (kg/kg)
1	0.476	12.98	5.68	1140	0.78	0.20	0.03
2	0.476	12.98	5.68	1140	0.79	0.20	0.02
3	0.476	12.98	5.68	1140	0.79	0.20	0.02
4	0.476	12.98	5.68	1140	0.79	0.20	0.02
5	0.476	12.99	5.69	1140	0.79	0.20	0.02
6	0.476	12.98	5.68	1140	0.79	0.20	0.02
7	0.475	12.98	5.67	1130	0.79	0.19	0.02
8	0.476	12.99	5.69	1140	0.79	0.20	0.02
9	0.476	12.99	5.69	1140	0.79	0.20	0.02
10	0.476	12.99	5.69	1140	0.80	0.19	0.02
11	0.476	12.99	5.69	1140	0.79	0.20	0.02
12	0.476	12.99	5.69	1140	0.79	0.20	0.02
13	0.476	12.99	5.69	1140	0.79	0.20	0.02
14	0.476	12.98	5.68	1140	0.79	0.20	0.02
15	0.476	12.98	5.68	1140	0.79	0.20	0.02
16	0.476	12.98	5.68	1140	0.80	0.19	0.02
17	0.476	12.98	5.68	1140	0.79	0.20	0.02
Average						0.20	0.02

Note:

1. $d(\Delta\theta_m)$ was the measurement error of $\Delta\theta_m$ (see Section 8.10.2 for details of error analysis).

Table D.14 Dual-probe measured moisture content of conditioned sample No.4

Test No.	I (A)	V (V)	P_{real} (W)	q (J/m)	ΔT_m (K)	$\Delta\theta_m$ (kg/kg)	$d(\Delta\theta_m)$ (kg/kg)
1	0.467	12.99	5.47	1090	0.73	0.22	0.03
2	0.467	12.99	5.47	1090	0.73	0.22	0.03
3	0.467	12.99	5.47	1090	0.74	0.22	0.03
4	0.467	12.99	5.47	1090	0.74	0.22	0.03
5	0.467	12.99	5.47	1090	0.74	0.22	0.03
6	0.467	12.99	5.47	1090	0.73	0.22	0.03
7	0.467	12.99	5.47	1090	0.73	0.22	0.03
8	0.467	12.99	5.47	1090	0.74	0.22	0.03
9	0.467	12.99	5.47	1090	0.74	0.22	0.03
10	0.467	12.99	5.47	1090	0.74	0.22	0.03
11	0.467	12.99	5.47	1090	0.74	0.22	0.03
12	0.467	12.99	5.47	1090	0.74	0.22	0.03
13	0.467	12.99	5.47	1090	0.74	0.22	0.03
14	0.467	12.99	5.47	1090	0.74	0.22	0.03
15	0.467	12.99	5.47	1090	0.74	0.22	0.03
16	0.467	12.99	5.47	1090	0.74	0.22	0.03
17	0.467	12.99	5.47	1090	0.73	0.22	0.03
Average						0.22	0.03

Note:

1. $d(\Delta\theta_m)$ was the measurement error of $\Delta\theta_m$ (see Section 8.10.2 for details of error analysis).

Table D.15 Dual-probe measured moisture content of conditioned sample No.5

Test No.	I (A)	V (V)	P_{real} (W)	q (J/m)	ΔT_m (K)	$\Delta\theta_m$ (kg/kg)	$d(\Delta\theta_m)$ (kg/kg)
1	0.456	13.01	5.20	1040	1.03	0.08	0.02
2	0.456	13.01	5.20	1040	1.04	0.07	0.02
3	0.456	13.01	5.20	1040	1.05	0.07	0.02
4	0.456	13.01	5.20	1040	1.04	0.07	0.02
5	0.456	13.01	5.20	1040	1.04	0.07	0.02
6	0.456	13.00	5.19	1040	1.04	0.07	0.02
7	0.456	13.00	5.19	1040	1.05	0.07	0.02
8	0.456	13.01	5.20	1040	1.04	0.07	0.02
9	0.456	13.01	5.20	1040	1.05	0.07	0.02
10	0.456	13.01	5.20	1040	1.05	0.07	0.02
11	0.456	13.01	5.20	1040	1.05	0.07	0.02
12	0.456	13.01	5.20	1040	1.05	0.07	0.02
13	0.456	13.01	5.20	1040	1.04	0.07	0.02
14	0.456	13.01	5.20	1040	1.04	0.07	0.02
15	0.456	13.01	5.20	1040	1.05	0.07	0.02
16	0.456	13.01	5.20	1040	1.04	0.07	0.02
Average						0.07	0.02

Note:

1. $d(\Delta\theta_m)$ was the measurement error of $\Delta\theta_m$ (see Section 8.10.2 for details of error analysis).

Table D.16 Dual-probe measured moisture content of conditioned sample No.6

Test No.	I (A)	V (V)	P_{real} (W)	q (J/m)	ΔT_m (K)	$\Delta\theta_m$ (kg/kg)	$d(\Delta\theta_m)$ (kg/kg)
1	0.474	12.96	5.65	1130	1.12	0.06	0.01
2	0.474	12.95	5.64	1130	1.12	0.06	0.01
3	0.474	12.95	5.64	1130	1.12	0.06	0.01
4	0.474	12.95	5.64	1130	1.13	0.06	0.01
5	0.474	12.95	5.64	1130	1.13	0.06	0.01
6	0.474	12.96	5.65	1130	1.13	0.06	0.01
7	0.474	12.95	5.64	1130	1.12	0.06	0.01
8	0.474	12.96	5.65	1130	1.12	0.06	0.01
9	0.474	12.96	5.65	1130	1.13	0.06	0.01
10	0.474	12.96	5.65	1130	1.13	0.06	0.01
11	0.474	12.96	5.65	1130	1.13	0.06	0.01
12	0.474	12.96	5.65	1130	1.13	0.06	0.01
13	0.474	12.96	5.65	1130	1.13	0.06	0.01
14	0.474	12.96	5.65	1130	1.12	0.06	0.01
15	0.474	12.96	5.65	1130	1.13	0.06	0.01
16	0.474	12.95	5.64	1130	1.13	0.06	0.01
Average						0.06	0.01

Note:

1. $d(\Delta\theta_m)$ was the measurement error of $\Delta\theta_m$ (see Section 8.10.2 for details of error analysis).

Table D.17 Dual-probe measured moisture content of conditioned sample No.7

Test No.	I (A)	V (V)	P_{real} (W)	q (J/m)	ΔT_m (K)	$\Delta\theta_m$ (kg/kg)	$d(\Delta\theta_m)$ (kg/kg)
1	0.457	13.06	5.22	1040	0.99	0.07	0.02
2	0.457	13.06	5.22	1040	0.99	0.07	0.02
3	0.457	13.05	5.21	1040	0.99	0.07	0.02
4	0.457	13.05	5.21	1040	0.99	0.07	0.02
5	0.457	13.05	5.21	1040	0.99	0.07	0.02
6	0.457	13.05	5.21	1040	0.99	0.07	0.02
7	0.457	13.05	5.21	1040	0.99	0.07	0.02
8	0.457	13.06	5.22	1040	0.99	0.07	0.02
9	0.457	13.05	5.21	1040	0.99	0.07	0.02
10	0.457	13.06	5.22	1040	1.00	0.07	0.02
11	0.457	13.06	5.22	1040	0.99	0.07	0.02
Average						0.07	0.02

Note:

1. $d(\Delta\theta_m)$ was the measurement error of $\Delta\theta_m$ (see Section 8.10.2 for details of error analysis).

Table D.18 Dual-probe measured moisture content of conditioned sample No.8

Test No.	I (A)	V (V)	P_{real} (W)	q (J/m)	ΔT_m (K)	$\Delta\theta_m$ (kg/kg)	$d(\Delta\theta_m)$ (kg/kg)
1	0.476	13.00	5.69	1140	1.09	0.07	0.02
2	0.476	13.00	5.69	1140	1.09	0.07	0.02
3	0.476	13.00	5.69	1140	1.09	0.07	0.02
4	0.476	13.00	5.69	1140	1.09	0.07	0.02
5	0.476	13.00	5.69	1140	1.09	0.07	0.02
6	0.476	13.00	5.69	1140	1.09	0.07	0.02
7	0.476	13.00	5.69	1140	1.09	0.07	0.02
8	0.476	13.00	5.69	1140	1.09	0.07	0.02
9	0.476	13.00	5.69	1140	1.09	0.07	0.02
10	0.476	13.00	5.69	1140	1.09	0.07	0.02
Average						0.07	0.02

Note:

1. $d(\Delta\theta_m)$ was the measurement error of $\Delta\theta_m$ (see Section 8.10.2 for details of error analysis).

Table D.19 Dual-probe measaured moisture content of conditioned sample No.9

Test No.	I (A)	V (V)	P_{real} (W)	q (J/m)	ΔT_m (K)	$\Delta\theta_m$ (kg/kg)	$d(\Delta\theta_m)$ (kg/kg)
1	0.468	13.01	5.49	1100	1.00	0.07	0.02
2	0.467	13.01	5.48	1100	0.99	0.07	0.02
3	0.467	13.01	5.48	1100	0.98	0.07	0.02
4	0.467	13.01	5.48	1100	0.98	0.07	0.02
5	0.467	13.01	5.48	1100	0.99	0.07	0.02
6	0.467	13.01	5.48	1100	0.99	0.07	0.02
7	0.468	13.01	5.49	1100	0.99	0.07	0.02
8	0.468	13.01	5.49	1100	0.98	0.07	0.02
9	0.467	13.01	5.48	1100	0.99	0.07	0.02
10	0.468	13.01	5.49	1100	0.99	0.07	0.02
11	0.467	13.01	5.48	1100	0.99	0.07	0.02
12	0.467	13.01	5.48	1100	0.98	0.07	0.02
13	0.467	13.00	5.48	1100	0.98	0.07	0.02
14	0.468	13.01	5.49	1100	0.98	0.07	0.02
15	0.467	13.01	5.48	1100	0.99	0.07	0.02
16	0.467	13.00	5.48	1100	0.98	0.07	0.02
17	0.467	13.00	5.48	1100	0.98	0.07	0.02
18	0.467	13.00	5.48	1100	0.98	0.07	0.02
Average						0.07	0.02

Note:

1. $d(\Delta\theta_m)$ was the measurement error of $\Delta\theta_m$ (see Section 8.10.2 for details of error analysis).

Table D.20 Comparison of dual-probes test results by both 'single-point' method and nonlinear fit method

Test No.	Dry sample ΔT_m (K)		Conditioned sample ΔT_m (K)		$\Delta\theta_m$ (kg/kg)	
	SPM	NMF	SPM	NMF	SPM	NMF
1	1.34	1.35	1.03	1.05	0.08	
2	1.34	1.35	1.04	1.05	0.07	
3	1.35	1.36	1.05	1.06	0.07	
4	1.34	1.35	1.04	1.05	0.07	
5	1.34	1.35	1.04	1.05	0.07	
6	1.34	1.35	1.04	1.06	0.07	
7	1.34	1.35	1.05	1.06	0.07	
8	1.34	1.35	1.04	1.05	0.07	0.07
9	1.35	1.36	1.05	1.06	0.07	
10	1.34	1.35	1.05	1.06	0.07	
11	1.34	1.35	1.05	1.06	0.07	
12	-	-	1.05	1.06	0.07	
13	-	-	1.04	1.06	0.07	
14	-	-	1.04	1.05	0.07	
15	-	-	1.05	1.06	0.07	
16	-	-	1.04	1.06	0.07	
Average	1.34	1.35	1.04	1.06	0.07	

Note:

1. SPM = 'single-point' method.
2. NMF = nonlinear model fit method.
3. Eleven measurements were taken for dry sample test. Sixteen measurements were taken for conditioned sample test.

Table D.21 A comparsion of moisture content as tested by dual-probe and gravimetric methods

Method	Sample moisture content (kg/kg)								
	No.1	No.2	No.3	No.4	No.5	No.6	No.7	No.8	No.9
Dual-probe	0.17	0.21	0.20	0.22	0.07	0.06	0.07	0.07	0.07
Gravimetric	0.20	0.22	0.20	0.22	0.06	0.06	0.07	0.06	0.06

Table D.22 Moisture content inside the aerated concrete samples

Sample	Moisture content (kg/kg)																	
No.	H_1	H_2	H_3	H_4	H_5	H_6	H_7	H_8	H_9	T_1	T_2	T_3	T_4	T_5	T_6	T_7	T_8	T_9
1	0.15	0.16	0.20	0.22	0.23	0.21	0.20	0.16	0.14	0.15	0.17	0.20	0.21	0.22	0.21	0.20	0.16	0.14
2	0.18	0.21	0.23	0.24	0.24	0.21	0.21	0.18	0.15	0.18	0.20	0.22	0.22	0.23	0.22	0.20	0.19	0.16
3	0.15	0.17	0.20	0.20	0.22	0.22	0.20	0.18	0.15	0.16	0.19	0.21	0.22	0.23	0.22	0.21	0.18	0.16
4	0.18	0.21	0.23	0.23	0.22	0.21	0.19	0.18	0.14	0.19	0.22	0.23	0.24	0.23	0.22	0.20	0.18	0.15
5	0.05	0.05	0.06	-	-	-	-	-	-	0.05	0.06	0.05	-	-	-	-	-	-
6	0.06	0.06	0.06	0.07	0.06	0.06	0.06	0.06	0.06	0.06	0.05	0.06	0.06	0.06	0.06	0.06	0.07	0.07

Note:

1. H_1 indicates that the sample was cut from heating needle side, and from samples' surface to 11mm deep.
2. H_9 indicates that the sample was cut from heating needle side, and 88mm from the surface to the start of the sample.
3. T_1 indicates that the sample was cut from temperature sensor needle side, and from samples' surface to 11mm deep.
4. T_9 indicates that the sample was cut from temperature sensor needle side, and 88mm from the surface to the start of the sample.

Appendix E

Laboratory Test of ρc_p for the Aerated Concrete Samples

E.1 Introduction

The ρc_p of the aerated concrete was the most important parameter when considering the maximum temperature rise for the dual-probe test. To verify the manufacturer's data, the ρc_p was tested in the laboratory.

E.2 Laboratory Test of ρ for the Aerated Concrete Samples

As noted in Equation (6.8), the density of the dry sample was defined as the ratio of the sample's dry mass over the sample's volume. To measure the sample density, it was necessary to measure both the mass and volume of the sample.

Considering the certain weight of the dry mass of the sample, as well as the volumes of the Dewar flask and the graduated cylinder used to test the ρc_p of the aerated concrete samples, the sample was cut to 50mm×35mm×100mm approximately. The dry mass of the sample was measured first. After drying in a 105°C oven, the dry mass of the sample was obtained. The details of drying the samples are provided in Section 6.3.

The volume of the sample was measured by a 'water displacement method' (ASTM D71-94 (1999): ('*Standard test method for relative density of solid pitch and asphalt*')). To prevent the aerated concrete sample absorbing water when it was placed into the water, self-adhesive packing tape was wrapped around the surface of the samples. A graduated cylinder and a ruler were used to measure the volume of the water. The volume of the sample was obtained by measuring the water volume before and after the sample was put into the graduated cylinder. The procedures for measuring the sample volume were:

1. A calliper was used to measure the diameter of the graduated cylinder.
2. A ruler was used to measure the height of the water inside the graduated cylinder before and after the sample was added. The volume of the sample and the self-adhesive packing tape, which was wrapped around the surface of the sample, was obtained.
3. The self-adhesive packing tape was removed, and the volume of the self-adhesive packing tape was measured as for step 2.
4. The sample volume was obtained by subtracting the self-adhesive packing tape's volume from the volume of both the sample and self-adhesive packing tape.

Twelve dry samples' densities were measured and are shown in Table E.1. They ranged from 583/m^3 to 626kg/m^3. The average sample dry density was 603kg/m^3. The manufacturer's data was 620kg/m^3. The difference between the measured ρ and the manufacturer's data ranged between 1% and 6%.

Table E.1 The density measurement of dry samples

Sample No.	Dry mass (g)	Volume (cm^3)	Density (kg/m^3)	Error in density (kg/m^3)
1	114.61	183	626	
2	111.40	178	626	
3	100.17	168	596	
4	105.15	178	591	
5	101.96	174	586	
6	101.65	170	598	3
7	99.18	162	612	
8	95.56	154	621	
9	95.90	161	596	
10	107.61	176	611	
11	107.36	184	583	
12	111.03	189	587	
Average			603	

In order to investigate errors in the density measurements, it was necessary to consider the errors associated with the measurements of sample dry mass and volume.

Step 1 Error of the Sample Volume

The volumes of the sample, self-adhesive packing tape and ruler were involved in each measurement of the sample volume. The volume of the sample can then be expressed as:

$$V_a = (h_{aa} - h_{ba} - h_{at} + h_{bt}) \times \left(\left(\frac{d}{2} \right)^2 \pi - l_r \times w_r \right) \qquad \text{(E.1)}$$

Where V_a = volume of the aerated concrete sample (mm^3)

d = diameter of the graduated cylinder (mm)

h_{aa} = the water level of the graduated cylinder after adding the sample wrapped in self-adhesive packing tape (mm)

h_{ba} = the water level of the graduated cylinder before adding the sample wrapped in self-adhesive packing tape (mm)

h_{at} = the water level of the graduated cylinder after adding the self-adhesive packing tape (mm)

h_{bt} = the water level of the graduated cylinder before adding the self-adhesive packing tape (mm)

l_r = the length of the ruler (mm)

w_r = the width of the ruler (mm)

The measurement error for the diameter of the graduated cylinder, dd was 0.1mm. The measurement error of the water level measurement, before and after the sample wrapped in self-adhesive packing tape was added to the graduated cylinder, dh_{ba} and dh_{aa} was 0.1mm. The measurement error of the water level measurement before and after the self-adhesive packing tape was added to the graduated cylinder, dh_{bt} and dh_{at} was 0.1mm. The measurement error of the length and width of the ruler, dl_r and dw_r was 0.1mm. The absolute error in volume can therefore be calculated as:

$$dV_a = \sqrt{\left((dh_{aa})^2 + (dh_{ba})^2 + (dh_{at})^2 + (dh_{bt})^2\right) \times \left(\left(\frac{d}{2}\right)^2 \times \pi - l_r \times w_r\right)^2 + \left(h_{aa} - h_{ba} - h_{at} + h_{bt}\right)^2 \times \left(\left(\frac{d\pi}{2}\right)^2 \times (dd)^2 + l_r^2 \times (dw_r)^2 + w_r^2 \times (dl_r)^2\right)} \quad \text{(E.2)}$$

Step 2 Absolute Error $d\rho$ of Density ρ

The sample mass measurement error dm was 0.01g. The density error $d\rho$ is given in Equation (8.29)

The errors associated with the twelve samples' density measurements were 3kg/m^3 and are shown in Table E.1. The density of the aerated concrete sample was measured to be 603±3kg/m^3 in the laboratory.

E.3 Laboratory Test of c_p for the Aerated Concrete Samples

c_p can be calculated via a technique using the heat transferred by a warm solid to a known quantity of water and measuring the temperature change of either the solid or the water (ASTM D4611-86 (2000): ('*Standard test method for specific heat of rock and soil*')). For this experiment, the heat lost by the solid equals the heat gained by the water.

The aerated concrete sample (50mm×35mm×100mm) was heated in the oven at approximately 100°C until it was dried. Note that if the aerated concrete sample had been heated at a temperature above 100°C, large amounts of steam would have been produced when the aerated concrete sample was put into the water. The mass of the dry aerated concrete (m_a) was then measured. A Dewar flask with a polystyrene cover was used as the calorimeter, i.e., the container was satisfactory insulated. A certain amount of water (m_w) was measured and added to the Dewar flask. The temperatures of the water and the aerated concreted sample were measured by the thermocouple and the CR10X data logger. The thermocouples were not calibrated over 50°C (Section B.2). The accuracy of the class A thermocouple temperature measurement was ±0.5°C (TC Direct, 2003). Therefore, ±0.5°C was used as the temperature measurement accuracy for the heated aerated concrete in the c_p test. The water temperature used in the c_p test was below 50°C, therefore ±0.04°C (see Appendix B) was used as the temperature measurement accuracy for the water. The heated aerated concrete sample temperature ($T_{aerated}$) inside the oven and the temperature of the water ($T_{initial}$) (before the hot sample was inserted) were both measured. The temperature of the water rose after the hot sample was added. The temperature of the water then stabilized and this temperature (T_{final}) was also measured.

Heat was transferred from the aerated concrete sample to the water. The specific heat of the aerated concrete sample can be calculated as:

$$m_a \times c_p \times (T_{aerated} - T_{final}) = m_w \times c_{pw} \times (T_{final} - T_{initial})$$
$$c_p = \frac{m_w \times c_{pw} \times (T_{final} - T_{initial})}{m_a \times (T_{aerated} - T_{final})} \quad \text{(E.3)}$$

A total of four dry samples' specific heat was measured and is shown in Table E.2. It ranged between 1.02kJ/kgK and 1.06kJ/kgK. The average sample dry specific heat was 1.04kJ/kgK. The manufacturer's data was 1.05kJ/kgK. The difference between the measured c_p and the manufacturer's data ranged between 1% and 3%. As described previously, the difference between the measured ρ and the manufacturer's data ranged between 1% and 6% (Section E.2). Thus, the differences between the measured ρc_p and the manufacturer's data ranged between 2% and 9%. The ρc_p test results were consistent with the manufacturer's data.

Table E.2 The specific heat measurement of dry samples

Sample No.	Weight		Temperature			Specific heat	Error in specific heat
	m_w (g)	m_a (g)	$T_{aerated}$ (°C)	$T_{initial}$ (°C)	T_{final} (°C)	c_p kJ/kgK	dc_p kJ/kgK
1	927.15	119.71	99.1	27.35	29.55	1.02	
2	934.41	111.57	99.9	27.55	29.65	1.05	
3	891.93	110.66	99.2	27.00	29.20	1.06	0.03
4	885.32	104.35	99.0	27.88	29.90	1.03	
Average						1.04	

In order to investigate the errors in the specific heat measurement, it was necessary to consider the errors associated with the parameters in Equation (E.3). The measurement error of the dry aerated concrete mass, dm_a was 0.01g. The measurement error of the amount of water, dm_w was 0.01g. The temperature measurement error of the heated aerated concrete sample, $dT_{aerated}$ was 0.5°C. The temperature measurement error of the

water before and after the heated aerated concrete was added into the Dewar flask, $dT_{initial}$ and dT_{final} was 0.04°C.

In terms of a differential equation, the absolute error of specific heat can be written as:

$$dc_p = \sqrt{\left(\frac{dm_w \times c_{pw} \times (T_{final} - T_{initial})}{m_a \times (T_{aerated} - T_{final})}\right)^2 + \left(\frac{m_w \times c_{pw} \times (T_{final} - T_{initial}) \times dm_a}{m_a^2 \times (T_{aerated} - T_{final})}\right)^2 + \left(\frac{m_w \times c_{pw}}{m_a}\right)^2} \times \sqrt{\left[\left(\frac{dT_{initial}}{T_{aerated} - T_{final}}\right)^2 + \left(\frac{(T_{final} - T_{initial}) \times dT_{initial}}{(T_{aerated} - T_{final})^2}\right)^2 + \left(\frac{dT_{final}}{T_{aerated} - T_{final}}\right)^2 + \left(\frac{(T_{final} - T_{initial}) \times dT_{final}}{(T_{aerated} - T_{final})^2}\right)^2\right]} \quad \text{(E.4)}$$

The errors associated with the four samples' specific heat measurements were 0.03kJ/kgK and are shown in Table E.2. The density of the aerated concrete sample was measured to be 1.04±0.03kJ/kgK in the laboratory.

Appendix F

Comparison of Dual-probe, Protimeter and Gravimetrical Method

F.1 Introduction

In a small scale study as an 'add-on' to the main body of work, moisture content of the aerated concrete samples was measured with the dual-probe, then verified by a protimeter and the gravimetrical method. A total of three samples conditioned with a saturated KNO_3 solution at an air RH of 89.0% were used in these tests.

F.2 Moisture Content Tested With the Dual-probe

After completing the dual-probe moisture content measurements for the aerated concrete samples conditioned with an air RH of 89.0% and 96.4% respectively (Sections 8.7 and 8.8), the aerated concrete samples No.7 to No.9 were again conditioned with an air RH of 89.0%. Subsequently, the moisture content of these samples was measured with the dual-probe. For verification, the moisture content of these three aerated concrete samples was also measured by the protimeter and the gravimetrical method. The sample dimensions, the methods of drying and conditioning the sample, the dual-probe test procedures and the data analysis method were the same as for the samples tested before (Chapters 6 and 8).

The protimeter measures the moisture content of wood from 0.12 to 0.26kg/kg, which is equivalent to the moisture content of concrete from 0.04 to 0.07kg/kg (Instructions for Protimeter Mini BLD2000, 2004). Thus, in order to test the moisture content of the samples both by the dual-probe and the protimeter, the samples had to be conditioned to have the moisture content within 0.04 to 0.07kg/kg. Previous dual-probe moisture content measurement results showed that KNO_3 solution could ensure the moisture content was in this range (Section 8.8). The saturated KNO_3 solution was made by mixing 1297.70g KNO_3 and 854.45g of distilled water. The mass, volume and density of the dry samples are given in Table 6.2. The volumetric heat capacity was tested with the dual-probe and the results are given in Tables D.8 to D.10. The moisture content was also measured with the dual-probe and the results are given in Tables D.17 to D.19. The moisture content of the there samples was measured at 0.07±0.02 kg/kg.

F.3 Moisture Content Tested with the Protimeter

A Protimeter Mini BLD2000 sourced by GE Protimeter plc, Bucks, UK, is used to measure the moisture content of wood and the wood moisture equivalent (WME) value of other non-conductive materials. The protimeter measures the moisture content of wood from 0.06 to 0.28kg/kg, the level at which the fibres are saturated. For other non-conductive materials the protimeter measures the WME value up to 0.28kg/kg. However, the protimeter measures the WME value of concrete from 0.04 to 0.07kg/kg. The WME value is the theoretical moisture level that would be attained by wood that is in moisture equilibrium with the material being tested (Instructions for Protimeter Mini BLD2000, 2004).

The changes of moisture content of the three aerated concrete samples were measured with the protimeter after the dual-probe tests. The procedures for using the protimeter are:

1. Open the airtight container which is used to conditioning the samples.
2. Remove the cap of the protimeter to expose the needle electrodes.
3. Switch on the protimeter and push the pins on the surface of the sample and record the reading.
4. Convert the WME value to the moisture content of the aerated concrete using the guidance values table provided by the GE Protimeter plc.

To further verify the dual-probe test results, the moisture content of the conditioned samples was measured by the protimeter and gravimetrical method. The measurement results are shown in Table F.1. It can be seen that:

1. The differences in measured moisture content between the dual-probe and protimeter measurements are 20% to 23%.
2. The differences in measured moisture content between the dual-probe and gravimetric method measurements are in the range of 0% to 14%.

Table F.1 Comparison of samples' moisture content measurement with dual-probe, protimeter and gravimetric methods

Sample No.	Dual-probe (kg/kg)	Protimeter (kg/kg)	Gravimetric (kg/kg)	Difference[1] (%)	Difference[2] (%)
1*	0.07	0.054	0.06	23%	14%
2*	0.07	0.054	0.06	23%	14%
3*	0.07	0.056	0.06	20%	14%
1	0.07	0.056	0.07	20%	0%
2	0.07	0.056	0.06	20%	14%
3	0.07	0.056	0.06	20%	14%

Note:
1. Sample No. with * represents samples that did not reach moisture equilibrium. Sample No. without * represents samples that reached moisture equilibrium.
2. Difference[1] represent the differences in the measured moisture content between the dual-probe and the protimeter measurements.
3. Difference[2] represent the differences in the measured moisture content between the dual-probe and the gravimetric measurements.

Comparison of these three measurement methods shows that the moisture content measured by the dual-probe is between 20% to 23% higher than that measured by the protimeter and between 0 to 14% higher than that measured gravimetrically. If the moisture content measured by the gravimetrical method is a reference value, then the dual-probe provided higher values, whereas the protimeter provided lower values.

Analysing the measurement results of the three test methods, it can be seen that good agreement was achieved. However, the protimeter is limited to measuring the moisture content for concrete in the range of 0.04 to 0.07kg/kg. Manual measurements were also taken by the protimeter method. The dual-probe has the advantage of unlimited range for moisture content measurement. The dual-probe measurement is taken automatically by a computer controlled data logger system. In this way, the test data can be obtained automatically over the whole test period.